

Louisiana State University

LSU Scholarly Repository

LSU Doctoral Dissertations

Graduate School

November 2020

Measurements and Mitigation of Scattered Light Noise in LIGO

Corey Daniel Austin

Louisiana State University and Agricultural and Mechanical College

Follow this and additional works at: https://repository.lsu.edu/gradschool_dissertations



Part of the [Cosmology, Relativity, and Gravity Commons](#), and the [Instrumentation Commons](#)

Recommended Citation

Austin, Corey Daniel, "Measurements and Mitigation of Scattered Light Noise in LIGO" (2020). *LSU Doctoral Dissertations*. 5419.

https://repository.lsu.edu/gradschool_dissertations/5419

This Dissertation is brought to you for free and open access by the Graduate School at LSU Scholarly Repository. It has been accepted for inclusion in LSU Doctoral Dissertations by an authorized graduate school editor of LSU Scholarly Repository. For more information, please contact gradetd@lsu.edu.

MEASUREMENTS AND MITIGATION OF SCATTERED LIGHT NOISE IN LIGO

A Dissertation

Submitted to the Graduate Faculty of the
Louisiana State University and
Agricultural and Mechanical College
in partial fulfillment of the
requirements for the degree of
Doctor of Philosophy

in

The Department of Physics and Astronomy

by
Corey Daniel Austin
B.S., Louisiana State University, 2005
M.S., Louisiana Tech University, 2015
December 2020

I dedicate this work to the memory of Ron Austin.

I miss you and I love you.

ACKNOWLEDGMENTS

Anamaria, for being my mentor and friend. You taught me everything and I wouldn't be here today without all that you've done for me.

Joe G., my advisor, for providing me with the tools and the guidance to get me through this journey.

Gaby, for being a role model who leads by example.

The commissioners who taught me what it means to be a scientist and showed me what can be accomplished when a team of talented people work together: Adam, Marie, Arnaud, Joe B., Stuart, and Matt.

Brian O. and Valera for the lunchtime conversations and for challenging me to be better.

Terra, for being a friend, for helping me to integrate with the team, and for getting me a job at NASA.

Sidd, for being there since my first semester at LSU. You're next and you'll do great things.

Ninja dog, for being my constant companion for the last 13 years. You truly are the best boy!

Mamaw, for loving me unconditionally and for making me believe in myself.

Judy, for being my guardian angel. No matter when I called or what I needed, you were there.

Grandma, for loving me, for believing in me, and for teaching me the value of hard work.

Kelly, for bringing me a happiness that I didn't know was possible. No matter where this world takes us, you'll always have a special place in my heart.

TABLE OF CONTENTS

ACKNOWLEDGMENTS	iii
ABSTRACT	1
CHAPTER 1: INTRODUCTION	2
CHAPTER 2: GRAVITATIONAL WAVES	5
2.1 General Relativity	6
2.2 Sources of Gravitational Waves	9
2.3 Interferometric Gravitational Wave Detection	12
2.4 Laser Interferometer Gravitational Wave Observatory	14
2.5 Observations	22
CHAPTER 3: NOISE FROM SCATTERED LIGHT	27
3.1 Introduction	27
3.2 Effects of Gravitational Waves and Scattered Light on a Complex Electric Field	28
3.3 Amplitude Transfer Coefficient	29
3.4 Transfer Functions	31
3.5 Equivalent Strain Noise	33
3.6 Upconversion from Fringe Wrapping	34
CHAPTER 4: STRAY LIGHT (IMPROVED) CONTROL	37
4.1 SLiC Part A	37
4.2 SLiC Part B	47
CHAPTER 5: SCATTERED LIGHT NOISE FROM INCREASED GROUND MOTION	65
5.1 End Station Layout	65
5.2 Ground Motion	67
5.3 Daytime Noise	68
5.4 Slow Scatter	71
5.5 Fast Scatter	76
CHAPTER 6: BACKSCATTERED LIGHT IN THE LIGO BEAMTUBES	85
6.1 Noise from Backscattered Light	85
6.2 Driven Measurements of Acoustic Coupling	90
6.3 Implications for Future Detectors	94
6.4 Summary	97
CHAPTER 7: CONCLUSION	98
WORKS CITED	102
VITA	107

LIST OF FIGURES

1.1	Cumulative number of detections and public alerts for the LIGO-Virgo network	3
2.1	Schematic layout of a simple Michelson interferometer	13
2.2	Schematic layout of a LIGO interferometer	25
2.3	LIGO Livingston noise budget during the third observing run	26
2.4	A schematic and CAD representation of the LIGO seismic isolation systems	26
3.1	Illustration showing how scattered light originates	28
3.2	Spectrogram showing scattering arches	35
3.3	Spectra of measured and modeled scattering noise	36
4.1	Photo taken in full lock of optics in HAM5	51
4.2	Photograph of newly installed baffles	52
4.3	Low frequency shaker and connecting rod	53
4.4	Shaker line injections made after installing baffles	54
4.5	Coupling functions calculated before and after installing SLiC baffles	54
4.6	PCal periscope before and after baffle installation	55
4.7	Photo showing completed PCal periscope baffle installation	56
4.8	Interferometer response to a 60-75 Hz broadband vibration injection performed at the Y-end of LIGO Livingston. The plot compares identical injections made before and after installing baffles during the October vent.	57
4.9	Photo showing diffuse scatter off of the OFI bench	58
4.10	Photo showing the components on the OFI bench with the HAM5 door removed	59
4.11	Ray tracing of the TFP-AR ghost beam	60
4.12	Photo of TFP-AR ghost beam landing on mirror mount	61
4.13	Photo showing the OFI with the shroud installed	62
4.14	Post-OFI shroud injection comparison	63
4.15	Coupling function and ambient projection after shroud install	64
5.1	CAD drawing of the LIGO end station	66

5.2	Schematic diagram of the sensors and actuators used to control the position of the end test mass	67
5.3	The binary neutron star inspiral range of LIGO Livingston over a 24 hour period	69
5.4	An example of daytime noise at LIGO Livingston	70
5.5	The TMS structure before and after installing the stray light shroud.	71
5.6	Comparison of daytime noise before and after TMS shroud	72
5.7	Spectrogram showing the presence of slow scattering in the gravitational wave channel at LIGO Livingston	73
5.8	Schematic diagram showing the path traversed by the scattered light that caused slow scatter	74
5.9	Comparison of scattering arches in DARM before and after implementing RC tracking	75
5.10	Glitch rates from GravitySpy before and after reaction chain (RC) tracking was implemented at both sites	79
5.11	Spectrogram showing fast scatter as a train passes	80
5.12	Fast scatter comparison of measured vs. modeled	80
5.13	Simple model showing the sum of 0.2 Hz and 4.4 Hz velocities	81
5.14	Spectrograms of the DARM and accelerometer responses to a 3.8 Hz injection .	82
5.15	Spectrograms of the DARM and accelerometer responses to a 3.3-3.9 Hz sweep injection	83
5.16	Spectrograms of the DARM and accelerometer responses to a 4-5 Hz sweep injection	84
6.1	BRDF of LIGO test masses	87
6.2	Schematic layout of equipment for driven measurements of beamtube backscatter	91
6.3	Ambient backscattering noise projections due to surface roughness and point defects on the surfaces of the test masses.	92
6.4	Low-frequency shaker setup for driven beamtube measurements	93
6.5	Backscattering noise projection made using data from driven measurements . .	95

6.6	Backscattering noise projection and upper limits for Cosmic Explorer	96
7.1	Strain sensitivities of LIGO Livingston (blue) and LIGO Hanford (green) during O3a.	99

ABSTRACT

The Advanced LIGO (aLIGO) detectors use 1064 nm lasers to measure the tiny fluctuations in spacetime that occur when gravitational waves pass through the earth. LIGO makes use of advanced coating methods and materials to limit the amount of light that scatters from the main beam, but some amount of light does scatter. This stray light can interact with surfaces inside the interferometer that are not seismically isolated and then recombine with the main beam, introducing excess noise into the gravitational wave channel. This thesis reviews the methods for modeling scattered light with ray tracing software and analytical models, for measuring scattered light with driven measurements of the vacuum enclosure, and for mitigating scattered light with baffles and changes to interferometer controls. It also details the process for finding correlations with auxiliary sensors in order to locate the sources of scattered light noise. The results of this work are improved sensitivity of the LIGO detectors in the frequency band from 20 Hz up to 200 Hz.

CHAPTER 1. INTRODUCTION

On September 14, 2015, the LIGO detectors in Livingston, LA and Hanford, WA made their first observation of gravitational waves from colliding black holes and ushered in the era of gravitational wave astronomy. The detectors looked for gravitational waves from September 2015 through January 2016 in what was the first observation run (O1) for LIGO. During O1, the detectors observed two more black hole-black hole mergers for a total of three events. For most of the rest of 2016, the detectors were down so that improvements to sensitivity could be made. From November 2016 through August of 2017, the detectors completed the second observing run (O2) during which seven more black hole mergers and one neutron star merger were observed. The detectors again underwent a series of improvements over the next 19 months before beginning the third observing run which was split into two parts (O3a and O3b) by a one month break for improvements. O3a ran from April 2019 until September 2019 and O3b ran from November 2019 until March 27, 2020 when operations were suspended due to Covid-19. Results from the third observing run are still being analyzed, but based on public alerts issued during the run, somewhere around 56 events were observed [1].

The LIGO detectors can sense changes in differential arm length on the order of $2 \times 10^{-20} \text{ m}/\sqrt{\text{Hz}}$ at around 200 Hz. This sensitivity corresponds to an estimated binary neutron star inspiral range, or range, of 134 Mpc for the Livingston Observatory and 111 Mpc for the Hanford observatory during O3 [2]. This range, sometimes called sensemon range, is one of several range definitions that are used in the field. It is averaged over source polarization, orientation, and sky position [3]. When the first detection was made in 2015, the range of the observatories was between 70-80 Mpc [4]. This range can be thought of as the radius of the observable volume, so improvements to the range are cubed when considering improvements to the observable volume. As the sensitivity, and thus range, improved, so too did the rate of detections as shown in Figure 1.1.

The sensitivity of a given instrument is limited by a combination of noise sources. Much

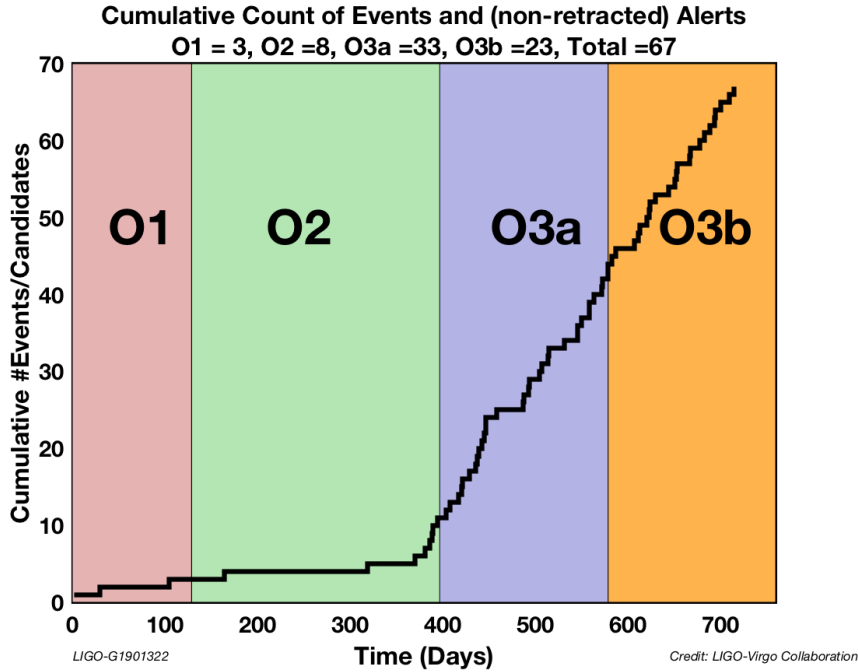


Figure 1.1. Cumulative number of detections and public alerts for the LIGO-Virgo network. The increase in the rate of detections over time corresponds with improvements to instrument sensitivity. The uptick at the end of O2 was not due to instrumental changes, but the stochastic nature of detections [1].

of the time between observing runs is spent installing new hardware and making adjustments to the interferometer to reduce the noise in the detector and to improve sensitivity. During the observing runs, scientists and engineers monitor data to identify new sources of noise and also design new hardware to be installed in the instrument when the observing run ends.

This dissertation focuses on the noise that arises from scattered light in the interferometer. All throughout the interferometer, at every location along the path of the main laser where the beam is reflected, a small amount of light scatters out of the main beam. This *scattered light* can then reflect from surfaces like the vacuum chamber walls that are not seismically isolated and then recombine with the main beam. When scattered light recombines with the main beam, it introduces noise into the gravitational wave channel.

In Chapter 2, we begin by reviewing gravitational waves in general relativity and discuss the types of events that can generate gravitational waves. We then discuss detecting gravitational waves with LIGO and the various noise sources that limit the sensitivity of LIGO.

In Chapter 3, we continue the discussion of detector noise by taking a closer look at noise from scattered light.

The next few chapters cover three different scattered light investigations. In Chapter 4 we review the design, installation, and performance of stray light baffles that were installed after the completion of the second observing run. While getting the detector ready for the third observing run, we began to notice scattered light noise that was correlated with the increase in ground motion due to daily human activity and the increase in ground motion from ocean waves. Chapter 5 reviews these investigations and the methods used to mitigate the noise.

The LIGO beamtubes are the 1.2 m diameter by 4 km long steel vacuum tubes through which the laser travels. When the beamtube was constructed, a series of baffles were placed inside the tube to prevent light from forward scattering along the tube to the test mass at the other end of the arm. Though the baffles fixed the problem of forward scattered light, they introduced the possibility of noise from light that back-scatters from the baffles and recombines with the main beam at the same test mass from which it originally scattered. In Chapter 6 we examine the problem in detail and present a set of measurements made to measure the noise. Chapter 7 provides a summary of this dissertation.

CHAPTER 2. GRAVITATIONAL WAVES

In November 1915, Albert Einstein published his general theory of relativity, which predicted gravitational waves. Prior to Einstein's theory, people like Henri Poincaré had theorized about the existence of gravitational waves. Einstein himself was not initially convinced that gravitational waves represented a physical phenomenon. He had determined that an exact analog to electrical waves, as proposed by Poincaré, was not possible due to the lack of a gravitational dipole moment [5]. At one point he became convinced that gravitational waves did not exist. He prepared a paper with the results stating this, but one of the reviewers found an error that made the conclusion invalid. Eventually, Einstein published an updated version of the paper that included a cylindrical gravitational wave solution to the equations of general relativity [6].

The first attempts at detecting gravitational waves were made by Joseph Weber in the 1960s. Weber used aluminum cylinders that were 66 cm diameter by 153 cm long to look for gravitational waves. A few groups around the world, including a group at LSU, developed their own Weber bars. Ultimately, the Weber bars were too insensitive to detect gravitational waves, but their development spurred further interest in the field. In 1979, Hulse and Taylor announced that they had found evidence for the emission of gravitational radiation from a binary pair of neutron stars. They observed a binary system containing a pulsar and found that the orbit of the system was contracting over time, consistent with the system losing energy to gravitational waves over time [7].

The idea to use laser interferometers for detecting gravitational waves was conceived independently by a few people in the 1960s. By the 1970s, people had begun building laboratory interferometers. In 1978, Robert Forward published a paper describing an experiment using an instrument with an effective arm length of 4.25 m. Forward operated his detector for 150 hours and found no events that were coincident with a number of Weber bars that were operating at the time [8]. During the 1970s and early 1980s, Rainer Weiss built a 1.5 m prototype at MIT, a group in Germany built first a 3 m then a 30 m instrument, and a

group in Glasgow led by Ron Drever built a 10 m interferometer. In 1983, a 40 m instrument was completed by Drever and others at Caltech. In the 1980s, groups began making plans for and seeking funding to build kilometer-scale interferometers. In 1983, a team from MIT with contributions from Caltech and work by Arthur D. Little and Stone and Webster Consultants completed the "Blue Book" survey on the feasibility of building a large scale interferometer [9].

In the 1990s, several large scale projects were approved and constructed. In Germany, construction on the GEO 600 detector (with 600 m long arms) was started in 1995. Construction on the 3-km VIRGO detector in Italy began in 1996. The 4-km LIGO detectors were started in 1994 at the Hanford, WA site and in 1995 at the Livingston, LA site. In 2012, work began on the underground, 3-km KAGRA detector in Japan.

In this chapter, we begin with a brief overview of gravitational waves in general relativity. We then examine how gravitational waves are generated in the universe before moving on to interferometric detection of gravitational waves. We look at the operating principles of LIGO and some of the noise sources that limit the sensitivity of LIGO. We end the chapter with a review of the discoveries made to date by LIGO and VIRGO.

2.1 General Relativity

General relativity describes how mass causes spacetime to curve and how gravity is a result of this curvature. The Einstein field equations we get from general relativity describe the relationship between matter and spacetime. These equations can only be solved exactly when simplified by symmetry. Fortunately for studying gravitational waves, we can further simplify things to *linearized gravity* which treats gravitational waves as small perturbations in flat spacetime.

We begin by considering the spatial distance, dl , between two points in flat, 3-dimensional

space. Using Euclidean geometry, we know that this distance can be written as:

$$dl^2 = dx^2 + dy^2 + dz^2 \quad (2.1)$$

In the early 20th century, Einstein published his special theory of relativity which showed that space and time are inseparable. Prior to Einstein, the distance and time between two events were thought to be independent and invariant. Special relativity said that the two were not independent, and that a new interval, *spacetime*, was the invariant. Minkowski introduced the following metric to describe the spacetime interval, ds , between two events:

$$ds^2 = -c^2 dt^2 + dx^2 + dy^2 + dz^2 \quad (2.2)$$

We can also write Equation 2.2 using Einstein notation:

$$ds^2 = g_{\mu\nu} dx^\mu dx^\nu \quad (2.3)$$

where $g_{\mu\nu}$ is the metric tensor, and in the flat (Minkowski) spacetime case where there is no gravitational field, $g_{\mu\nu} = \eta_{\mu\nu}$, where $\eta_{\mu\nu}$ is defined as:

$$\eta_{\mu\nu} = \begin{pmatrix} -c^2 & 0 & 0 & 0 \\ 0 & 1 & 0 & 0 \\ 0 & 0 & 1 & 0 \\ 0 & 0 & 0 & 1 \end{pmatrix} \quad (2.4)$$

When we include the effects of a gravitational field, spacetime is curved, $g_{\mu\nu} \neq \eta_{\mu\nu}$, and $g_{\mu\nu}$ can no longer be made diagonal. We can, however, consider the effects of a gravitational

wave traveling in the $+z$ direction by introducing a small perturbation, $h_{\mu\nu}$:

$$h_{\mu\nu} = \begin{pmatrix} 0 & 0 & 0 & 0 \\ 0 & a & b & 0 \\ 0 & b & -a & 0 \\ 0 & 0 & 0 & 0 \end{pmatrix} \quad (2.5)$$

such that $g_{\mu\nu} = (\eta_{\mu\nu} + h_{\mu\nu} + O[h_{\mu\nu}]^2)$ where we neglect the higher order terms. We can rewrite $h_{\mu\nu}$ as the sum of two components, $h_{\mu\nu} = ah_+ + bh_\times$ where:

$$h_+ = \begin{pmatrix} 0 & 0 & 0 & 0 \\ 0 & 1 & 0 & 0 \\ 0 & 0 & -1 & 0 \\ 0 & 0 & 0 & 0 \end{pmatrix} \quad (2.6)$$

$$h_\times = \begin{pmatrix} 0 & 0 & 0 & 0 \\ 0 & 0 & 1 & 0 \\ 0 & 1 & 0 & 0 \\ 0 & 0 & 0 & 0 \end{pmatrix} \quad (2.7)$$

h_+ and h_- form an orthogonal basis with which we can describe the polarization of a gravitational wave traveling in the $+z$ direction. h_+ describes the oscillation (shrinking and stretching of spacetime) that occurs along the x- and y-axes whereas h_\times describes a shrinking and stretching that occurs along axes that are rotated 45° from those of h_+ .

Using the metric, $g_{\mu\nu}$, from above, we can now examine the Einstein field equations:

$$R_{\mu\nu} - \frac{1}{2}Rg_{\mu\nu} + \Lambda g_{\mu\nu} = \frac{8\pi G}{c^4}T_{\mu\nu} \quad (2.8)$$

The Ricci tensor, $R_{\mu\nu}$, is a second order tensor providing information about spacetime cur-

vature and the stress-energy tensor, $T_{\mu\nu}$, provides information about the source of the curvature. The Ricci scalar, R is the trace of the Ricci tensor and Λ is the cosmological constant. Finally, G is the Newtonian gravitational constant and c is the speed of light.

In the weak field approximation far from the source, and using the transverse-traceless gauge, we can write the field equations in vacuum as:

$$\left(\nabla^2 - \frac{1}{c^2} \frac{\partial^2}{\partial t^2}\right) h_{\mu\nu} = 0 \quad (2.9)$$

This is a wave equation where $h_{\mu\nu}$ represents a gravitational wave propagating at the speed of light [10].

2.2 Sources of Gravitational Waves

As is the case with electromagnetic waves, we can study the generation of gravitational waves using the multipole expansion. For electromagnetic waves, monopole radiation is not possible due to conservation of electric charge. Gravitational monopole radiation would require a time varying change in the monopole moment, or a change in the total mass of the system. But conservation of energy tells us that this type of change is forbidden in an isolated system.

We next consider the gravitational dipole moments. We can construct a mass dipole moment in the following way [11]:

$$\mathbf{d} = \sum_{\text{particles } A} m_A \mathbf{x}_A \quad (2.10)$$

The first time derivative of this dipole moment gives the linear momentum of the system:

$$\dot{\mathbf{d}} = \sum_{\text{particles } A} m_A \dot{\mathbf{x}}_A = \mathbf{p} \quad (2.11)$$

The law of conservation of momentum tells us that $\dot{\mathbf{p}} = 0$, so there can be no mass dipole

radiation.

We can also create an analog to the magnetic dipole moment:

$$\mathbf{J} = \sum_{\text{particles } A} \mathbf{r}_A \times (m\mathbf{v}_A) \quad (2.12)$$

but this is the angular momentum of the system, and it must also be conserved, so there can be no gravitational dipole radiation.

The next moment to consider is the quadrupole moment:

$$I_{\mu\nu} \equiv \int dV (x_\mu x_\nu - \frac{1}{3} \delta_{\mu\nu} r^2) \rho(\mathbf{r}), \quad (2.13)$$

where $\rho(\mathbf{r})$ is the mass density. In the case where spherical or cylindrical symmetry is broken, the second derivative of the quadrupole moment is non-zero, and gravitational radiation is emitted [10]:

$$h_{\mu\nu} = \frac{2G}{Rc^4} \ddot{I}_{\mu\nu}, \quad (2.14)$$

where G is the gravitational constant, R is the distance from the source to the detector, and c is the speed of light. Any asymmetric acceleration of the mass in a system will create gravitational waves, but the coefficient on the right hand side of Equation 2.14 is very small, so only very massive systems can create waves capable of being detected.

An estimate for the amplitude of the gravitational wave produced by a binary neutron star system located in the Virgo cluster (a distance of $R \approx 15$ Mpc) is given in [10]. This estimate is proportional to the product of the Schwarzschild radii (r_s) and inversely proportional to the separation distance (r_0) and the distance to the observer (R):

$$h \approx \frac{r_{s,1} r_{s,2}}{r_0 R} \quad (2.15)$$

Assuming a mass of $1.4M_\odot$ for each of the neutron stars, the Schwarzschild radii ($r_s =$

$2GM/c^2$) would be $r_s \approx 5\text{km}$. When $r_0 = 20\text{ km}$,

$$h \approx 1 \times 10^{-21} \quad (2.16)$$

2.2.1 Compact binary coalescence

Two compact, massive objects (like black holes or neutron stars) in a binary system will radiate gravitational waves. As the objects orbit, energy leaves the system in the form of gravitational waves and the two objects move closer together with increasing orbital frequency until they merge. Radio astronomy observation of the first binary pulsar, *PSR 1913+16*, showed that the orbital period was decreasing at the rate predicted by general relativity [7]. In 2015, LIGO made the first direct observation of gravitational waves from a binary coalescence with *GW150914*. The binary system was comprised of two black holes with masses of $85_{-14}^{+21}M_\odot$ and $66_{-18}^{+17}M_\odot$ and it was located at a luminosity distance of $5.3_{-2.6}^{+2.4}\text{ Gpc}$. The peak gravitational wave strain for this event was $h = 1 \times 10^{-21}$ [12].

2.2.2 Supernovae

Core collapse supernovae are another potential source for generating gravitational waves. There are a number of scenarios that lead to core collapse supernovae [13], but the general idea is that any asymmetries in the mass distribution that arise during the collapse and bounce phases will give a time varying quadrupole moment and generate gravitational waves. The estimated gravitational wave energy emitted by core collapse supernovae ranges from 10^{-12} to $10^{-8} M.c^2$. The distance at which detectors like Advanced LIGO can expect to see signals from core collapse supernovae is less than 100 kpc. This distance means that signals from the Milky Way galaxy and Magellanic clouds could be detected [14].

2.2.3 Pulsars

Pulsars, and other rapidly rotating neutron stars, which have an asymmetric mass distribution will generate gravitational waves. The asymmetry comes from "mountains" on the surface of the neutron star. The search for pulsars in LIGO data look for pulsars that have been identified by radio and gamma ray observations which provide precise information about the position, rotational frequencies, and change in frequency over time. The LIGO searches have yet to yield a discovery, but they have helped to place upper limits on the size of the mountains, or the ellipticity, of the pulsars that have been targeted. Upper limits on the size of the mountains range from 50 cm to less than 0.1 mm [15].

2.2.4 Gravitational Wave Background

The cosmic gravitational wave background will have nearly constant amplitude and a broad continuous spectrum. All of the previously mentioned sources of gravitational waves are expected to contribute to the stochastic background. An additional source for the background are the quantum gravitational fluctuations that occurred just after the Big Bang. The search for the stochastic background involves cross-correlating the data taken from two detectors. The data from aLIGO's first observing run did not yield any evidence for the background but did set upper limits on the expected energy density of the background. For the frequency-independent (flat) background, the upper limit is $\Omega_{gw} < 6.0 \times 10^{-8}$ and for a background of compact binary coalescences, the upper limit is $\Omega_{gw} < 4.8 \times 10^{-8}$ [16].

2.3 Interferometric Gravitational Wave Detection

In a simple Michelson interferometer, such as the schematic representation in Figure 2.1, light passes through a beamsplitter and then travels down two perpendicular arms until it reaches the end mirrors. After reflecting from the end mirrors, the light travels back along the arms and recombines at the beamsplitter. Half of the light goes back towards the light source and the other half goes to the detection port. Depending on the travel time of the light

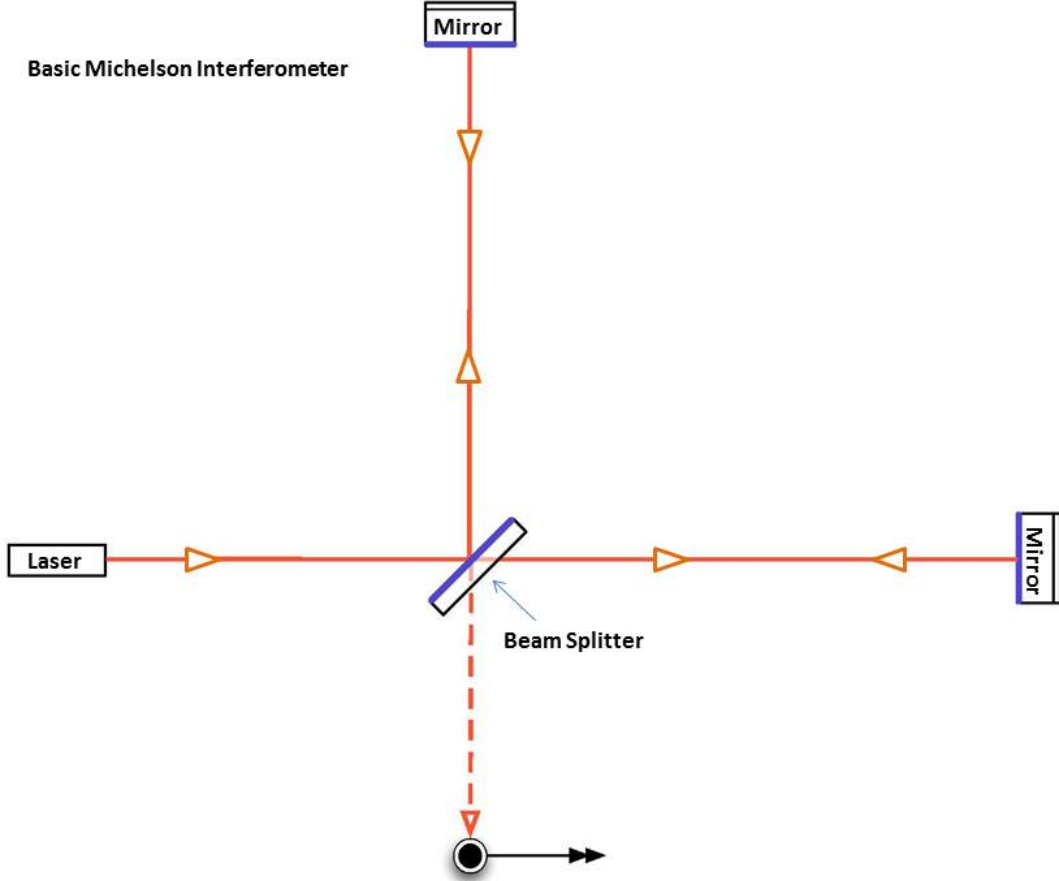


Figure 2.1. Schematic layout of a simple Michelson interferometer [17].

in the two arms, the light at the detection port can interfere constructively, destructively, or somewhere in between.

For light, the total spacetime interval, ds^2 is always zero. If we orient the arms of an interferometer along the \hat{x} and \hat{y} directions and consider a $+$ -polarized gravitational wave traveling in the \hat{z} direction, the spacetime interval for light traveling along the \hat{x} arm becomes:

$$ds^2 = 0 = g_{\mu\nu}dx^\mu dx^\nu = c^2 dt^2 - (1 + h \sin(kz - \omega t))dx^2. \quad (2.17)$$

Because $h \ll 1$,

$$cdt = \left[1 + \frac{h}{2} \sin(kz - \omega t) \right] dx \quad (2.18)$$

If the gravitational wave wavelength is much greater than the arm length, L , then the travel time of light is much less than the period of the wave: $\Delta t \ll 2\pi/\omega$, we can simplify the integral for Δt :

$$\Delta t = \left(1 - \frac{h}{2} \sin \omega t\right) \frac{L}{c} \quad (2.19)$$

When there is no gravitational wave, the travel time is, as expected, $\Delta t = L/c$. The gravitational wave causes a change in the travel time:

$$\delta \Delta t = \left(\frac{h}{2} \sin \omega t\right) \frac{L}{c}. \quad (2.20)$$

The change in arm length as measured by the light is $\Delta L = c\delta\Delta t$ and the *strain* is then:

$$\frac{\Delta L}{L} = \frac{h}{2} \sin \omega t \quad (2.21)$$

The \hat{y} arm sees an opposite change in travel time and the path back from the mirror to the beamsplitter double the effect, so the apparent length change seen by a Michelson interferometer is [18, 19]:

$$\frac{\Delta L}{L} \approx h \quad (2.22)$$

Using the result from Equation 2.16 and the LIGO arm length ($L = 4\text{ km}$), a gravitational wave from coalescing neutron stars in the Virgo cluster would correspond to an arm length change of $\Delta L \approx 4 \times 10^{-18}\text{ m}$.

2.4 Laser Interferometer Gravitational Wave Observatory

The Laser Interferometer Gravitational-wave Observatory (LIGO) detectors are dual recycled, Fabry-Perot, Michelson interferometers located in Livingston, LA and Hanford, WA. Figure 2.2 is a schematic representation of a LIGO interferometer. Dual recycled refers to the power- and signal-recycling cavities of the LIGO detectors. The power-recycling cavity sends light that would normally be reflected back towards the laser and thus not utilized

back into the interferometer and increases the circulating power. The signal-recycling cavity allows the bandwidth of the interferometer to be tuned. Fabry-Perot cavities formed by the input (ITMs) and end test masses (ETMs) increase the effective arm length and the amount of interaction time between passing gravitational waves and light in the arms.

2.4.1 Detecting Gravitational Waves

Ultimately, it is the differential arm length (DARM) degree of freedom that is used by LIGO to detect passing gravitational waves. LIGO uses a DC readout scheme to sense the changes in differential arm length due to passing gravitational waves. This scheme is achieved by holding the length of the arms on the order of 10 pm away from resonance so that the photodiode signal responds linearly to the arm length changes, rather than being proportional to ΔL^2 .

In order for the DARM degree of freedom to have the required sensitivity, a number of auxiliary degrees of freedom must also be precisely controlled. The method used to control the lengths of the auxiliary degrees of freedom is the Pound-Drever-Hall technique [20]. This technique uses radio frequency sidebands added to carrier light to detect the length of a cavity. The resulting error signal gives information on how far away from resonance the carrier is in the cavity and can be used in a feedback loop to adjust either the length of the cavity or the frequency of the laser or both. Closing this feedback loop is called locking the cavity because the frequency of the laser is now locked to the cavity length, and a locked cavity can be used as a stable reference for another cavity. Differential-mode degrees of freedom (DoFs) are generally controlled using signals similar to the output of Michelson interferometers. Finally, the error signals for angular DoFs are obtained with measurements similar to the length DoFs as measured differentially across the beam. In LIGO, bringing the instrument up to full sensitivity requires locking a sequence of cavities before the DARM servo can be engaged [4, 2].

2.4.2 Noise Sources

The output of the LIGO detectors is the combination of the gravitational wave signal (or lack thereof) and noise present in the detector [21]. By decreasing the amount of noise, the sensitivity of the instrument is increased. Noise in the detector comes from a variety of sources. We can use a noise budget like the one shown in Figure 2.3 to examine the contributions from the various noise sources across the frequency range of the interferometer. At high frequencies, LIGO is quantum shot noise limited. At lower frequencies, a combination of actuator and control noises dominate. In the middle, around 100 Hz, thermal noise and scattered light noise are the largest contributors to the noise floor.

Quantum Noise

Quantum fluctuations of the optical vacuum field enter the interferometer through the anti-symmetric port and fundamentally limit the sensitivity of the instrument. These quantum fluctuations create both shot noise and radiation pressure noise [22, 23]. In this section, we will review quantum noise for a simple Michelson interferometer. In the actual LIGO interferometer, the noise is complicated by the interferometer response including recycling cavities, resonant cavities, and optical losses. For a more complete description of quantum noise in the LIGO detectors, see [24].

The photodetector at the output port measures changes in optical power due to gravitational waves by counting the number of photons that arrive in a given time interval. This photon arrival rate is approximately governed by Poisson statistics. Given a time interval, τ , the number of photons, N , that arrive in that interval are given by $N = n\tau$ where n is the arrival rate. We can approximate the Poisson distribution with a Gaussian distribution that has a standard deviation equal to the square root of the total number of photons. We can then write the precision of a measurement as:

$$\frac{\sigma_N}{N} = \frac{\sqrt{n\tau}}{n\tau} = \frac{1}{\sqrt{n\tau}} \quad (2.23)$$

Or, in terms of power:

$$\frac{\sigma_N}{N} = \sqrt{\frac{4\pi\hbar c}{\lambda P_{in}\tau}} \quad (2.24)$$

where P_{in} is the input power. We are free to choose the operating point of the interferometer to be anywhere from $P_{out} = P_{in}$ (bright fringe) to $P_{out} = 0$ (dark fringe), but the general result is that *photon shot noise* in units of gravitational wave strain for a simple Michelson interferometer is inversely proportional to the square root of the input power:

$$h_{shot}(f) = \frac{1}{L} \sqrt{\frac{\hbar c \lambda}{2\pi P_{in}}} \quad (2.25)$$

This expression is frequency independent, so shot noise is white. Increasing input power decreases the shot noise and increases instrument sensitivity across all frequencies, but other effects must also be considered.

The conjugate phenomenon to shot noise is the fluctuating radiation pressure that impacts the test masses in the interferometer. The force on the mirror from light reflecting off of it is:

$$F_{rad} = \frac{P}{c} \quad (2.26)$$

The fluctuation of this force is due to the fluctuation in P :

$$\sigma_F = \frac{1}{c} \sigma_P \quad (2.27)$$

The force from the radiation pressure causes each test mass to move with the following frequency dependent spectrum:

$$x(f) = \frac{1}{m(2\pi f)^2} F(f) \quad (2.28)$$

The power fluctuations in the arms are anti-correlated, and since the interferometer is sensitive to differential displacements, the effect on the noise is doubled. Radiation pressure

noise in units of gravitational wave strain for a simple Michelson interferometer is then:

$$h_{rp}(f) = \frac{2}{L}x(f) = \frac{1}{mf^2L}\sqrt{\frac{\hbar P_{in}}{2\pi^3 c \lambda}} \quad (2.29)$$

We see that this radiation pressure noise is frequency dependent and proportional to the input power. So an increase in power will reduce shot noise but increase radiation pressure noise. The $1/f^2$ frequency dependence of the radiation pressure noise means that it dominates at lower frequency and shot noise dominates at higher frequencies.

Prior to the third observing run, a couple of steps were taken to reduce the effects of quantum noise. First, a squeezed light injection system was installed [24]. Squeezed light injection allows reducing one quantum component (in this case shot noise) while increasing the other (radiation pressure). Second, the input laser power was increased, which, as we can see in Equation 2.25, reduces shot noise as the square root of the power increase. The improved sensitivity from these upgrades can be seen in Figure 2.3 when comparing the measured sensitivity from the first two observing runs with the sensitivity from the third observing run. The improvement from squeezing alone led to a 12% and 14% increase in binary neutron star inspiral range at LIGO Hanford and Livingston, respectively. Future upgrades will allow for frequency-dependent squeezing so that at lower frequencies, radiation pressure can be reduced (and shot noise increased) while at higher frequencies, shot noise is lowered at the expense of increased radiation pressure noise. Increased input laser power is also planned.

Thermal Noise

Thermal motion couples to the gravitational wave channel as displacement noise. The noise can come from the test mass suspensions, coatings, and substrates.

Thermal noise levels are calculated by measuring the mechanical losses of materials and then using the fluctuation-dissipation theorem to compute the thermal fluctuations [25, 26].

The dominant thermal noise term is coating Brownian noise, which causes a change in arm cavity length. The source of this noise is mechanical dissipation in the mirror coatings. The aLIGO mirror coatings are made by ion-beam sputtering alternating layers of SiO_2 and $Ti-TaO_5$ (titanium doped tantalum pentoxide) [27]. Once coated, the mirrors are polished to limit power loss in the arms. The target for round trip losses is 75 ppm, which gives a potential power buildup in the arms of $1/75\text{ ppm} = 1.3 \times 10^4$ times the input power.

Thermal noise also comes from the substrate of the optics. The contribution from the test masses is small, but a contribution from the composite signal-recycling mirror (SRM) in the second observing run led to it being replaced by a monolithic mirror prior to the third observing run. Changing from the aluminum and fused-silica composite to the monolithic fused-silica SRM eliminated that source of thermal noise [2].

Thermal motion of the suspension fibers is transferred to the test masses and results in thermal noise. The suspension fibers are welded to silica ears attached to the 40 kg test mass and penultimate mass. The fibers are constructed to minimize the noise transmitted in the sensitive band of the interferometer. The most visible feature from the suspension fibers are the *violin modes*. The violin modes of the suspension fibers are actively damped, but still show up in the gravitational wave channel at around 500 Hz and harmonics.

Seismic Noise

As mentioned in the previous section, the test masses are suspended from silica fibers. These silica fibers form a 4-stage pendulum and offer passive seismic isolation that goes as $1/f^8$ above the suspension resonances at around 0.4Hz. In addition to the passive isolation, each stage of the suspension can be actively damped. The upper 3 stages are damped by optical shadow sensor and magnetic actuators (OSEMs) and the bottom stage of the end test masses can be actuated on by an electro-static drive. The structure from which the suspension hangs is mounted to an optical table with multiple stages of active and passive seismic isolation as shown in Figure 2.4. Two levels of isolation are provided by the internal

seismic isolation (ISI) system and an additional layer of isolation comes from the hydraulic external pre-isolator (HEPI) system. The result of all of this seismic isolation is that by the time the ground motion is transferred to the test masses, it has been reduced by as much as ten orders of magnitude [28]. Another way to consider this impressive performance is by looking at the noise budget in Figure 2.3 and seeing that the seismic noise contribution lies far below noise floor of the interferometer.

Residual Gas Noise

Other than the pre-stabilized laser system, all of the rest of the core components of LIGO lie inside the vacuum system. There are vacuum chambers called Basic Symmetric Chambers (BSCs) that house the test masses and a series of smaller Horizontal Access Module (HAM) chambers that house the smaller optics like the power- and signal-recycling mirrors. There are also a series of vacuum tubes that connect the various chambers to each other, including the two 4-km long, 1.2-m diameter beamtubes that make up the arms of the interferometer. Pressure inside the vacuum system is held as low as 1×10^{-9} Torr by ion pumps placed throughout the vacuum system and by liquid nitrogen cryogenic pumps located at both ends of each arm. The pumps must operate constantly to overcome the outgassing from components placed inside the vacuum system and from any leaks that may be present in the system. Any residual gas in the vacuum system can cause phase and/or gas damping noise in the interferometer.

Gas molecules that pass through the beam of the interferometer change the phase of the light and introduce noise into the gravitational wave channel. This effect can be modeled as the impulse disturbance to the phase of the laser field as a gas molecule passes through the field and then integrating over all of the particles in the interferometer [30]. The result is a noise that is mostly white. Phase noise is the dominant source of residual gas noise above approximately 60 Hz.

A leak in the LIGO Livingston X-arm beamtube had caused pressures to rise from a few

nanotorr to tens of nanotorr. The leak was pinpointed during the O3 commissioning break in October 2019 and subsequently repaired. A measurement of interferometer noise taken before the leak was fixed showed excess noise from 400-1000 Hz which would be consistent with excess gas phase noise [2].

The other way that residual gas creates noise is through squeezed film damping. The Advanced LIGO End Test Masses (ETMs) were separated by only 5 mm from the End Reaction Masses (ERMs) behind them. The proximity of the two surfaces makes it easy for residual gas to accumulate. One way to think about the noise is that if the ETM moves closer to the ERM, some of the residual gas is squeezed out of the space between. This leads to a pressure drop and an associated force on the ETM. Another way to think about the noise is to consider the repeated impacts of gas molecules as they traverse the gap. Modeling has shown both methods to be equivalent. Gas damping noise is frequency dependent and drops off as $1/f^2$. [31]

Prior to the start of O3, the ERMs were replaced with Annular End Reaction Masses (AERMs) which have a hollow center section such that the face seen by the ETM looks like a donut. This shape reduces the surface area in the gap, and reduces the force generated by residual gas. The change to AERMs is expected to have reduced gas noise below 100 Hz by a factor of 2.5 [2].

Scattered Light

As the main beam works its way from laser to output port, each time it encounters an optical component in its path, a small amount of light scatters out of the main beam. This *scattered light* introduces both phase and radiation pressure noise into the gravitational wave channel. We can write down a simple formula for the noise introduced by scattered light [32]:

$$h_{scat}(f) = \sqrt{\frac{P_{scat}}{P_{main}}} TF \cdot x_{scat}(f) \cdot 2k \quad (2.30)$$

where P_{scat} and P_{main} are the power in the scattered and main beams respectively, TF is the optical transfer function from the mirror at which the scattered light recombines with the main beam to the output port, x_{scat} is the amplitude of the displacement of the scattering surface at a given frequency, f , and k is the wavenumber of the light in the interferometer. Every mirror in the interferometer is a source of scattered light and every surface, from suspension components to vacuum chambers, can be a scattering surface. This makes measuring scattered light noise very difficult, since, as we can see from Equation 2.30, we need to know not only how much each surface is moving, but also how much power is incident on that surface. And measuring the motion directly is not always helpful, as it is the relative motion between the scattering surface and the scattering mirror that is important. So a particular vacuum chamber may be moving only as much as the ground on which it sits, but the optic inside the vacuum chamber may be following an optic in another chamber via active feedback control loops, so the relative motion may be large.

Finding and mitigating scattered light is largely an iterative process. Areas with high coupling of scattered light to the gravitational wave channel are identified by looking for correlation between sensors like accelerometers and seismometers and noise in the gravitational wave channel and also by performing tests where mechanical shakers are used to increase the motion of the vacuum chambers. Once an area is identified, a mitigation strategy is developed. This could include installing baffles to absorb and/or deflect the scattered light or changing the control scheme of the interferometer to reduce the relative motion. Once mitigation has been put in place, the tests are repeated to quantify any improvements. If the source is properly mitigated, then the process repeats by finding the next loudest source of scattered light noise.

2.5 Observations

On 14 September 2015, the LIGO detectors made the first observation of gravitational waves from a binary black hole merger. Another black hole merger was observed on 26

December 2015 and a third event was detected on 12 October 2015 [33]. These observations were made during the first LIGO observing run (O1) which ran from September 2015 through January 2016.

The first detection, GW150914, was a result of two black holes colliding 410^{+160}_{-180} Mpc away. The two black holes were $36^{+5}_{-4}M_{\odot}$ and $29^{+4}_{-4}M_{\odot}$ and the resulting black hole was $62^{+4}_{-4}M_{\odot}$. $3.0^{+0.5}_{-0.4}M_{\odot}c^2$ was radiated away in the form of gravitational waves [34]. The signal seen by LIGO lasted approximately 0.2 seconds and swept up in frequency from around 35 Hz up to 150 Hz [12].

The second observing run (O2) started on 30 November 2016 and ended 25 August 2017. During the run, 3 more binary black hole mergers were detected: GW170104 [35], GW170608 [36], and GW170814 [37]. GW170814 was the first detection made by a 3 detector network with the VIRGO detector joining the LIGO detectors in the observation. The addition of the 3rd detector improved the sky localization of the source from 1160 deg^2 to 60 deg^2 .

On 17 August 2017, the LIGO and VIRGO detectors detected gravitational waves from a binary neutron star inspiral for the first time [38]. At the time of the detection, named GW170817, the source was in a 'blind spot' for the VIRGO detector, so the signal did not show up in the VIRGO data, but this lack of signal helped improve the sky localization to 28 deg^2 . Shortly after the signal passed through the gravitational wave detectors, a γ -ray burst was detected by the FERMI Gamma-ray Burst Monitor. The first optical counterpart was observed 11 hours later by the SWOPE telescope and a campaign of electromagnetic observations continued over the following weeks and months [39].

The third observing run (O3) is divided into two parts. O3a ran from April 1 until September 30, 2019 and O3b ran from November 1, 2019 until March 27, 2020, when operations were forced to stop by Covid-19. During O3, 56 candidate gravitational wave events were identified through open public alerts to the astronomical community [2]. Analysis is ongoing at the time of writing, but a few notable events have been reported in journals.

GW190425 was a binary neutron star merger that was seen by LIGO Livingston. LIGO

Hanford was not operating and the VIRGO signal was too weak to aid in detection, but it was used for parameter estimation. The signal seen by LIGO Livingston lasted for 128 seconds and swept up in frequency from 19.4-2048 Hz. The binary system is unique in that the total mass of the system (3.3-3.7 times the mass of the Sun) is larger than any other known binary neutron star systems [40].

GW190412 [41] and GW190814 [42] were events whose binary systems had asymmetric masses. Because of the mass difference, these types of systems will emit gravitational radiation that, while still dominated by the quadrupole, will contain higher multipoles. For both events, this was found to be the case providing yet another verification of general relativity. GW190814 was unique not just because its mass ratio was the most uneven measured to date, but also because the smaller object had a mass of $2.59^{+0.08}_{-0.09} M_{\odot}$. It was most likely a black hole, but it could have been a neutron star. In either case, it was either the largest neutron star or the smallest black hole found in a double compact-object system [42].

The signal from GW190521 lasted 0.1 s and swept from 30-80 Hz with peak strength at 60 Hz. This peak frequency suggested that it came from a massive system. Analysis showed that the component masses were $85^{+21}_{-14} M_{\odot}$ and $66^{+17}_{-18} M_{\odot}$ and the total mass was $150^{+29}_{-17} M_{\odot}$. GW190521 is the heaviest binary black hole system ever observed and the remnant black hole is the first intermediate mass black hole ever observed [43]. Since this event lacked gravitational wave energy at high frequencies, its detection relied on LIGO's sensitivity in the frequency range affected by noise from scattered light, the main subject of this dissertation.

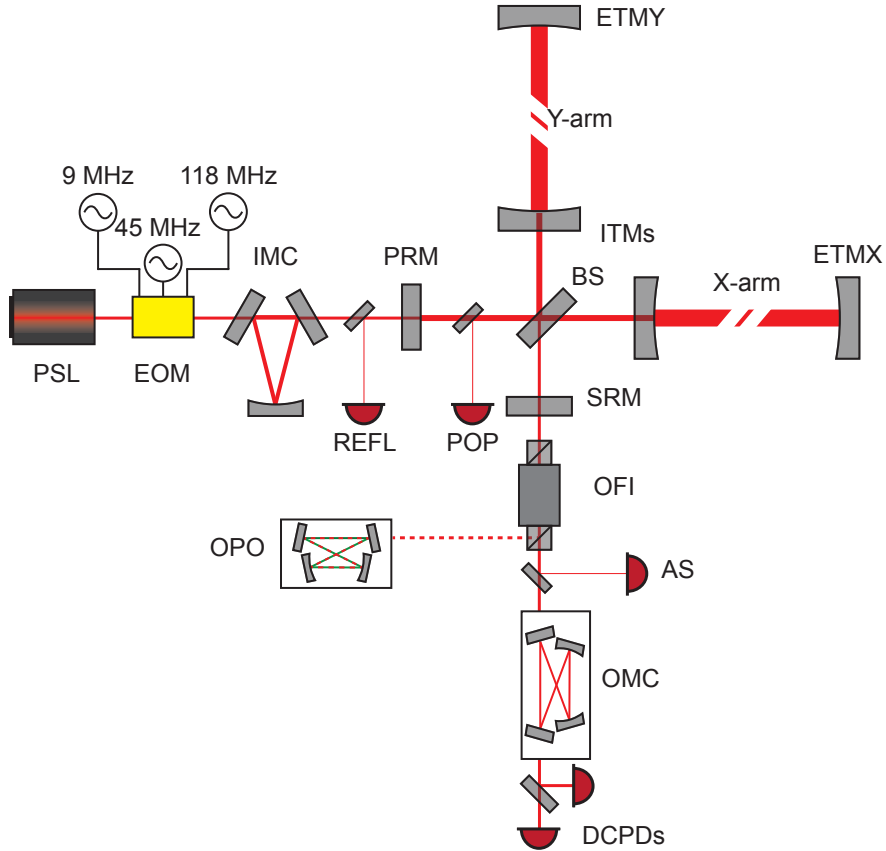


Figure 2.2. Schematic layout of a LIGO interferometer. The laser originates with the pre-stabilized laser (PSL). An electro-optical modulator (EOM) adds radio sidebands which are used for interferometer controls. The beam then passes through the input mode cleaner (IMC) where the beam profile is cleaned up. The input test masses (ITMs) and end test masses (ETMs) make up the arm cavities. The power-recycling mirror (PRM) and signal-recycling mirror (SRM) are part of the power- and signal-recycling cavities respectively along with the ITMs and the beamsplitter (BS). The reflected power photodiode (REFL) senses light coming back from the interferometer and the power-recycling pick-off (POP) senses light coming from the PSL. The output Faraday isolator (OFI) only allows light to pass from the interferometer to the output port and not vice versa. The OFI also serves as the location where squeezed light is injected via the optical parametric oscillator (OPO). The output mode cleaner (OMC) removes the sidebands from the carrier light and the output photodiodes (DCPDs) sense the change in carrier light caused by changes in differential arm length. [2]

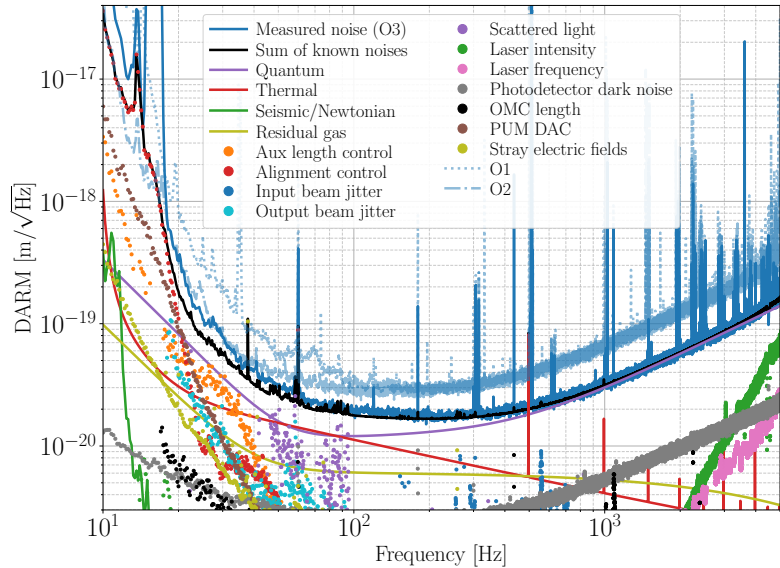


Figure 2.3. LIGO Livingston noise budget during the third observing run [2].

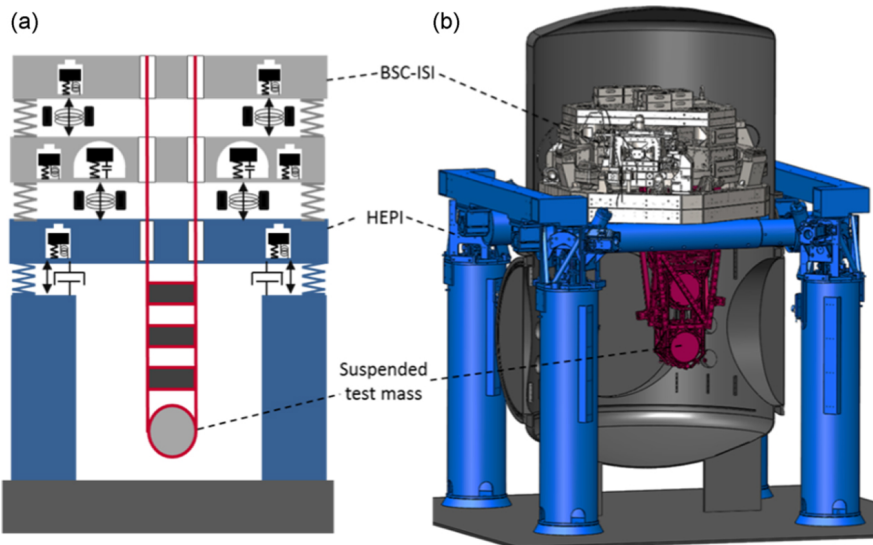


Figure 2.4. A schematic and CAD representation of the LIGO seismic isolation systems. The test masses have up to 7 layers of isolation from 3 different systems. The first layer of isolation comes from the hydraulic external pre-isolator (HEPI) system. The next two levels of isolation are provided by the internal seismic isolation (ISI) system. From the ISI optical table, the quadruple stage pendulum suspension is hung, providing the final four layers of isolation [29].

CHAPTER 3. NOISE FROM SCATTERED LIGHT

3.1 Introduction

The simplest picture for scattered light noise involves three events: light scatters from some *scattering mirror*, light reflects from some *scattering surface*, and light re-combines with the main beam at the original scattering mirror. The scattering surface is moving relative to the optical cavity, so the scattered light picks up phase noise due to the path length modulation. The scattered field interferes with the static field in the interferometer and causes power fluctuations, so scattered light also causes radiation pressure noise.

Light can scatter from the main beam for a number of reasons; surface imperfections lead to even high-quality mirrors scattering small amounts of light in non-specular directions. The middle panel in Figure 3.1 shows BRDF scatter. Light hits the mirror and then scatters according to the Bi-directional Reflectivity Distribution Function (BRDF). The BRDF is either the measured or modeled distribution of scattered light reflecting from a mirror. Highly polished surfaces like the LIGO test masses generally have a BRDF with an angular dependence whereas scattering surfaces like vacuum chamber walls have a constant BRDF. The third panel shows a ghost beam reflecting from the anti-reflective (AR) coating on the rear of the mirror. The front surface of the mirror has a highly-reflective (HR) coating which reflects most of the light (anywhere from 50% reflected to only a few ppm transmitted), but some amount of light is transmitted through the coating. The rear surface has been AR coated to limit the amount of light reflected, but some light will reflect. An additional source of scatter is the Gaussian tail of the laser beam. The beam radius is defined as the distance out to which the intensity has dropped to $1/e^2$. The optics are sized larger than the beam radius, and baffles are installed to limit the Gaussian tail, but as we will see in Chapter 5, this light from the Gaussian tail can cause noise.

The differential motion between scattering surface and scattering mirror is due to a combination of seismic motion of the scattering surface and the interferometer controls pushing

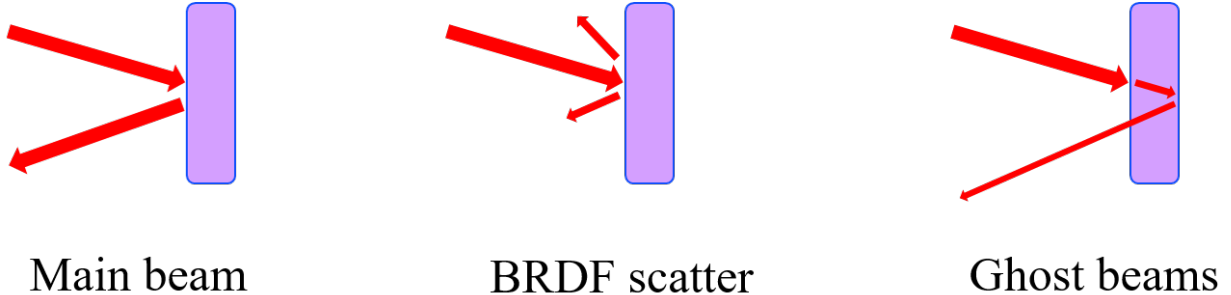


Figure 3.1. Illustration showing how scattered light originates. BRDF scatter is from imperfections on the highly-reflective coating on the mirror. Ghost beams originate when light reflects from the anti-reflective coating on the rear of the optic.

the scattering mirror relative to the scattering surface. This differential motion usually cannot be measured directly, so sensor data has to be propagated through a model to obtain an estimate for the differential motion.

In the following sections, we will derive an expression that allows us to express the noise from scattered light in terms of the effective gravitational wave strain, h_{eff} , necessary to generate the same signal.

3.2 Effects of Gravitational Waves and Scattered Light on a Complex Electric Field

We can approximate the light circulating in the arms (ignoring things like the Fabry-Perot storage time and spatial filtering of the arm cavities) as a complex electric field:

$$E(x, t) = E_0 \exp(i(\omega t - kz + \phi(t))) \quad (3.1)$$

where E_0 is the amplitude of the field in the arm cavity, ω is the angular frequency, $k = \frac{2\pi}{\lambda}$ is the laser wave number, z is the distance to an arbitrary plane of reference, and $\phi(t)$ is the phase due to some external source such as gravitational waves or scattered light. If we consider a simple sinusoidal motion with amplitude ϕ_m and frequency ω_m and assume that

$z = 0$, then the field in the cavity is:

$$E(t) = E_0[i\omega t] \sum_{n=-\infty}^{\infty} i^n J_n(\phi_m) \exp[in\omega_m] \quad (3.2)$$

where we've used the Bessel function expansion identity. If we consider a gravitational wave, the strain, h , will cause a test mass displacement of $x_G = hL$ where L is the arm length of the interferometer. The resulting phase shift caused by the gravitational wave will be $\phi_G = 2kx_G$. For a gravitational wave, this phase shift will be small such that $\phi_G \ll 1$. This means that in Equation 3.2, only the $n = 0, \pm 1$ terms are appreciable and we can approximate it as a phase modulation:

$$E_G(x, t) \simeq E_0 \exp[i\omega t] (1 + ikx_G \exp[\pm i\omega_G t]) \quad (3.3)$$

The field from scattered light carries phase noise due to the path length modulation that results from the differential motion of the scattering surface. The scattered field takes on the form of Equation 3.2, but has an additional amplitude transfer coefficient, A , which takes into account the fact that only a portion of the light in the main beam scatters:

$$E_{scat}(t) = AE_0[i\omega t] \sum_{n=-\infty}^{\infty} i^n J_n(\phi_{scat}) \exp[in\omega_{scat}], \quad (3.4)$$

where $\phi_{scat} = 2kx_{scat}$ and x_{scat} is the amplitude and ω_{scat} is the frequency of the displacement of the scattering surface. When $kx_{scat} \ll 1$, we get a phase modulation as in the gravitational wave case. When $kx_{scat} \gg 1$, the Bessel functions up to $n \approx 2kx_{scat}$ must be considered. The result is that there will be sidebands at frequencies up to $\omega_{max} = 2kx_{scat}\omega_{scat}$ [44].

3.3 Amplitude Transfer Coefficient

We can express the amplitude transfer coefficient, A , in Equation 3.4 in terms of power in the scattered and interferometer beams:

$$A^2 \equiv \frac{\delta I}{I} \quad (3.5)$$

Though it is the ratio of the fields that determines the noise in the gravitational wave channel, it is often easier to work with the power when determining the amplitude transfer coefficient. The coefficient will be different based on where in the interferometer the scattering takes place.

One example, discussed in Chapter 6 involves light scattering from a test mass, then scattering from a baffle, and then re-combining with the main beam. In this case, we have three scatter events that we need to consider: BRDF scatter from the test mass, BRDF scatter from the baffle, and BRDF scatter from the test mass. The ratio of power is then:

$$\begin{aligned} \frac{\delta I}{I} &= \beta_{\text{mir}} \cdot \beta_{\text{baf}} \cdot \beta_{\text{mir}} \cdot \frac{d\Omega}{r^2} \\ &= \beta_{\text{mir}}^2 \beta_{\text{scat}} \frac{d\Omega}{r^2}, \end{aligned} \quad (3.6)$$

where β_{mir} and β_{baf} are the BRDFs of the test mass and baffle respectively, $d\Omega$ is the solid angle subtended by the baffle, and $r = R/\sin\theta$ is the distance from the mirror to the backscattering surface. For the mirrors, the BRDF is evaluated by a beam with normal incidence and for the baffles, the BRDF is integrated over the range of appropriate incidence angles.

Another example that we will consider in Chapter 5 is light that is transmitted through the test mass, reflected from the reaction mass, and transmitted again through the test mass to re-combine with the main beam. In this case, we need to consider the power transmission of the test mass, T_{tm} , and also need to know how much power is reflected from the reaction

mass, R_{rm} . The power ratio in this case is:

$$\begin{aligned}\frac{\delta I}{I} &= T_{\text{tm}} \cdot R_{\text{rm}} \cdot T_{\text{tm}} \\ &= T_{\text{tm}}^2 R_{\text{rm}},\end{aligned}\tag{3.7}$$

For this example, the integral over the Gaussian tail of the beam has been included in the reaction mass reflection term.

3.4 Transfer Functions

We have an expression for the scattered light electric field. We are interested in how scattered light affects interferometer output, so we need to convert this scattered field into units of interferometer output. We want to know the equivalent gravitational wave strain, h_{eff} , that would generate the same signal in the interferometer output as the scattered light. To do this, we use transfer functions that take the phase and amplitude noise (expressed as Relative Intensity Noise (RIN)) of the scattered field to the effective strain.

3.4.1 Phase Noise

As we saw earlier, a passing gravitational wave adds a phase shift $\phi_G = 2kx_G$ on the main beam. From Equation 3.3 we can see that a passing gravitational wave adds the following field to the main beam:

$$\delta\psi_{mb} = i2k\delta L\psi_{mb}\tag{3.8}$$

In the case of a gravitational wave, $\delta L = hL$, we can write:

$$\frac{\delta\psi_{mb}}{\psi_{mb}} = i(2kL)h.\tag{3.9}$$

Similarly, we can use Equation 3.4 to write the scattered field added to the main beam:

$$\frac{\delta\psi_{mb}}{\psi_{mb}} = \left(\frac{\delta I}{I}\right)^{1/2} e^{i\phi_{scat}} = \left(\frac{\delta I}{I}\right)^{1/2} (\cos\phi_{scat} + i\sin\phi_{scat}). \quad (3.10)$$

If we compare Equations 3.9 and 3.10, we see that the imaginary part of Equation 3.10 has the same form as the signal from the gravitational wave. We can solve for h and find an expression for the scattered light that adds phase noise to the main beam as the ratio $\frac{\delta I}{I}$ and is read out from a LIGO arm as though it were a gravitational wave signal $h(t)$ [45]:

$$h(t) = \left(\frac{\delta I}{I}\right)^{1/2} S(t) \left(\frac{\lambda}{4\pi L}\right), \quad (3.11)$$

where $S(t) = \sin\phi_{scat}(t)$. We can now relate the spectral density of the effective strain noise, $\tilde{h}(f)$, to the spectral density of $\tilde{S}(f)$ by taking the Fourier transform of $S(t)$:

$$\tilde{h}_{\text{phase}}(f) = A \left[\frac{h_{\text{eff}}}{\Phi} \right] \tilde{S}(f), \quad (3.12)$$

where A is again the amplitude transfer coefficient and we have used the transfer function from phase noise to effective strain:

$$\frac{h_{\text{eff}}}{\Phi} = \frac{1}{2} \frac{\lambda}{4\pi L} \quad (3.13)$$

The scattered field will split between the common and differential degrees of freedom. Only the differential degree of freedom is sensed by the gravitational wave channel, so the factor of $\frac{1}{2}$ in Equation 3.13 is added to account for this [46].

3.4.2 Amplitude Noise

The amplitude quadrature of the scattered field is represented by the real part of Equation 3.10. The scattered field builds up with the cavity signal gain, Γ , and the total field is:

$$\psi_{\text{mb}} + \delta\psi_{\text{mb}}\Gamma = \psi_{\text{mb}}(1 + (\delta I/I)^{1/2}\Gamma \cos \phi_{\text{scat}}) \quad (3.14)$$

The modulus square of the total field gives us the total power. The changing part of the power is then:

$$\delta P = 2P_0(\delta I/I)^{1/2}\Gamma C(t), \quad (3.15)$$

where $C(t) = \cos \phi_{\text{scat}}(t)$. The power fluctuation leads to a changing force on the test masses, displacing them as a result. The force is $F_{\text{scat}} = 2\delta P/c$ so we need to divide out the mass of the test mass, M , to get the acceleration and then divide twice by the angular frequency, $2\pi f$, to get the displacement. We can now obtain the effective strain noise spectrum [47]:

$$\begin{aligned} \tilde{h}_{\text{rad}}(f) &= \frac{2}{M(2\pi f)^2} \frac{2\delta\tilde{P}}{cL} \\ &= A \left[\frac{h_{\text{eff}}}{RIN} \right] \tilde{C}(f), \end{aligned} \quad (3.16)$$

where we have defined the radiation pressure transfer function in terms of relative intensity noise (RIN) as:

$$\frac{h_{\text{eff}}}{RIN} = 2P_0 \frac{\Gamma}{M} \frac{2}{cL} \frac{1}{(2\pi f)^2}, \quad (3.17)$$

3.5 Equivalent Strain Noise

We can now express the effective strain noise from scattered light with the following equation:

$$\tilde{h}_{\text{eff}}(f) = A \left[\frac{h_{\text{eff}}}{\Phi} \right] \tilde{S}(f) + A \left[\frac{h_{\text{eff}}}{RIN} \right] \tilde{C}(f) \quad (3.18)$$

3.6 Upconversion from Fringe Wrapping

The type of noise created by scattered light depends on the RMS displacement of the scattering surface relative to the optical cavity. If the displacement is less than the wavelength of the laser, then the noise seen in the detector is linear and appears at the same frequency as the motion. If the displacement, however, is larger than the wavelength of the laser, then *fringe wrapping* occurs and the noise is *upconverted* to higher frequencies. We can see the non-linearity in the terms $\tilde{S}(f)$ and $\tilde{C}(f)$ (used previously in Equations 3.12 and 3.16 respectively):

$$\tilde{S}(f) = \int_{-\infty}^{\infty} \sin\left(\frac{4\pi x_{scat}(t)}{\lambda}\right) \exp(i\omega t) dt, \quad (3.19)$$

$$\tilde{C}(f) = \int_{-\infty}^{\infty} \cos\left(\frac{4\pi x_{scat}(t)}{\lambda}\right) \exp(i\omega t) dt, \quad (3.20)$$

In a spectrum of scattered light noise, scattered light in the linear regime would appear as a peak at the frequency of the motion of the scattering surface. Upconverted scattered light appears in spectra scattering shelves as illustrated in Figure 3.3. In a spectrogram, scattered light in the linear regime is simply a line at the frequency of motion. Upconverted scattered light appears in spectrogram as arches as shown in Figure 3.2. Figures 3.3 and 3.2 are both plotted from the same time series data. The four scattering shelves in Figure 3.3 correspond to the four arches in Figure 3.2.

Also plotted (as colored lines) in Figure 3.2 are the predicted *fringe frequencies*. To obtain this prediction, we use the following:

$$f_{\text{fringe},n}(t) = \left| \frac{2nv_{scat}(t)}{\lambda} \right|, \quad (3.21)$$

where n represents the number of bounces. In this equation, we are dividing the velocity of the scattering surface by half the wavelength. If the scattering surface moves by $\lambda/2$, then it has moved through the entire *fringe*. Dividing the velocity by $\lambda/2$ puts us in units of

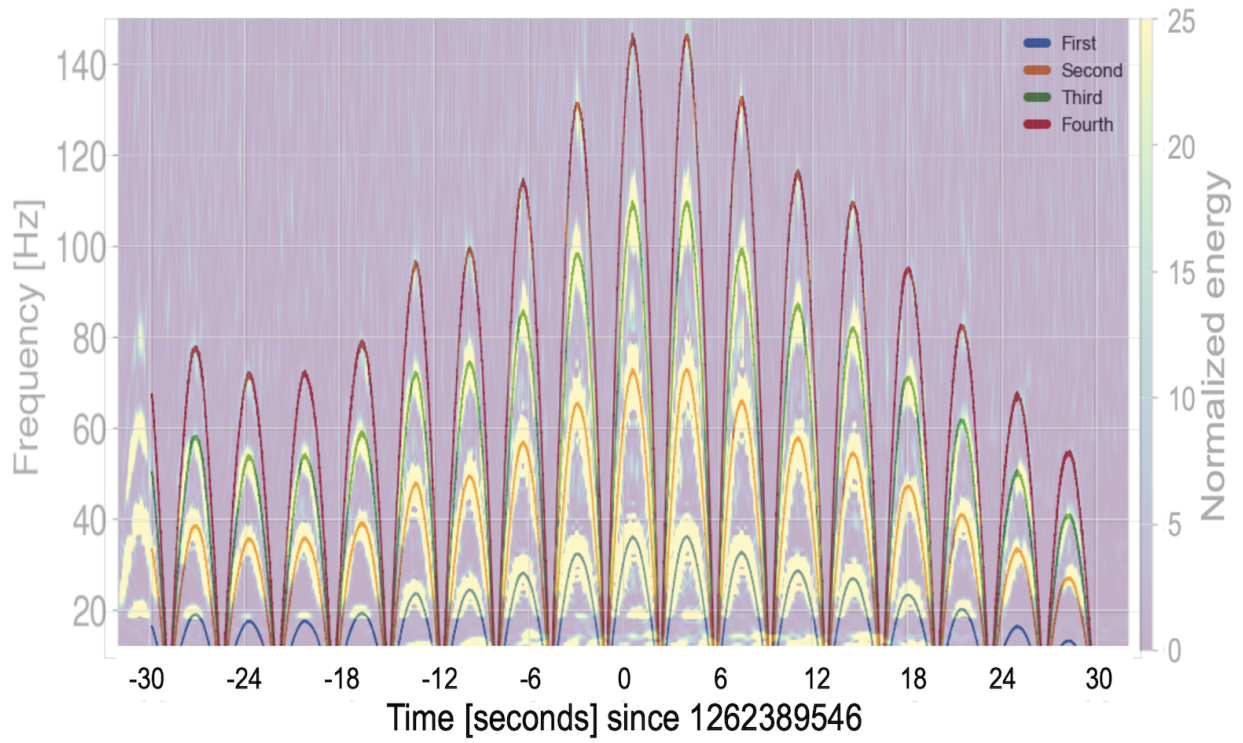


Figure 3.2. Spectrogram showing scattering arches. The fringe frequency for single and multiple bounce paths is calculated from scattering surface velocity and overlaid [48].

"fringes per second" and gives us the fringe frequency. In this example, the peak frequency of the arches is changing with time indicating that the peak velocity of the scattering surface is also changing with time.

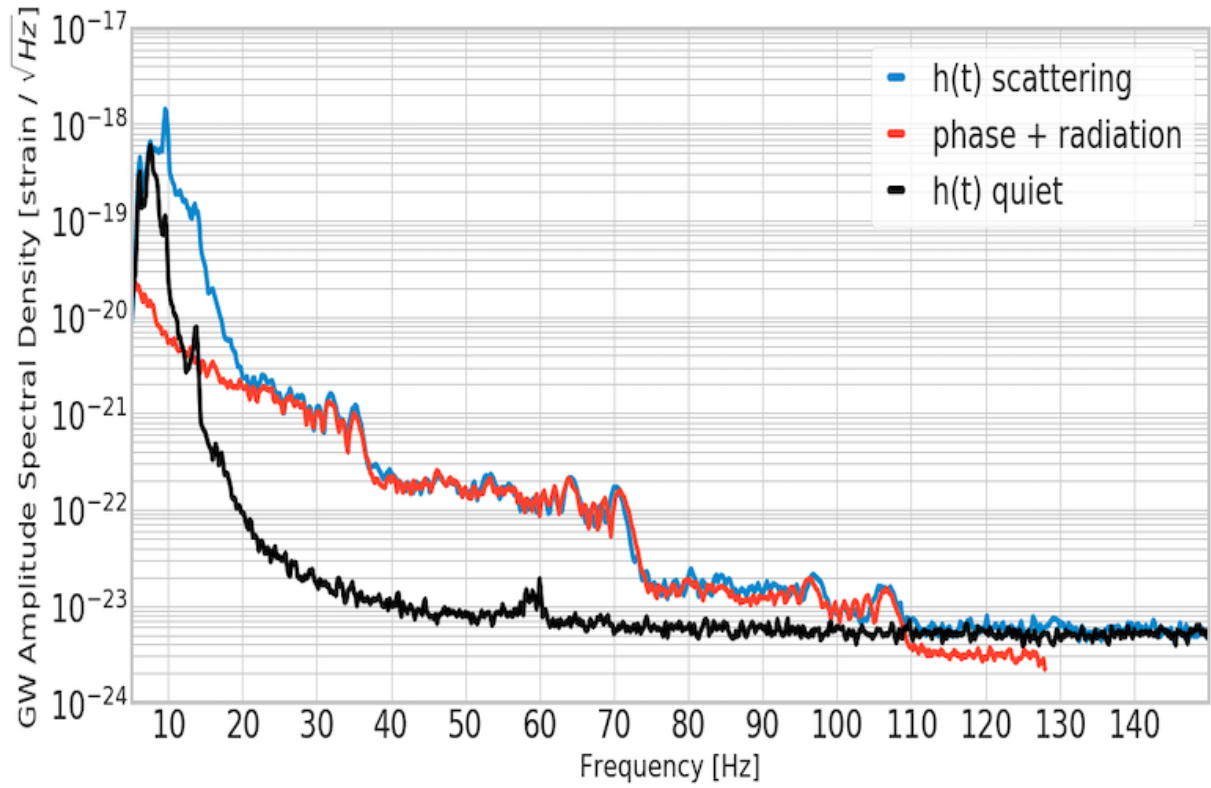


Figure 3.3. Spectra of measured scattering noise (" $h(t)$ scattering") plotted along with a model of the noise ("phase + radiation") and a quiet spectra (" $h(t)$ quiet") for reference [48]. The multiple scattering shelves seen here correspond to the multiple arches in Figure 3.2

CHAPTER 4. STRAY LIGHT (IMPROVED) CONTROL

As the second LIGO observing run (O2) was kicking off at the end of 2016, a project called Stray Light (Improved) Control (SLiC) was also getting its start. SLiC would be a project to design and install baffles in the LIGO interferometers in order to reduce the noise from scattered light. The baffles would be installed at the conclusion of O2. The main focus of SLiC was the recycling cavities, but baffles were also installed near the end test masses on the structures used to steer an auxiliary laser to and from the test masses. The project started with an initial set of baffles that were installed after the conclusion of O2. These baffles became known as SLiC Part A and subsequent improvements in the output arm of the interferometer became known as SLiC Part B. This chapter discusses the design, installation, and testing of both phases of SLiC.

4.1 SLiC Part A

Tests performed during O2 showed that the coupling of chamber motion to the gravitational wave channel via scattered light was highest near the output port of the interferometer [49]. Photos like Figure 4.1 taken with the interferometer in full lock showed that there were many reflective surfaces in close proximity to the optics in this area. This combination of testing and photographing was used to determine the priorities for SLiC.

From Figure 2.2 we can see that the output arm of the interferometer houses the signal-recycling cavity (SRC), the output Faraday isolator (OFI), the optical parametric oscillator (OPO), and the output mode cleaner (OMC). With multiple optics sharing optical tables, it would have been very difficult to isolate the source of the scattered light to a single mirror. The OMC was baffled with a shroud that completely enclosed the structure in 2015 [50]. The OFI lies in transmission of the signal recycling mirror (SRM), so it receives less power than the components in the SRC and was thus ranked with a lower priority than the mirrors of the SRC. The OPO was only installed after the conclusion of O2, so it could not have

been the source of the scattered light seen during O2. Because of these factors, the mirrors of the SRC were chosen as the location for the installation of new baffles following O2. And because the optics of the SRC share the same suspension structure design as the optics in the power-recycling cavity (PRC), the PRC would also receive new baffles. The mirrors of the PRC share optical tables with the mirrors of the input mode cleaner (IMC), so baffles were also designed for the input mode cleaner.

Another area that had shown previously high coupling was near the end test masses. One likely source for the coupling was the structure that holds the mirrors, which guide the photon calibrator (PCal) beam to and from the end test mass [51]. This structure spans the diameter of the beam tube, lies normal to the beam propagation direction, and is made of highly reflective aluminum. Its location had also been identified by vibration injections (where the motion of the vacuum system is driven by a mechanical device) as having higher coupling than the surrounding areas, so the PCal structure was also chosen as a location for baffling.

4.1.1 Design and Installation

There were numerous constraints that had to be considered when designing the SLiC baffles. The primary goal of the baffles was to reduce the amount of noise from scattered light. To accomplish this, they would need to reflect less light than the surfaces that they were covering. The new baffles would also need to move the same or less than the surfaces they were covering in order to reduce the noise. Beyond solving the problem of scattered light, the new baffles also needed to avoid creating noise in other ways. The SLiC baffles would need to be vacuum compatible and the apertures through which the main beam passes needed to be properly sized and aligned. Considerations for handling and installation also needed to be properly accounted for.

Structural

The suspension structures to which the SLiC baffles would be mounted are themselves mounted to the HAM-ISI tables which are seismically isolated. By mounting the baffles to the suspension structure, the baffles would also be seismically isolated. Vibrational modes of the baffle surface could lead to excess motion at anti-nodes, so passive damping was included in the design of the baffles. The passive damping was accomplished by sandwiching Viton o-rings between the suspension structure and the baffles at all of the attachment locations.

The baffles were designed to be mounted at an angle such that the specular reflections off of the baffles would be directed away from any optics. Where possible, the specular reflections were directed towards secondary baffles that offered additional attenuation via their low reflectance.

Coatings

In order to reduce the noise from scattered light, the new baffles would need to limit the amount of scattered light returning to the main beam. The baffles themselves would be made from polished stainless steel and then coated with a thin layer of material that would provide the required optical properties. Several coatings were evaluated by Alena Ananyeva at Caltech and ranked based on the following criteria: specular reflectance, BRDF, vacuum compatibility, ease of handling, and cost.

Specular reflectance and BRDF must be considered together to get the best coating. A highly polished mirror, for example, would have a very low BRDF, but the specular reflectance would be high. A rough surface, like the vacuum chamber walls, has a low specular reflectance, but the BRDF is high. If both specular reflectance and BRDF are low, then the coating is absorbing some of the power and the power that is reflected is contained to the specular direction. As mentioned in the previous section, the SLiC baffles were mounted at an angle with respect to the main beam, so the scattered power is directed away from the main beam. Also, where possible, the specular reflection is aimed at a secondary baffle.

When the evaluation was complete, two coatings were chosen: diamond-like carbon

Table 4.1. Optical properties of the coatings chosen for SLiC baffles. Diamond-like carbon (DLC) has the best optical properties, but is expensive and can only be applied to smaller parts, so black nickel was chosen as a backup option. These values were obtained at 57° angle of incidence.

	Stainless Steel	Black Nickel	DLC
BRDF (sr^{-1})	8×10^{-3}	1×10^{-3}	2×10^{-4}
R^2	2×10^{-2}	6×10^{-3}	5×10^{-5}

(DLC) and black nickel. Table 4.1 summarizes the optical properties of these two coatings along with uncoated stainless steel. DLC has better optical properties than black nickel, but it is more expensive and the size of parts that can have the coating applied is limited. Both materials were robust while handling and had similar outgassing properties when tested for vacuum compatibility.

Ray Tracing

Zemax is commercial ray tracing software that was used in the baffle design process. In Zemax, a 3-D model of the optical system being studied is created. From a source defined in the model, rays are launched. The source definition determines the distribution of emitted rays and everything from a point-like source emitting one ray in one direction to a 360° source emitting rays in all directions can be modeled. The source is also defined to have some power and that power is divided among the rays according to the source definition. The rays represent the straight line path that photons would take leaving the source. Each ray is propagated through the model until it encounters an object. Objects can reflect, absorb, or transmit any rays that land on them. Reflection can be defined to be specular only or it can include scattering. When a ray encounters an object, the properties of the object determine the path of the ray following the interaction with the object. If the object is absorbing, the path for the ray simply ends. If it reflects, scatters, or transmits, then the ray continues to propagate until encountering the next surface. A ray can also split when it encounters an object. For example, a ray encountering a 50/50 beamsplitter would split into two rays: one

continuing through the beamsplitter with half of the original power and one reflecting at 45° with half of the original power. A pre-defined, finite number of rays are launched from the source and their paths are traced through the model with the power in each ray also being tracked. The result of the ray tracing is displayed as the paths of the rays are drawn over the 3-D model of the optical system.

SolidWorks is computer-assisted design (CAD) program that has been used extensively in the design of the LIGO interferometers. The SolidWorks model of the LIGO interferometers includes the precise locations of the attachment points to which the baffles would be mounted, so the preliminary design for the baffles was made in SolidWorks. The Zemax model of the LIGO interferometer includes detailed models of the optics throughout the instrument, but only includes rough polygons for the other components. When detailed analysis is required, the 3-D SolidWorks model for a part can be imported into the Zemax model. The SLiC baffles were first modeled in SolidWorks to align them to the suspension structures. They were then exported to Zemax where the optical alignment could take place. The first part of the alignment was to locate the apertures in the baffles and to ensure that each aperture had the proper clearance. The second part of the alignment made sure that ghost beams that were meant to be dumped on the baffles actually landed on the baffles as intended.

Installation

O2 ended on August 25, 2017 and installation of the SLiC baffles began the following week. The baffles were manufactured, coated, and shipped from Caltech. Prior to the end of O2, the baffles were received at the observatories and inspected for any potential damage. Special care had to be taken when handling the baffles throughout the installation process. Bare hands were never allowed to touch the baffles as the oils would have been a vacuum contaminant and could have damaged the coatings. The baffles were sprayed with ionized nitrogen prior to installation in the chamber to remove any loose dust particles and to discharge any static electricity that had accumulated in the coating.

At LIGO Livingston, the baffles were installed in phases. The first set of baffles were installed in HAM2 and HAM5 in August and September of 2017. HAM2 and HAM5 are symmetric vacuum chambers in the power- and signal-recycling cavities, respectively. HAM2 houses two of the three mirrors that make up the power-recycling cavity and two of the three mirrors that make up the input mode cleaner. HAM5 houses two of the three mirrors that make up the signal-recycling cavity and also the output Faraday isolator. The next set of baffles were installed in HAM3 and HAM4 in November and December of 2017. HAM3 houses one mirror each from the power-recycling cavity and the input mode cleaner and HAM4 houses one of the three mirrors in the signal-recycling cavity. The final phase of installation took place in April of 2018. The PCal baffles were installed in conjunction with the ETMs being replaced for optics with improved coatings.

Figure 4.2 is a photo taken just after the installation of the baffles in HAM5. The hardware used to attach the baffles allowed for rough and fine adjustments. The final location of the baffles was determined using the main laser of the interferometer. The beam was aligned as it would be for full interferometer operation, but the input power was turned down and the arm cavities were misaligned to prevent any power build-up in the arms. The baffles were adjusted so that the beam was centered in the aperture.

4.1.2 Measuring Performance

Quantifying any improvements made by the SLiC baffles is a difficult task. The main reason for this is that scattered light noise is sub-dominant most of the time, so it lies below the noise floor of the interferometer. In order to measure scattered light noise, the level of noise must be artificially increased. We cannot readily modulate the amount of power in any given scattered light path, but we can increase the motion of many surfaces throughout the interferometer. We increase the motion (as seen by a witness sensor) by performing an *injection* and measuring the interferometer response. To quantify any improvements, we perform the same injection (by matching the response in the witness sensor) before and after

the baffles are installed and then compare the results. We compare the results by calculating *coupling functions*. A coupling function is a transfer function that allows us to convert a measurement of motion (displacement, velocity, or acceleration) into equivalent strain noise.

Shaker Injections

To make the injections needed for coupling functions, we use *shakers*. These shakers have a reciprocating mass and a drive system to move the mass. The drive system is either piezoelectric or electromagnetic. In either case, a time-varying signal is sent to the shaker causing it to vibrate. The injection signal is defined using digital filters and then sent through a digital-to-analog converter (DAC) to the shaker. The most common signal used is a line at a single frequency, but broadband injections over a range of frequencies and sweep injections that slowly change in frequency over time are also used. The range of frequencies being tested depends on the shaker being used, but can range from a few Hz up to a few hundred Hz.

The piezoelectric shakers are made by PiezoSystems, Inc and are small enough to be attached directly to the vacuum chamber with a clamp. The electromagnetic shaker, an APS 113 Electro-Seis, causes interference between the electric fields used to drive the mass and the sensors on the vacuum chamber, so a connecting rod is used. Figure 4.3 is a photograph showing how the low frequency shaker is connected to the vacuum chamber.

The piezoelectric shakers are smaller and more portable, but their applied force is limited below 40 Hz. For lower frequency injections, the electromagnetic, or *low-frequency*, shaker is used. The low-frequency shaker is capable of driving motion at frequencies below 1 Hz, but the motion does not propagate well from the shaker through the connecting rod and to the vacuum chamber, so 1 Hz is generally the lower limit of the frequencies tested with shakers. The low-frequency shaker is capable of driving excitations up to approximately 200 Hz and the piezoelectric shakers can drive excitations into the kHz regime, but generally shaker injections are only performed up to around 100 Hz. Above that frequency, large speakers

are used to make acoustic injections as they can cover a larger area and a larger range of frequencies in a shorter period of time. The low-frequency shaker is also capable of driving broadband injections. The broadband injections (both acoustic and shaker) are helpful in identifying mechanical resonances. Mechanical resonances are important for scattered light as the nodes see increased motion at their resonant frequencies relative to surrounding surfaces.

The amplitude of single frequency line injections are tuned such that the witness sensor (usually an accelerometer) sees at least a factor of 10 more motion than during ambient times. Figure 4.4 shows the gravitational wave channel (DARM) and the accelerometer response to line injections made near the output port of the interferometer. We see in Figure 4.4 that when compared to the accelerometer, the DARM response to line injections is broader (spread over a wider range of frequencies) and the peak amplitude is reduced relative to ambient. This widening of peaks is due to fringe wrapping. The shaker injections drive the vacuum system at the prescribed frequency, but ground motion is also always present during the injections. The low frequency ground motion adds sidebands to the signal at the driven frequency. The level of ground motion at the time of the test determines the extent to which the peak is broadened.

Coupling Functions

When performing a set of follow-up injections, we attempt to tune the injection to match the accelerometer response of the previous injections as best as possible, but it is never possible to exactly replicate an injection. We therefore need to calculate a *coupling function* that relates the interferometer response to the accelerometer response:

$$F_{coup}(f) = \frac{\sqrt{h_{\text{inject}}(f)^2 - h_{\text{quiet}}(f)^2}}{\sqrt{X_{\text{inject}}(f)^2 - X_{\text{quiet}}(f)^2}}, \quad (4.1)$$

where $h_{\text{inject}}(f)$ and $h_{\text{quiet}}(f)$ are the amplitude spectral densities (ASDs) of the gravitational wave channel during the injection and during a period of no injections respectively. Similarly, $X_{\text{inject}}(f)$ and $X_{\text{quiet}}(f)$ are the ASDs of the witness sensors during injection and quiet periods respectively. We can see that if we managed to get two identical injections as seen by the witness sensor, but the DARM response was less in one, then the overall value of the coupling function would be lower and we would say that the coupling has been reduced.

We can also use a coupling function to make a projection of the equivalent strain noise. This is especially useful in the case of scattered light where the noise lies below the noise floor of the interferometer. We can project the noise and have an estimate of how far below the noise floor a particular source may lie. To obtain the projection, we multiply the coupling function by the ambient accelerometer spectrum to get a projection to DARM:

$$h_{\text{projection}}(f) = F_{\text{coup}}(f) \cdot X_{\text{quiet}}(f) \quad (4.2)$$

Coupling functions are a tool that can help with comparing different injections, but, in the case of scattered light, they are not a perfect tool. As we have seen, the interferometer response to injections depends not only on the injection, but also the ambient motion of the interferometer. As the low-frequency ground motion increases, the peak seen in DARM at the injection frequency is lowered in amplitude and spread out across a wider range of frequencies. To compensate for this, we often use the root mean square (RMS) of the difference $h_{\text{inject}}(f) - h_{\text{quiet}}$ across a small band of frequencies around the injection frequency.

4.1.3 Results

Following the installation of the baffles in HAM2 and HAM5, we performed a series of shaker injections to compare with measurements taken during O2 prior to installing any baffles. Figure 4.5 plots the two sets of coupling functions together and we can see that

the results are mostly inconclusive. There is a slight reduction in coupling at a few of the frequencies tested, but most are within a factor of two of the original tests. Because of the uncertainties involved in calculating the coupling functions, we cannot conclusively say that the slight improvement comes from installing the SLiC baffles.

Another set of injections were performed in February 2018 after the HAM3 and HAM4 baffles were installed and the results were similarly inconclusive. At the time of the injections, there was a small vacuum leak in HAM6 which necessitated running an auxiliary vacuum pump that caused excess noise from 45 – 52 Hz. Also, at the time the injections were performed, the interferometer was undergoing almost daily configuration changes with the squeezer subsystem being brought online and the input power being increased. A couple of attempts were made to repeat the injections, but the results were never conclusive.

4.1.4 PCal Periscope Baffles

Figure 4.6 is a photo that shows the PCal periscope before and after installing the SLiC baffles. For the PCal periscope, we did not have a reference set of measurements against which we could compare, so we took a full set of reference measurements. We noticed during these tests that the coupling at the Y-end was higher than the coupling at the X-end and it seemed to be the worst in the immediate vicinity of the PCal periscope.

As Figure 4.6 shows, the baffle installed on the PCal periscope only partially covers the structure. The decision to only partially cover the structure was made because the test mass is offset with respect to the center of the beamtube (and thus the PCal structure). Cost and manufacturing time were also contributing factors. A month long break from the observing run was planned for October 2019 to allow both LIGO observatories to make incursions into the vacuum system. At LIGO Livingston this opportunity was used to install the additional PCal baffle panels as well as a set of newly designed *nozzle baffles* that were meant to limit the amount of light reaching the 6 glass viewports located behind the PCal periscope. All of these additional baffles were installed at both end stations at LIGO Livingston. Four of

these viewports are used to allow the PCal and optical lever (OPlev) lasers to enter and exit the vacuum system. The OPlev laser is used to aid in interferometer alignment. One of the other two viewports has a camera mounted on it that provides an image of the test mass and the sixth is left unobstructed. While installing the nozzle baffles, we felt that when installed as intended, the nozzle baffles for the OPlev viewports left too little clearance for the beam to pass through. Those baffles were instead fastened to the panels on the PCal periscope baffles. Figure 4.7 shows the completed PCal periscope baffling as well as the OPlev nozzle baffles which are located just to the left and to the right of the 6 o'clock position.

We repeated the shaker injections that showed high coupling and found that the coupling had been reduced after installing the additional baffles. Figure 4.8 is a plot showing the interferometer (top) and accelerometer (bottom) response to the initial (red) and follow-up (blue) injections. We can see that the interferometer response to the injections is greatly decreased following the installation of the additional baffles.

4.2 SLiC Part B

The installation of the SLiC baffles did not significantly reduce the coupling between scattered light in the output arm and the gravitational wave channel, so the investigations into possible sources continued. The shaker tests had isolated the source to HAM5 or HAM6, but the two chambers are adjacent, so any injection in one chamber caused increased motion in the other chamber, making it impossible to distinguish between the two chamber with shaker injections. Using a camera that was sensitive to infrared light, we began to take photographs during interferometer operation to try and isolate the source. A photo (Figure 4.9) taken by Robert Schofield showed that the output Faraday isolator (OFI) was scattering a significant amount of light. Based on these photographs and the shaker injections pointing to the general area, we began designing a shroud to encapsulate the OFI.

4.2.1 Design and Installation

The OFI is made up of several optical components on a small optical table. The optical table is suspended from a structure that sits on the large optical table in HAM5. Figure 4.10 is a photo showing the OFI bench. The OFI would be encapsulated by a shroud comprised of coated stainless steel panels that are mounted to the support structure. The panels would completely encapsulate the OFI so that any light scattering from the optics on the bench could not reach the chamber walls. Some amount of light would scatter from the panels, but because the panels are mounted on the HAM optical table, they move less relative to the optics than do the surrounding chamber walls. The shroud panels would be coated with black nickel so that some of the scattered power would be absorbed by the coating. The result is that the scattered light would see less motion and the power would be reduced, thus reducing the amount of noise.

The design process for the OFI shroud mirrored that for the SLiC Part A baffles. The shroud was first designed in SolidWorks and then exported to Zemax where the apertures were placed and ghost beams were examined. During this review, we noticed that one of the ghost beams coming from the OFI had never been properly accounted for.

The thin-film polarizer (TFP) rotates the polarization of any light that is back-reflected from components downstream of the OFI so that the light is rejected by the Faraday isolator and not able to re-enter the interferometer. The TFP is also the component that is used to send squeezed light into the interferometer. Most of the light coming from the interferometer passes through the TFP and goes on to the OMC, but a small amount of light is reflected from the anti-reflective coating on the rear of the TFP. Figure 4.11 shows the ghost beam from the thin-film polarizer (TFP) landing on the mirror mount for one of the steering mirrors in the squeezed light path. When the TFP ghost beam was found in Zemax, the team at LIGO Hanford used an infrared sensitive camera to look through a viewport to determine if the ghost beam was landing on the mirror mount as predicted. Figure 4.12 is the photo that was taken by the team at LIGO Hanford confirming the location of the TFP ghost beam.

The TFP is wedged such that the back of the optic is angled with respect to the front. This means that the ghost beam and main beam will not co-propagate and will achieve separation after some distance. At the location of the shroud, the two beams (ghost and main) are still essentially overlapping, so the new shroud could not be used to dump the TFP ghost beam. Instead, a small beam dump would be added to the optical table in HAM5 to dump the ghost beam.

The OFI shroud and TFP beam dump were installed in HAM5 in July and August of 2018. The OFI shroud has 2 apertures for the main beam and one aperture for the squeezed light beam that had to be aligned with the respective lasers. Figure 4.13 shows the shroud after it was installed. The TFP ghost beam was located using IR cards and viewers and the beam dump was placed between the OFI and the squeezed light steering mirror in the path of the ghost beam.

4.2.2 Results

A follow-up set of injections (solid lines) were performed in October 2018 and those injections are shown in Figure 4.14 alongside the injections from November 2017 (dashed lines). We compared the injections to the set performed in November 2017 instead of the more recent injections performed in February 2018 because of the excess noise in DARM in February due to the auxiliary vacuum pump. The accelerometer saw a very similar response for most of the injections, but the 75 Hz injection did not register as well in the follow-up injection. For all of the injections, the DARM response is narrower indicating that the ground motion was lower for the follow-up injections. Below 45 Hz, we see a significant reduction in the interferometer response. Above 45 Hz, it is less clear, though the area under the curve is smaller for the follow-up injections.

Figure 4.15 shows the coupling functions in the top panel and the ambient projection to DARM in the bottom panel. The coupling functions show reduced coupling below 60 Hz and similar levels of coupling from 60 to 70 Hz. Above 70 Hz, the coupling appears to

have increased, but the projection lies above the measured noise suggesting an issue with the calculation. As mentioned in the previous paragraph, the accelerometer response was lower for the follow-up 75 Hz injection than for the initial injection and the interferometer response was similar but it also included increased noise at 74 Hz that was present even when not injecting. Ideally, the 75 Hz injection would have been repeated to try and clarify the situation, but limited time prevented another test.

SLiC Parts A & B managed to reduce the coupling of scattered light to the gravitational wave channel in the critical 30 to 70 Hz frequency band. SLiC focused on reducing the amount of scattered power returning to the main beam. It did this with improved coatings and geometries that directed the power away from the path of the main beam. The overall impact on instrument sensitivity was not profound since the ambient noise lies below the noise floor of the interferometer, but because all of the various noise sources add together in quadrature, even an improvement in a sub-dominant noise source offers some improvement to overall sensitivity.



Figure 4.1. Photo taken in full lock of optics in HAM5. Glints can be seen on the suspension structure, ballast masses on the table, and earthquake stops.

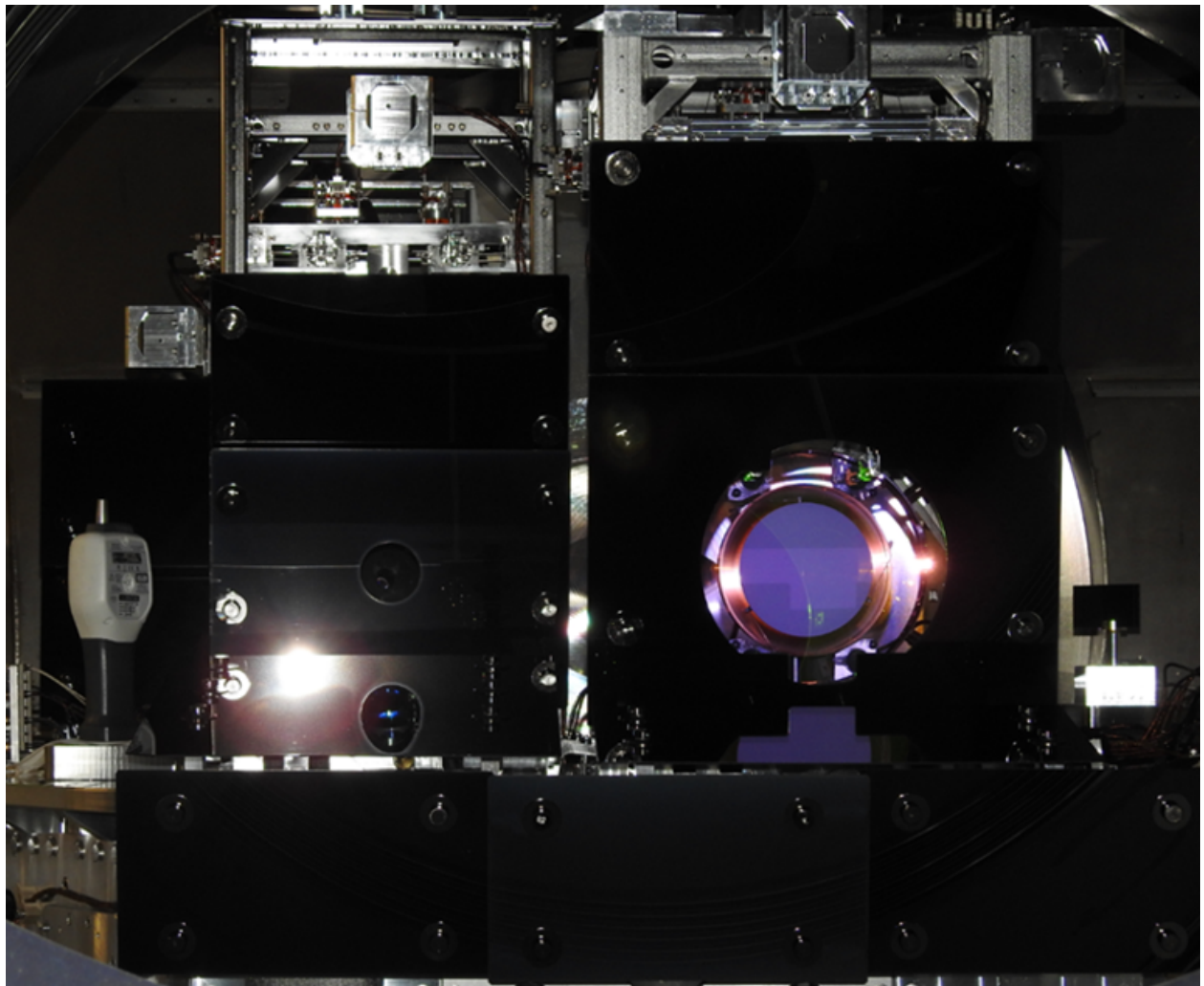


Figure 4.2. Photo taken just after installing the new baffles in HAM5. Suspension structure, ballast masses, and earthquake stops are all covered by the new baffles.

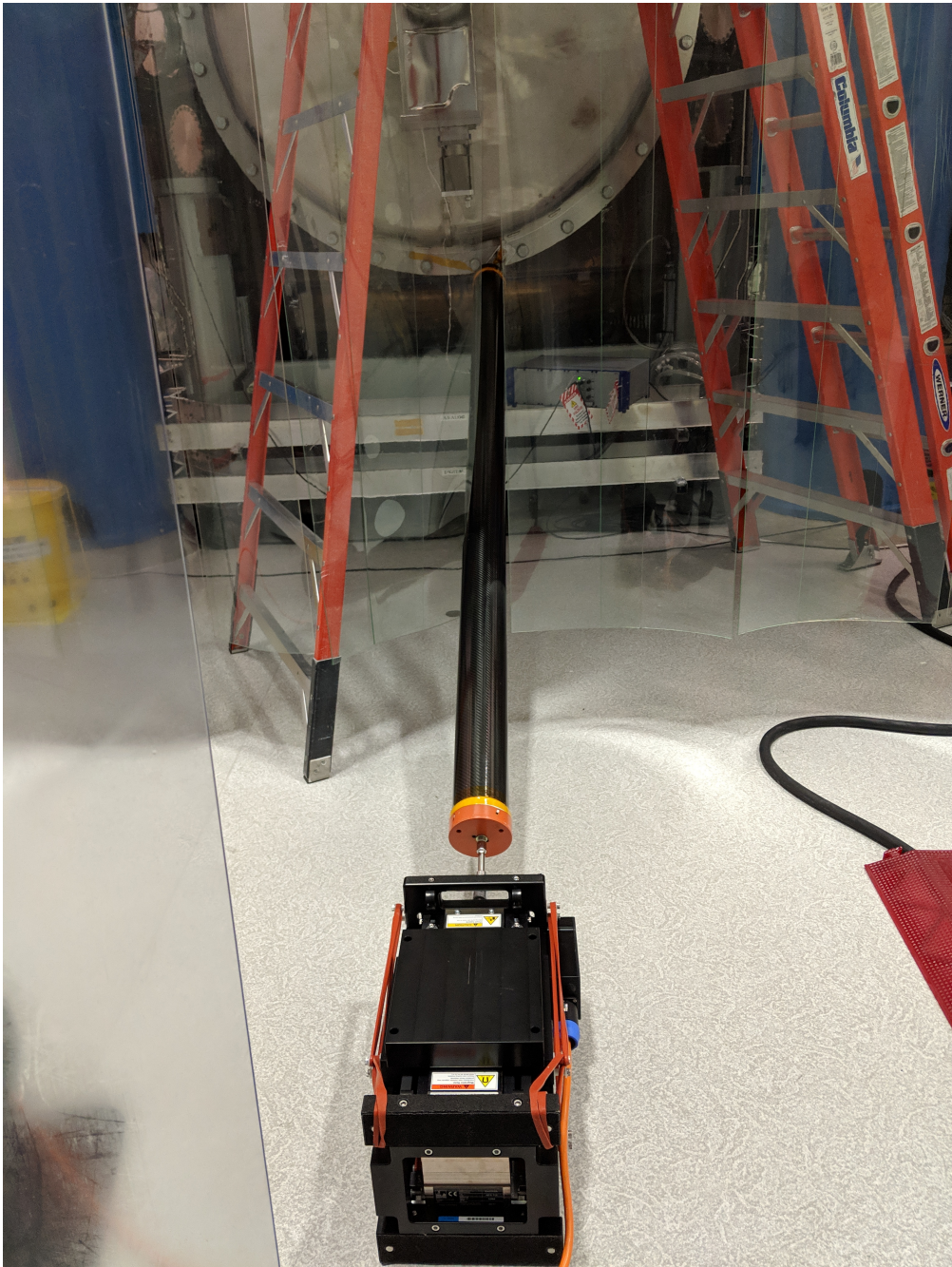


Figure 4.3. The broadband shaker sits on the floor next to the vacuum system and is connected to the vacuum system via a carbon fiber tube.

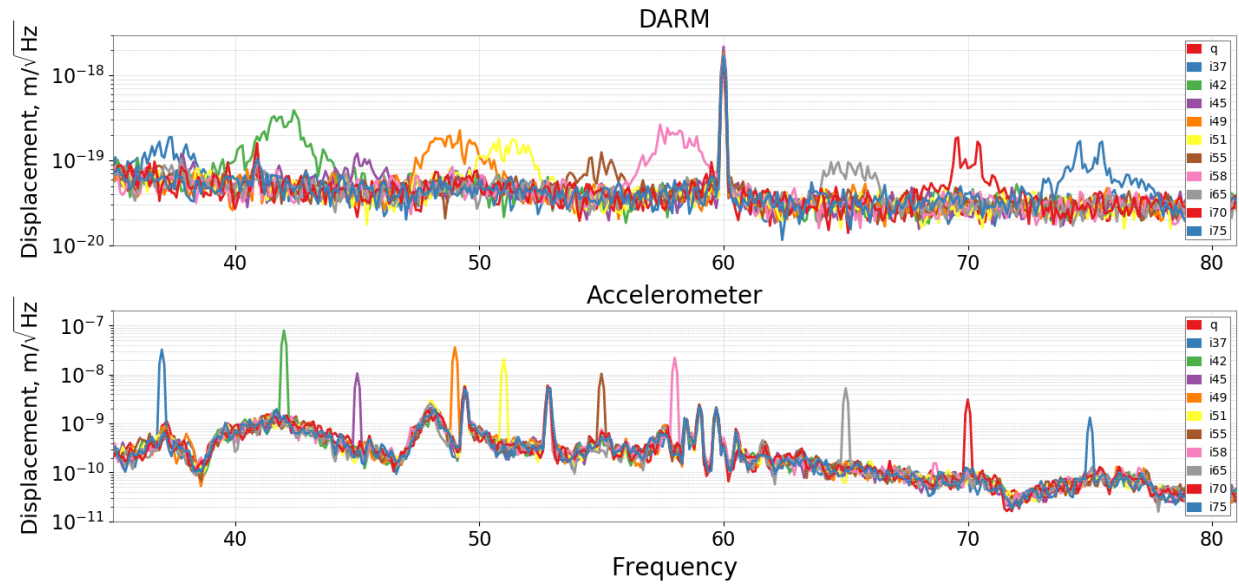


Figure 4.4. Shaker line injections made after installing baffles. The top plot shows the DARM response to the injections while the bottom plot shows the accelerometer response.

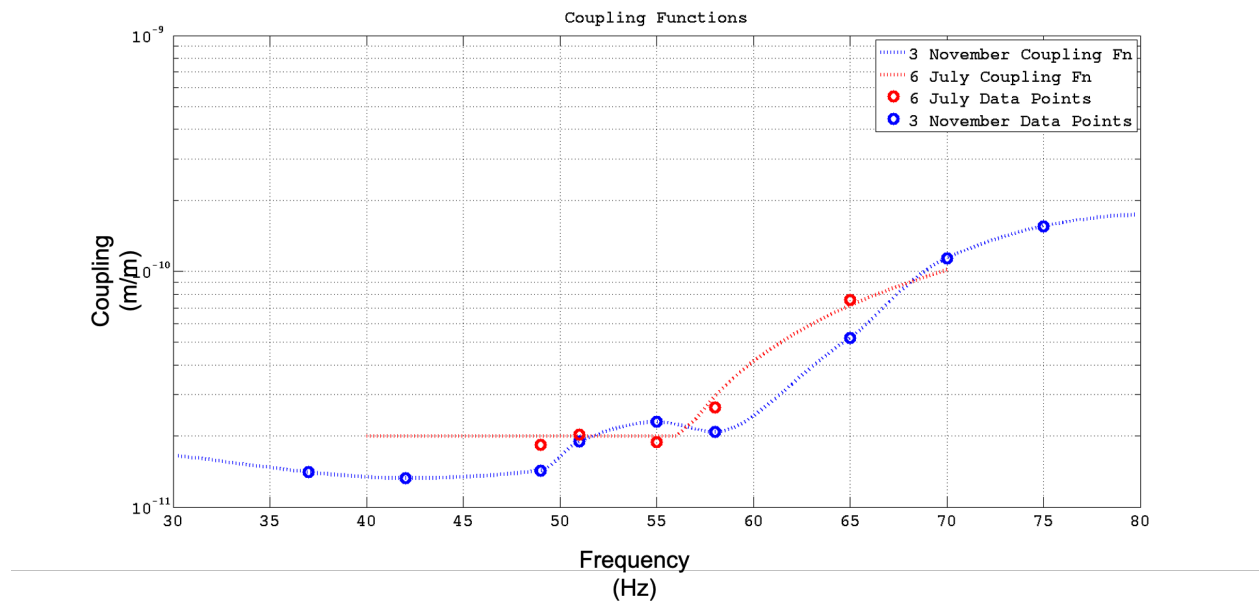


Figure 4.5. Coupling functions calculated before (red) and after (blue) installing SLiC baffles. Tests were performed near HAM5/6 in the output arm of LIGO Livingston.



Figure 4.6. Photo showing the PCal periscope before (left) and after (right) installing SLiC baffles.



Figure 4.7. Photo showing the completed installation of the additional PCal periscope panels which provide full coverage. The OPlev nozzle baffles are also visible just to the left and to the right of the 6 o'clock position.

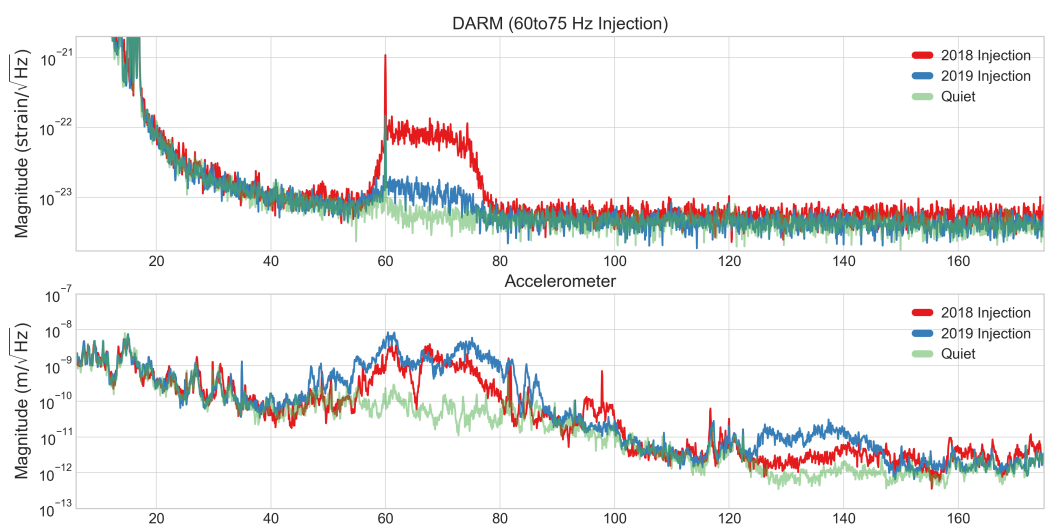


Figure 4.8. Interferometer response to a 60-75 Hz broadband vibration injection performed at the Y-end of LIGO Livingston. The plot compares identical injections made before and after installing baffles during the October vent.



Figure 4.9. Photo showing diffuse scatter off of the OFI bench.

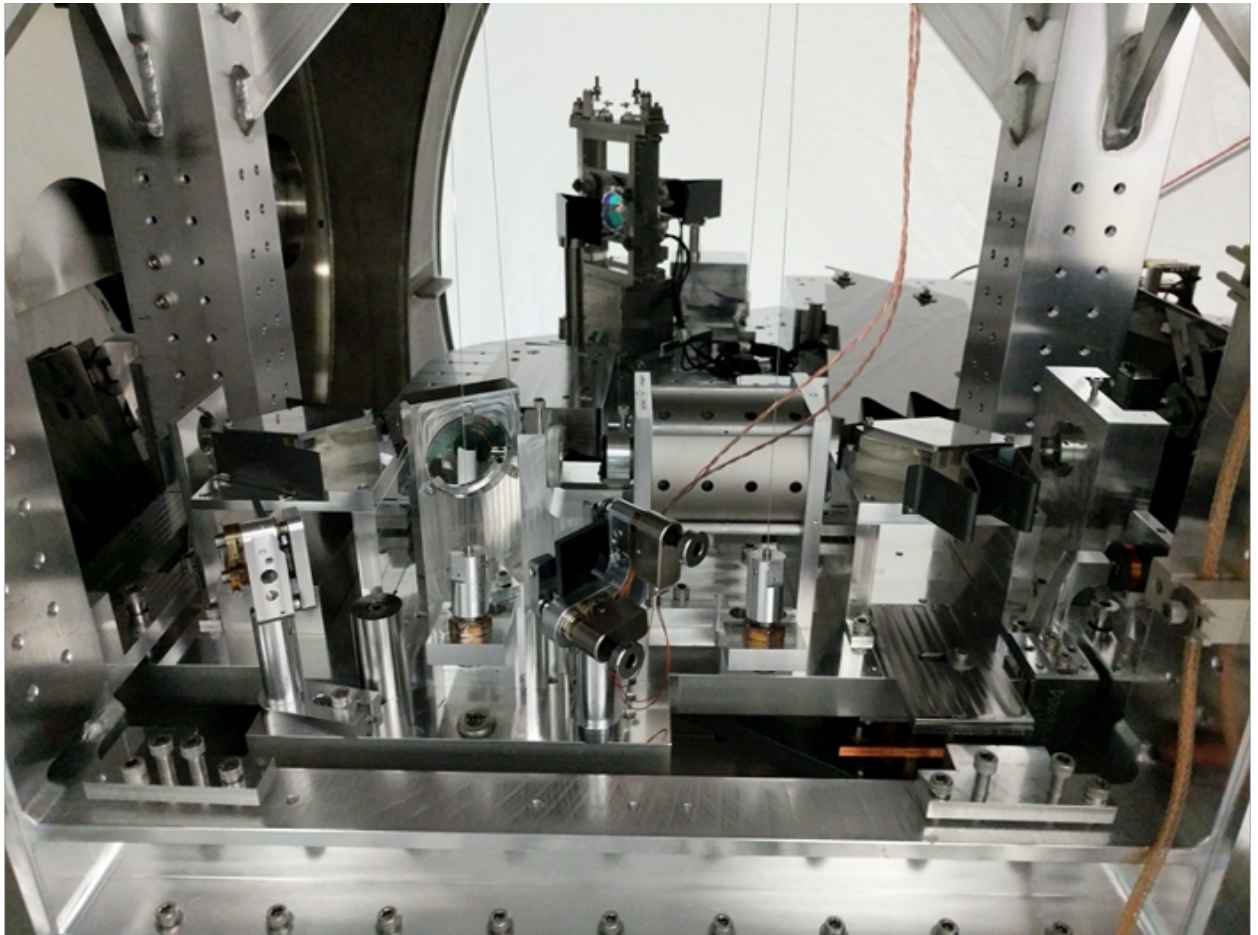


Figure 4.10. Photo showing the components on the OFI bench with the HAM5 door removed.

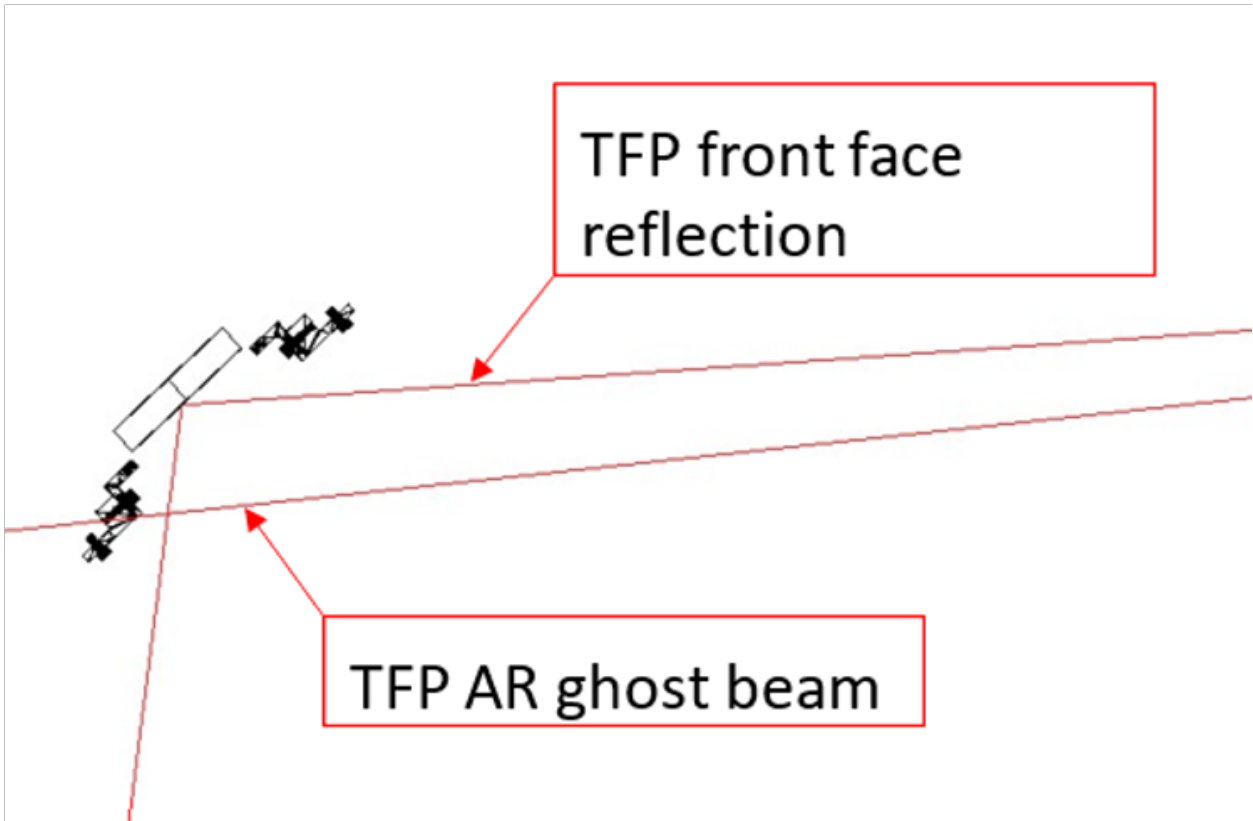


Figure 4.11. Ray tracing the path of the TFP-AR ghost beam showed the ghost beam landing on the mount for one of the steering mirrors in the squeezed light path.

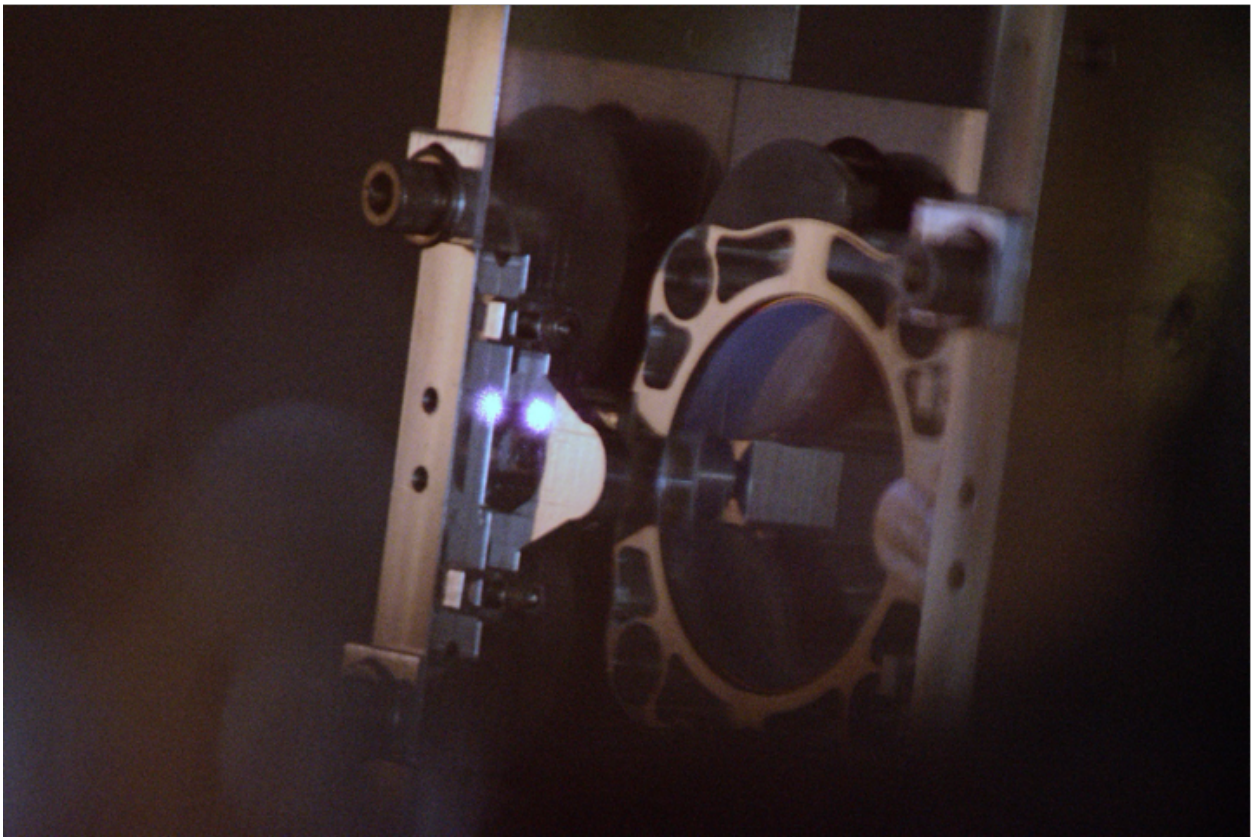


Figure 4.12. Photo taken with an infrared sensitive camera showing the thin-film polarizer (TFP) ghost beam landing on the mount for one of the steering mirrors in the squeezed light path.

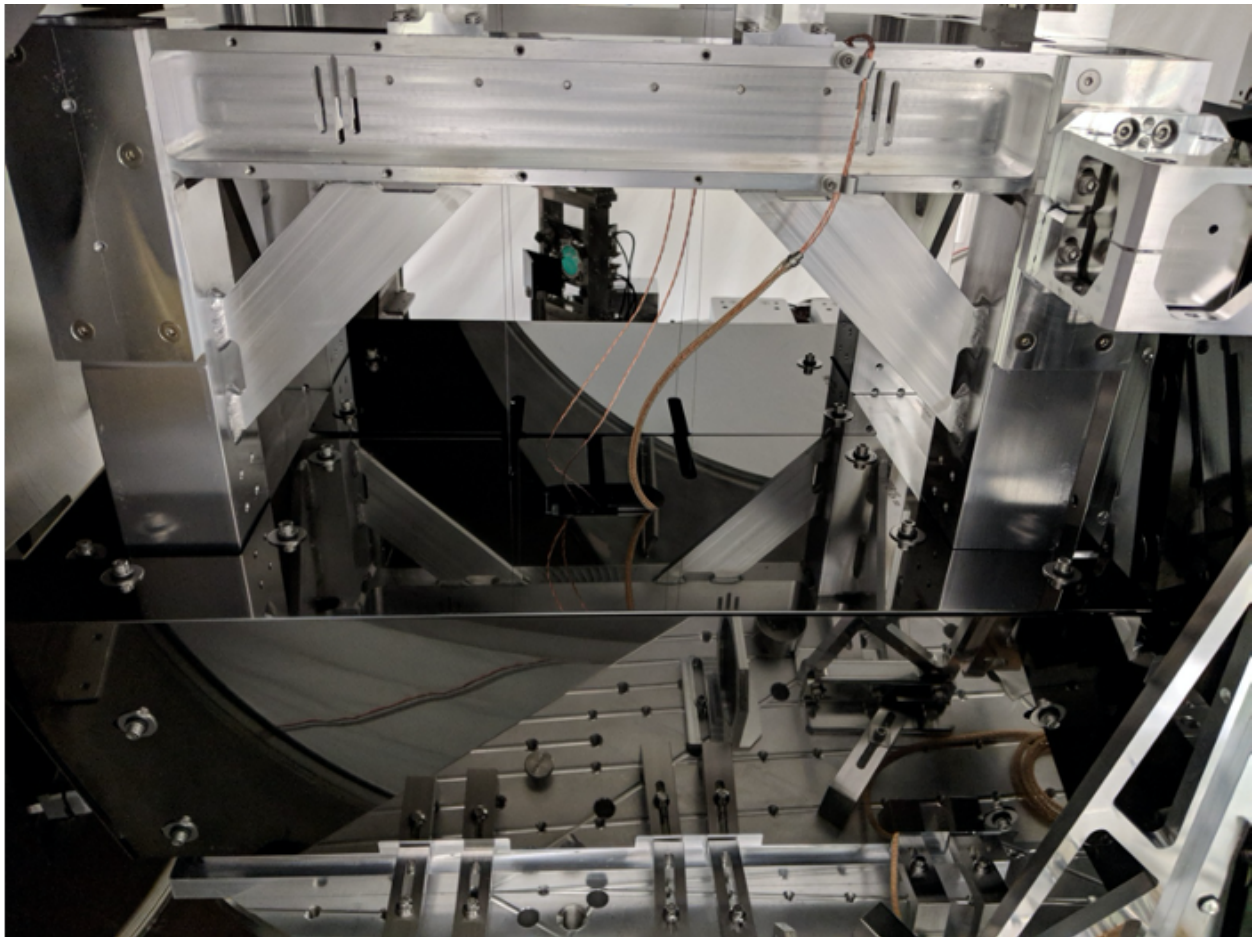


Figure 4.13. Photo taken after the OFI shroud was installed.

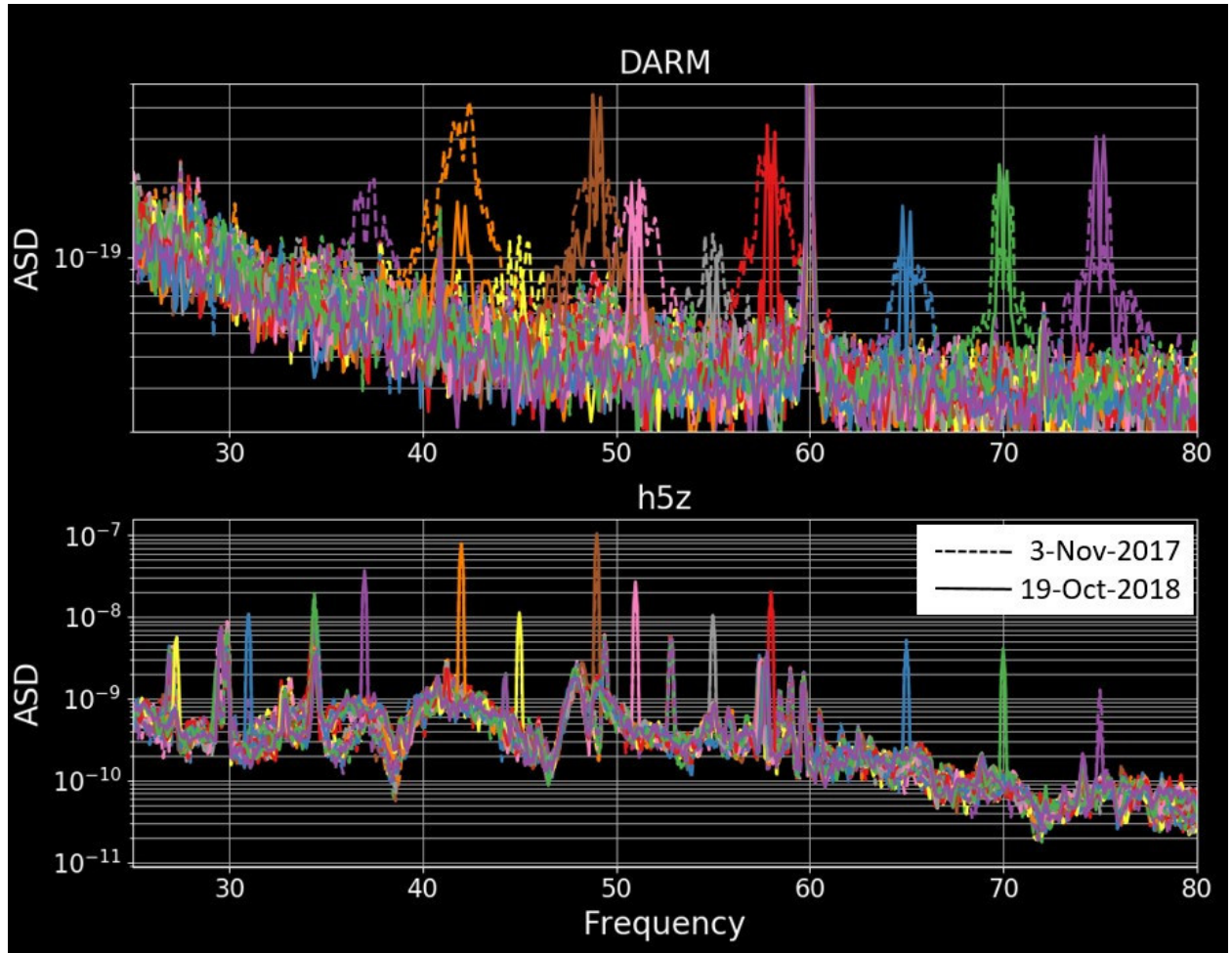


Figure 4.14. Comparison of injections performed before (dashed lines) and after (solid lines) installing the OFI shroud and TFP beam dump. The accelerometer response (bottom panel) was nearly identical for most of the injections and we can see that the interferometer response (top panel) was much less below 45 Hz and above 45 Hz the peak heights are similar, but narrower. This suggests that the ground motion was elevated for the pre-install injections.

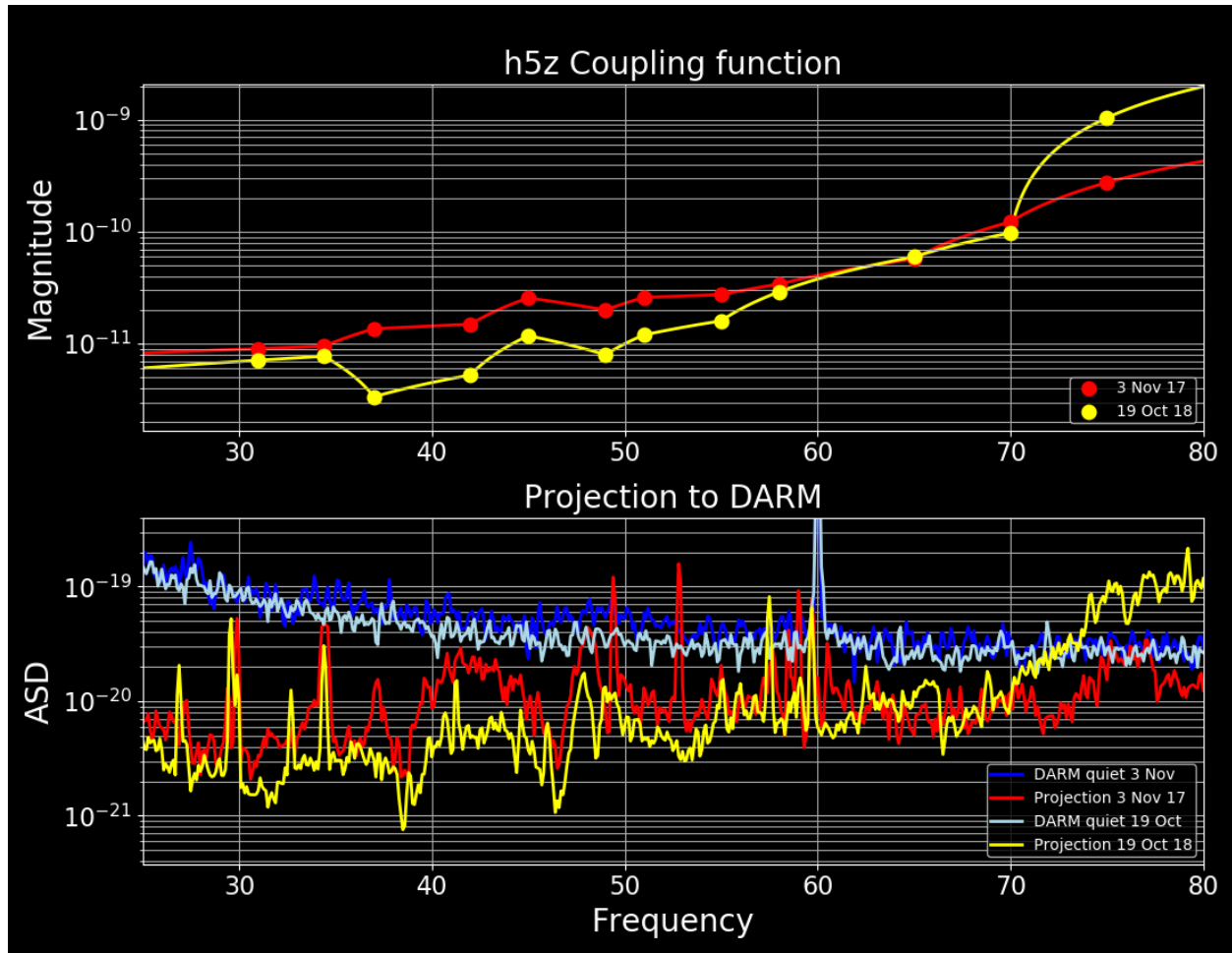


Figure 4.15. Coupling function (top panel) and ambient projection (bottom panel) calculated before (red) and after (yellow) the OFI shroud install. Coupling is reduced from 30-60 Hz and remains similar from 60-70 Hz. Above 70 Hz, coupling appears to have increased, but a decreased accelerometer response to the 75 Hz injection and spurious noise at 74 Hz may have skewed that result.

CHAPTER 5. SCATTERED LIGHT NOISE FROM INCREASED GROUND MOTION

In this chapter we examine scattered light noise in the gravitational wave channel that correlates with increased ground motion. As we began preparing the interferometer for the third observing run, we began noticing scattering shelves in the gravitational wave channel. These shelves are indicative of low-frequency motion being upconverted to higher frequencies. In addition to the scattering shelves, we were consistently seeing decreased range during daylight hours. We, at first anecdotally and later more rigorously, noticed that the appearance of these scattering shelves and range drops were correlated with increased ground motion as witnessed by the ground seismometers. Over time, we identified three different morphologies for the scattering noise and worked to identify the mechanism for each. As of this writing, two of the scattering types have been mitigated. A likely mechanism for the third type of scattering has been identified and a mitigation strategy is currently being developed and implemented. The work in this chapter represents a highly collaborative effort between the on-site commissioners and members of the detector characterization team including significant contributions from the LSU detector characterization group.

5.1 End Station Layout

Each of the noise sources discussed in this chapter originates near the end test masses (ETMs) of the LIGO interferometers, so we begin our discussion with a review of the detector components in the vicinity of the test masses. Figure 5.1 is a SolidWorks rendering that shows the location of several key components.

The test mass is housed inside the basic symmetric chamber (BSC) that was described in Chapter 2. Connected to the BSC is a cylindrical vacuum chamber called a *manifold*. This manifold houses the PCal periscope that was described in Chapter 4 as well as the *cryo baffle*. The cryo baffle was designed to catch wide-angle scatter from the ETM and narrow-

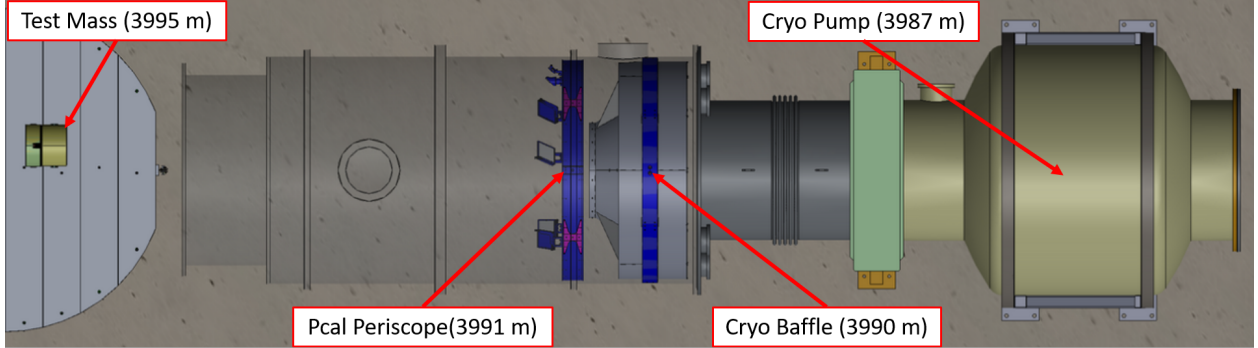


Figure 5.1. SolidWorks rendering showing the locations of the ETM, PCal periscope, cryo baffle, and cryo pump [52]. Distances shown are measured from the beamsplitter.

angle scatter from the ITM along the same arm. The cryo baffle gets its name because it was meant to shield the *cryo pump* from scattered light. The cryo pump is a cryogenic vacuum pump that greatly aids in removing any residual water vapor that may be trapped inside the vacuum system.

In addition to housing the test mass, the end-station BSC also houses the reaction mass and the transmission monitoring system (TMS) as seen in a schematic representation in Figure 5.2. The reaction mass, like the test mass, is suspended from a quadruple-stage suspension. Both *chains* are surrounded by a structure called a *cage* that is directly mounted to the ISI optical table which serves as a displacement reference and also provides protection for the chains. Near the top stage of each chain, a set of OSEMs measure the position of the chain relative to the cage and can also be used to actuate on the chain. On the upper intermediate (UIM) and penultimate (PUM) stages, the OSEMs are mounted on the reaction masses, so these sensors measure the relative position of the two chains. At the bottom stage, a series of 5 gold traces make up the electro-static drive (ESD) that is used to apply corrective forces between the reaction mass and the test mass [48].

The TMS consists of a beam-reducing telescope and an optical table with quadrant photodiodes (QPDs) that measure the position and intensity of the beam transmitted through the ETM. The TMS is also serves to send the 532 nm auxiliary laser used for initial align-

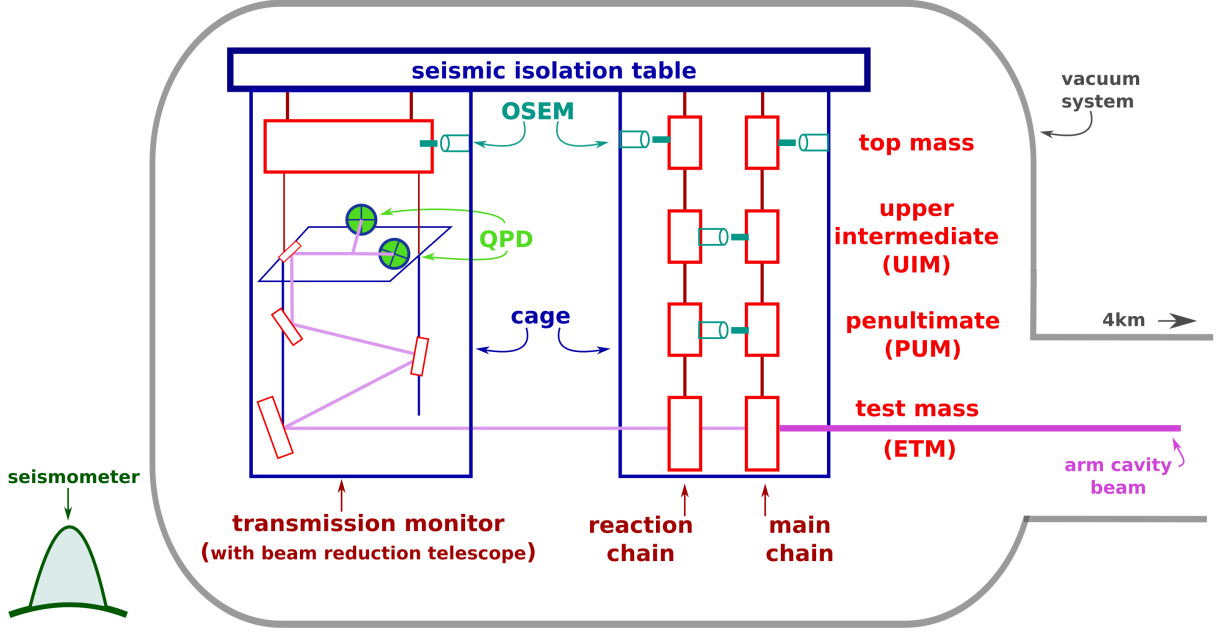


Figure 5.2. Schematic diagram of the sensors and actuators used to control the position of the end test mass [48]

ment of the arm cavities into the arm cavity. The telescope and optical table are housed on a rigid structure that hangs at the bottom of a double stage suspension. The TMS is surrounded by a cage which includes OSEMs to measure the position of the top stage and actuate as needed [48].

5.2 Ground Motion

Ground seismometers placed outside the vacuum system, but near the test masses, measure the ground velocity. We divide the ground motion spectrum into frequency bands whose motions are dictated by different environmental sources. The *earthquake band* ranges from 0.03 – 0.1Hz and the motion in this band, as the name suggests, comes from earthquakes and also from wind gusts. The *micro-seismic band* ranges from 0.1 – 1Hz but is usually subdivided into the 0.1 – 0.3Hz band and the 0.3 – 1Hz band. Motion in this band is primarily driven by ocean waves pressing down on the solid earth below. The motion is dominated by a peak that can change frequency, but is generally between 0.15 – 0.2Hz. At LIGO Livingston,

this band is often at the level of $1\mu\text{m}/\text{s}$ or higher, which is large enough for fringe wrapping to occur. The final band is the *anthropogenic band* which ranges from $1 - 10\text{Hz}$ and it is also sub-divided into $1 - 3\text{Hz}$ and $3 - 10\text{Hz}$ bands. This motion is generally attributed to human activity such as trains passing, cars driving, and timber logging activity.

To aid in studying correlations in the time domain we transform the ASDs of the ground motion into band-limited root mean square (BLRMS) segments. We compute the ASD over a segment of time sufficient to obtain the required frequency resolution and then in each frequency band compute the RMS of the velocity. This RMS becomes one data point in the BLRMS time series. We overlap the ASDs so that we get one BLRMS data point every minute. We use this same procedure to calculate BLRMS for the gravitational wave channel and auxiliary channels and can use combinations of BLRMS time series to look for correlations.

5.3 Daytime Noise

Figure 5.3 is a plot that illustrates the range variation that occurred on most days at LIGO Livingston during the first part of the third observing run (O3a). These range drops were most often noticed during daylight hours and correlated with increased anthropogenic ground motion. Thus, the noise became known as *daytime noise*.

The correlation with increased anthropogenic ground motion was easy to establish, but we were unable to narrow down the source to a particular section of the interferometer. All of the ground seismometers around the site saw increased anthropogenic ground motion as human activity increased during the daytime hours. Attempts to correlate the ground BLRMS with the DARM BLRMS proved unsuccessful.

With no clear correlation to a particular part of the interferometer, we began performing shaker injections in the $1-3\text{ Hz}$ and $3-10\text{ Hz}$ bands at various locations around the interferometer. Despite repeated attempts at several locations, we were never able to re-create the noise with shaker injections.

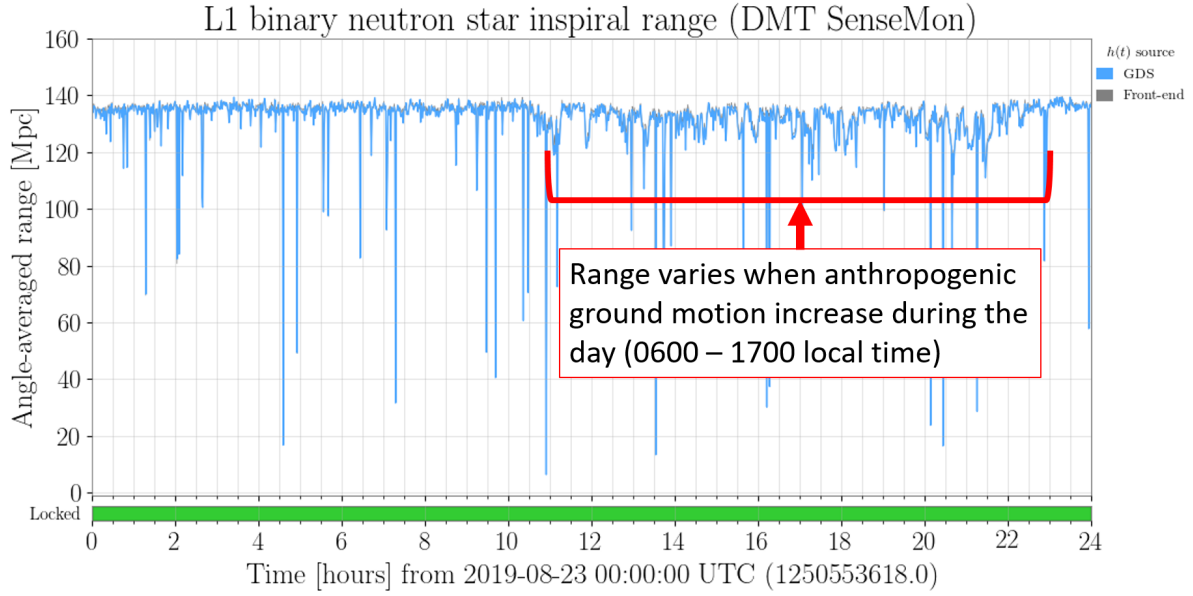


Figure 5.3. The binary neutron star inspiral range of LIGO Livingston over a 24 hour period. The highlighted region shows the dips in range associated with daytime noise.

The first clue as to the source of the noise came when Robert Schofield noticed that the range drops were correlated with noise seen in the photodiodes on the TMS at the X-end that monitor transmitted light [53]. Figure 5.4 is a spectrogram that shows the noise in both the gravitational wave channel (DARM) and the transmitted photodiode (TRX).

The daytime noise was not seismic upconversion of low-frequency ground motion but was instead linear coupling of higher frequency motion. We were seeing scattering shelves that were indicative of upconverted low-frequency motion, but these scattering shelves were not the primary driver of the range drops. This indicated that there were at least two different sources of scattered light noise. If we look at Figure 5.4 and compare the TRX spectrogram to the DARM spectrogram, we can see that there is excess noise in DARM that appears below 50 Hz (n.b. the large glitches such as the one at 2.5 minutes are not related to these investigations). This lower frequency noise in the DARM spectrogram was caused by seismic upconversion and will be discussed in subsequent sections.

Comparing the noise in TRX to the noise in DARM, we found that the signal to noise

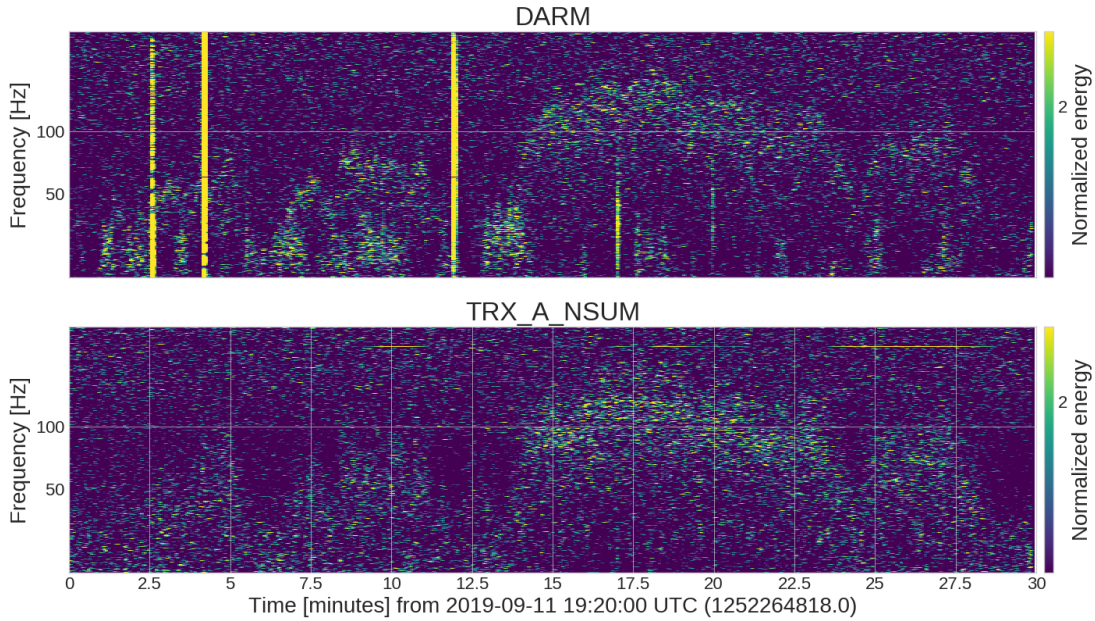


Figure 5.4. An example of daytime noise at LIGO Livingston. The noise could be seen in the gravitational wave channel (top) as well as in auxiliary sensors (bottom).

ratio (SNR) was higher in TRX than in DARM. This suggested that the noise source was on the transmitted side of the ETM and not in the arm cavity. We attempted to recreate the noise by using the OSEMS on the TMS structure to perform drive the motion of the structure but these efforts were unsuccessful.

To mitigate the noise, we designed a shroud to encapsulate the TMS structure and installed the shroud during the break from O3 in October 2019. Figure 5.5 shows the TMS structure before (left) and after (right) installing the shroud.

Following the installation of the TMS shroud, we no longer saw the daily range variations and we no longer saw the noise in spectrograms of either DARM or TRX. Figure 5.6 is a plot comparing the DARM, TRX, and ground BLRMS before and after the shroud installation. In this figure, we see that the daily increases in ground motion remained, but the daily noise in both DARM and TRX was no longer present after installing the TMS shroud. This is a clear indication that the daytime noise was successfully mitigated. We were never able to



Figure 5.5. The TMS structure before and after installing the stray light shroud.

identify the exact scattering mechanism and we do not see this noise in the other end station at LIGO Livingston nor in either of the end stations at LIGO Hanford.

5.4 Slow Scatter

When we examined the lower frequency noise in the DARM spectrograms that was mentioned in the previous section and that is visible in Figure 5.4, we found that there were actually two different kinds of noise. These noises became known as *slow scatter* and *fast scatter*. In this section, we discuss slow scatter and in the following section we discuss fast scatter.

Figure 5.7 is a spectrogram that shows the presence of slow scattering. In the spectrogram, we see the scattering arches that are indicative of upconverted low frequency motion. The spectrogram, when combined with Equation 3.21 gives us both the frequency and the amplitude of the displacement of the scattering surface responsible for the noise. The fringe frequency, f_{fringe} , can be read directly off of the spectrogram as the peak frequency achieved by the individual arches. With that information, we can determine the velocity of the scattering surface. As we saw in Figure 3.2 (which is an example of slow scatter), we can plot the right hand side of Equation 3.21 on top of the spectrogram and correctly predict the fringe

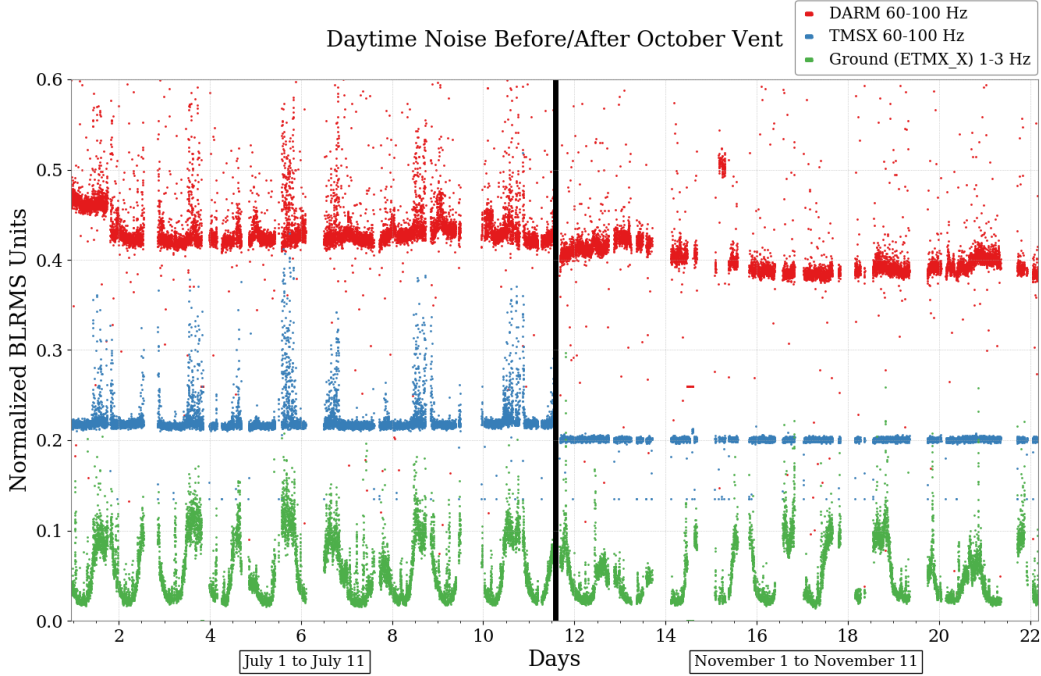


Figure 5.6. Ground motion in the 1-3 Hz frequency band (green) plotted alongside BLRMS of 60-100 Hz noise in DARM (red) and the transmon photodetector (blue). The spikes in DARM noise prior to installing baffles (on the left of the plot) correlated with the large range drops seen in Figure 5.3. Both the spikes in noise and the range drops went away after installing the baffles.

frequency. Since we are plotting the absolute value of the velocity, we can obtain the period, and thus the frequency, of the velocity by measuring the time between every other peak (e.g. the time between the first and third arch seen in Figure 5.7). The velocity is the derivative of the displacement, so the displacement has the same frequency as the velocity. We can then obtain the amplitude of the displacement by dividing the velocity by the angular frequency ($2\pi f$). Using these methods, we were able to determine that the slow scatter was a result of motion in the micro-seism band.

The source of the slow scatter was determined to be the gold traces on the reaction mass (RM) that make up the electro-static drive (ESD). Slow scatter often appeared as the fundamental along with one or more harmonics. As Equation 3.21 shows, these harmonics appear when the scattering path involves multiple reflections. The gold traces on the ESD are highly

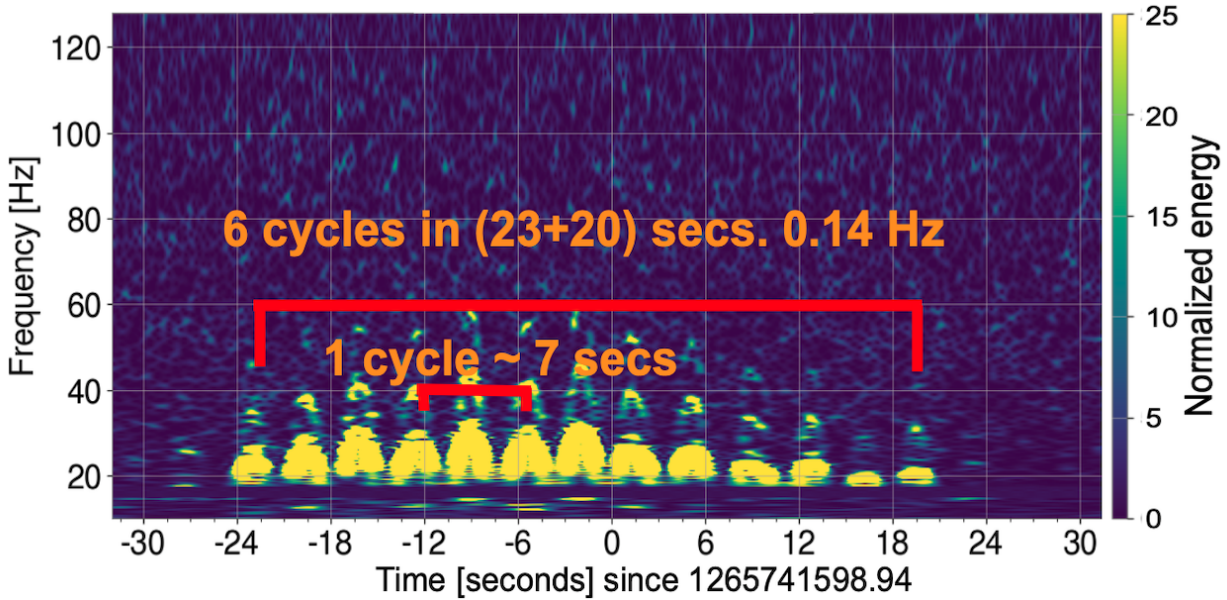


Figure 5.7. Spectrogram showing the presence of slow scattering in the gravitational wave channel at LIGO Livingston. The appearance of the arches coincided with increased ground motion at 0.14 Hz. Motion at this frequency is often attributed to ocean waves.

reflective, so multiple reflections between the ESD and the highly reflective (HR) coating on the test mass are not unexpected. We could also see that the OSEMs on the penultimate stage (PUM) of the reaction chain were seeing micron scale relative displacements between the test and reaction chains. Though this is not a direct measurement of the relative motion between the test and reaction masses, it serves as a close approximation below the pendulum resonance at around 0.45 Hz. Finally, we saw slow scatter in both LIGO Livingston and LIGO Hanford which indicated that it was not a localized problem such as the one that caused the daytime noise. Figure 5.8 is a schematic representation of the scattered light path [48].

The relative motion between the test and reaction chains is a result of the interferometer controls sending a drive signal to push the ETM so that it can maintain the resonance of the arm cavity. The interferometer controls are set up such that the ITMs and one of the ETMs are allowed to move with the motion of their respective ISIs. As we saw in Chapter 2, the ISI suppresses ground motion in the micro-seism band, but some residual motion is

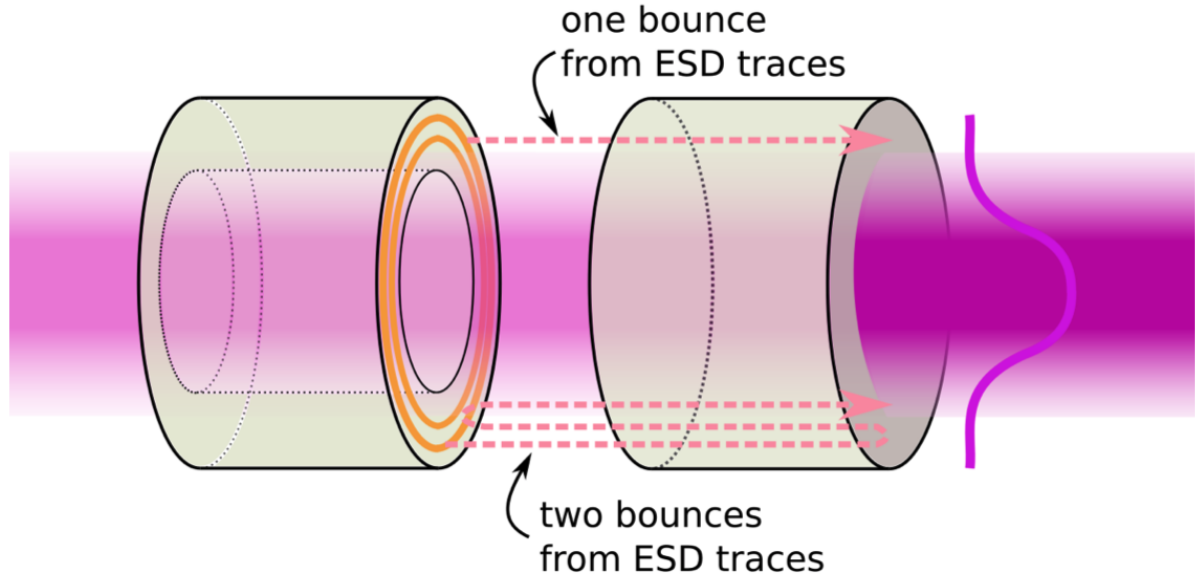


Figure 5.8. Schematic diagram showing the path traversed by the scattered light that caused slow scatter. A change to interferometer controls made the reaction chain follow the test mass chain and reduced the relative motion between the two chains.

still transmitted to the ISI optical table. Because the micro-seism frequencies lie below the resonant frequency of the suspension, this motion is then transmitted to the test mass. And because there is no phase correlation between the ground motion at the corner and end stations, it is necessary to apply a force to the remaining test mass so that it can follow the cavity and maintain resonance. The drive is applied to the ETM but not the RM, so during times of high micro-seismic ground motion the relative displacement between ETM and RM can reach tens of microns.

We can estimate the power in the scattered path by considering the power transmission of the ETM and the reflectivity of the RM. At LIGO Livingston, ETMX is the optic that is driven by interferometer controls and it has a measured HR transmission of 4.0 ppm [54]. Hiro Yamamoto estimated the power reflected from the RM in [55]. We now have all of the information required to estimate the noise using Equation 3.18. As mentioned in Chapter 3,

the amplitude transfer coefficient in this case is:

$$\begin{aligned}\frac{\delta I}{I} &= T_{\text{tm}} \cdot R_{\text{rm}} \cdot T_{\text{tm}} \\ &= T_{\text{tm}}^2 R_{\text{rm}},\end{aligned}\quad (5.1)$$

since we need to consider an ETM transmission, an RM reflection, and another ETM transmission. We adjusted the value of the R_{rm} term to achieve the best fit to the measured noise and arrived at a value of 2×10^{-4} which agrees reasonably well (within an order of magnitude) with Yamamoto's estimate [48]. The results of our noise projection agreed well with the measured noise and are plotted in Figure 3.3.

To mitigate the noise, we implemented a scheme that fed the signal from the PUM OSEM back to the top stage of the reaction chain (R0) so that the reaction chain (RC) would track the movements of the test mass chain [56]. Implementing the scheme successfully reduced the relative motion between the ETM and RM. Figure 5.9 compares spectrograms made during times of similar levels of micro-seismic ground motion before (left) and after (right) implementing RC tracking. The arches that remain in the after image are the result of relative motion between the ETM and the TMS.

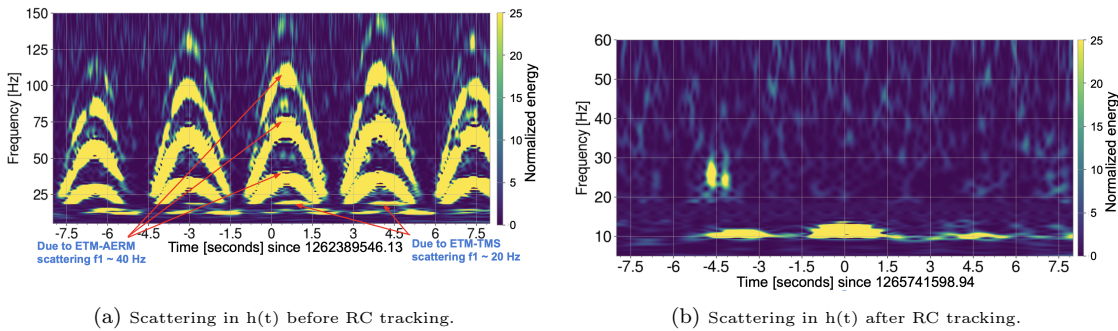


Figure 5.9. Comparison of scattering arches in DARM before and after implementing RC tracking. With similar levels of ground motion, we no longer see the scattering shelves due to the relative motion of the ETM and the RM. The shelves that remain in the image on the right are from relative motion of the ETM and the TMS. This ETM-TMS noise is also visible in the image on the left at the bottom of the ETM-RM arches [48].

We also used a tool called *GravitySpy* to evaluate the improvements made by RC tracking.

GravitySpy uses machine learning for image recognition to classify different glitch types that appear in the gravitational wave channel. GravitySpy is a citizen science project where volunteers generate training sets for the machine learning algorithm by classifying images of glitches [57]. One of the glitch classes is scattering glitches, so we can compare the rate of scattering glitches identified by GravitySpy before and after RC tracking to quantify the improvements. RC tracking was implemented at both LIGO sites and Figure 5.10 compares the rate of glitches before and after RC tracking at both sites. At LIGO Livingston (LLO) we see that the glitch rate is decreased considerably as the ground motion begins to exceed $1\mu\text{m}/\text{s}$ and at LIGO Hanford (LHO) we see a decreased glitch rate at all levels of micro-seismic ground motion.

5.5 Fast Scatter

The *fast scatter* mentioned in the previous section was first identified by Joshua Smith and Andrew Lundgren in April 2019 just as the third observing run was beginning [58]. Figure 5.11 is a spectrogram that shows fast scatter in the gravitational wave channel (DARM). The fast scatter was well correlated with increased anthropogenic band ground motion and specifically with trains passing by on the nearby tracks. The train tracks are approximately 6.03 km from the closest part of the interferometer, which is the Y-End station. When a train passes, the 1-3 Hz BLRMS can exceed $1\mu\text{m}/\text{s}$. For comparison, the normal daytime level is below $0.5\mu\text{m}/\text{s}$ and at night it can fall to $0.1\mu\text{m}/\text{s}$ or less.

The fast scatter noise is so named because the spacing of subsequent arches in the time domain is approximately 0.25 seconds or we can say that they occur with a frequency of 4 Hz (compare to slow scatter where the arches are approximately 3.5 seconds apart or 0.28 Hz). In the case of slow scatter, we obtained the period of the scattering surface motion by counting the time between alternating arches. In the case of fast scatter, the situation was different and the scattering surface was moving with a period that corresponded with the spacing between adjacent arches. The reason for this is that the noise was actually the result

of the combination of motion in the micro-seism and anthropogenic bands. We can see in Figure 5.11 that the groups of fast scattering arches are spaced at time intervals that are consistent with micro-seismic ground motion (in this case, alternate peaks are approximately 5 seconds apart corresponding to 0.2 Hz scattering surface motion). Figure 5.12 compares a zoomed in portion of the DARM spectrogram to a spectrogram made using a simple model that combined a 0.2 Hz sine wave with a 4.4 Hz sine wave. Both the spacing between subsequent fast scattering arches and the spacing between groups of arches in the model agree with the spacing seen in DARM.

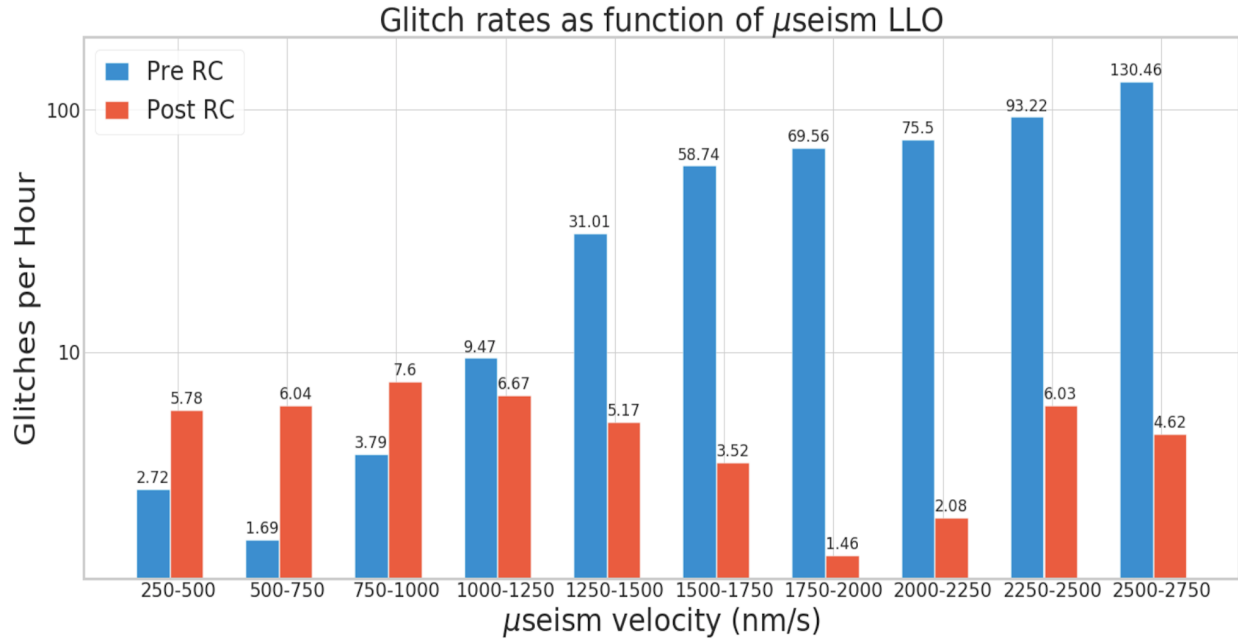
To understand why we measure between alternate peaks for slow scatter and between adjacent peaks for fast scatter in order to determine the frequency of the scattering surface motion, we consider the displacement. The velocity of the scattering surface is the angular frequency, $\omega = 2\pi f$, of the scattering surface multiplied by the displacement, x_{scat} : $v = 2\pi f x_{scat}$. For a scattering surface moving with a velocity of $1\mu m/s$ at 0.2 Hz, the displacement is $0.79\mu m$. Likewise, a 4.4 Hz motion at $1\mu m/s$ corresponds to a displacement of $0.036\mu m$. If we were to sum two sine waves with these parameters, we would find a large amplitude 0.2 Hz wave with a smaller 4.4 Hz superimposed on top of it. If we then took the derivative of this summed sine wave, we would have the velocity. It is the magnitude of the velocity that determines the fringe frequency, so we plot the magnitude of this summed sine wave in Figure 5.13. We can see that as the 0.2 Hz motion passes through its maximum velocity, the 4.4 Hz motion goes through several cycles. At times, the velocities are in the same direction and the two velocities sum. At other times, the opposite is true and the magnitude of the total velocity is less than either of the component velocities. We have plotted one period of the 0.2 Hz velocity and we see two "arches." The time between subsequent 0.2 Hz peaks represents half of the total period and we measure between alternate peaks to obtain the full period. For the summed sine wave, subsequent peaks represent the full period, so we measure between subsequent peaks to obtain the full period.

We reviewed the design documents for several interferometer components and found that

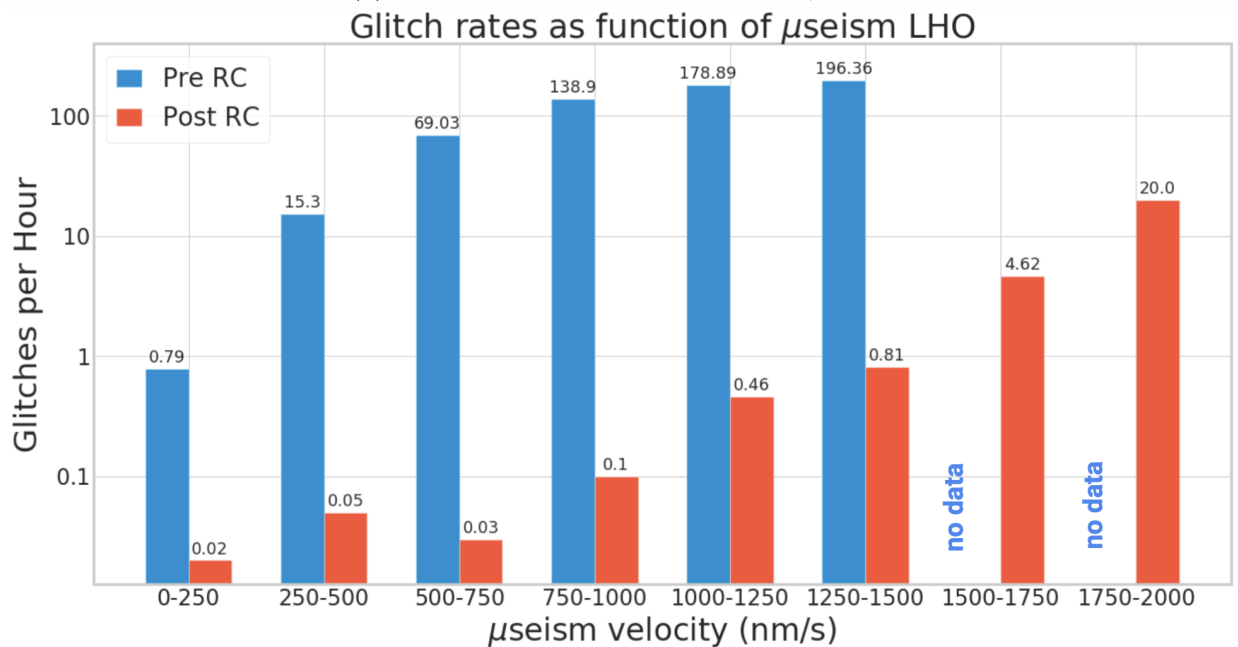
the cryo baffle had a resonance in the vicinity of 4 Hz. The resonance had been recorded as being 3.8 Hz, so we performed shaker injections near the end station cryo baffles at that frequency. At the X-End, we saw no interferometer response, but at the Y-End the 3.8 Hz injection produced noise with the same characteristics as fast scatter. The Q-transform of the DARM response to this injection is shown in Figure 5.14.

To zero in on the exact resonant frequency, we performed a series of sweep injections with the low-frequency shaker [56]. Figure 5.15 shows the accelerometer (top) and DARM (bottom) response to a sweep injection that went from 3.3-3.9 Hz. The resonance appears at 3.49 Hz. A 4-5 Hz sweep injection showed an additional resonance at 4.62 Hz as shown in Figure 5.16.

Efforts are currently underway to damp the mechanical resonances of the cryo baffle. When the damping work is completed, the shaker injections will be repeated to determine if the fast scatter noise has been mitigated.



(a) LLO glitch rate as a function of μ seism.



(b) LHO glitch rate as a function of μ seism.

Figure 5.10. Glitch rates from GravitySpy before and after reaction chain (RC) tracking was implemented at both sites. The data is binned by ranges of ground motion [48].

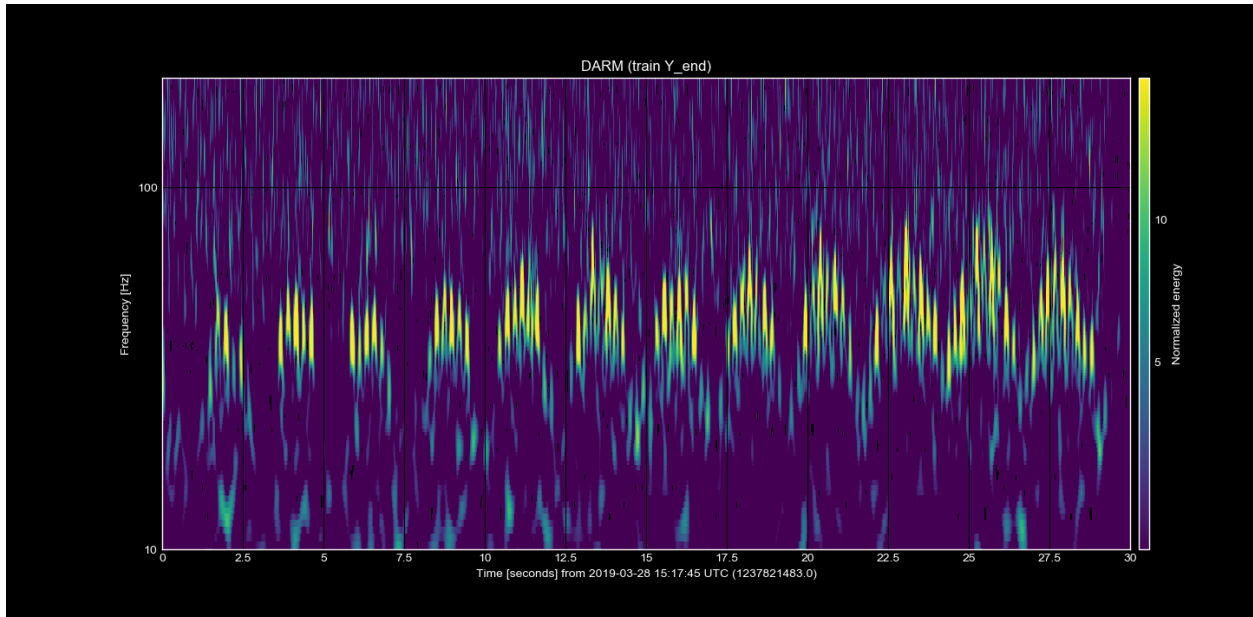


Figure 5.11. DARM spectrogram showing the presence of fast scattering. This spectrogram was made using data from a time when a train was passing by the site. Trains increase the ground motion in the anthropogenic band.

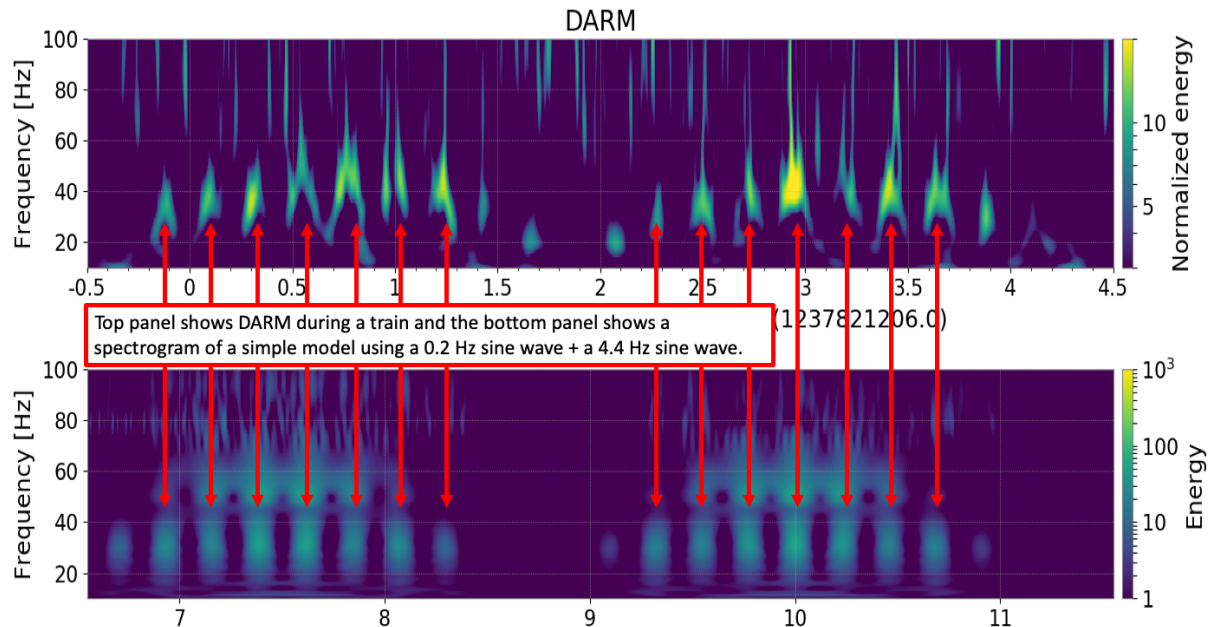


Figure 5.12. The top panel is a zoom in of the noise seen in Figure 5.11 and the bottom panel is a spectrogram of a simple model that combines 0.2 Hz motion with 4.4 Hz motion to obtain a similar shape to the noise seen in DARM.

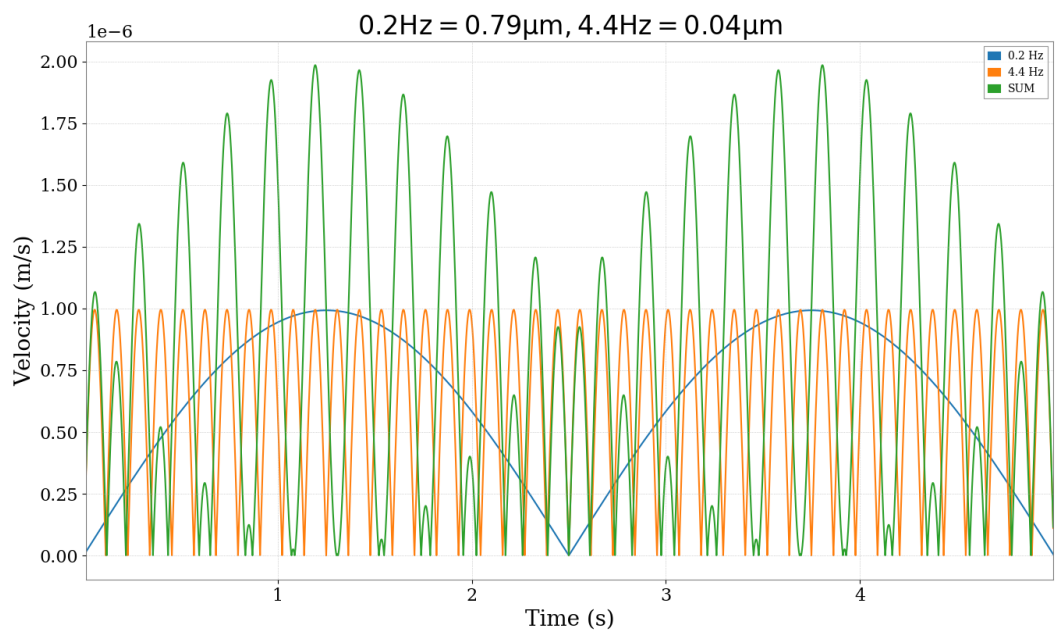


Figure 5.13. A simple plot illustrating the summing of 0.2 Hz and 4.4 Hz velocities. As the 0.2 Hz motion passes through its maximum velocity, the 4.4 Hz motion goes through several cycles. At times, the two velocities are in the same direction and thus sum, but at others the 4.4 Hz motion is opposite the 0.2 Hz motion, so the overall velocity is less than the 0.2 Hz would be on its own.

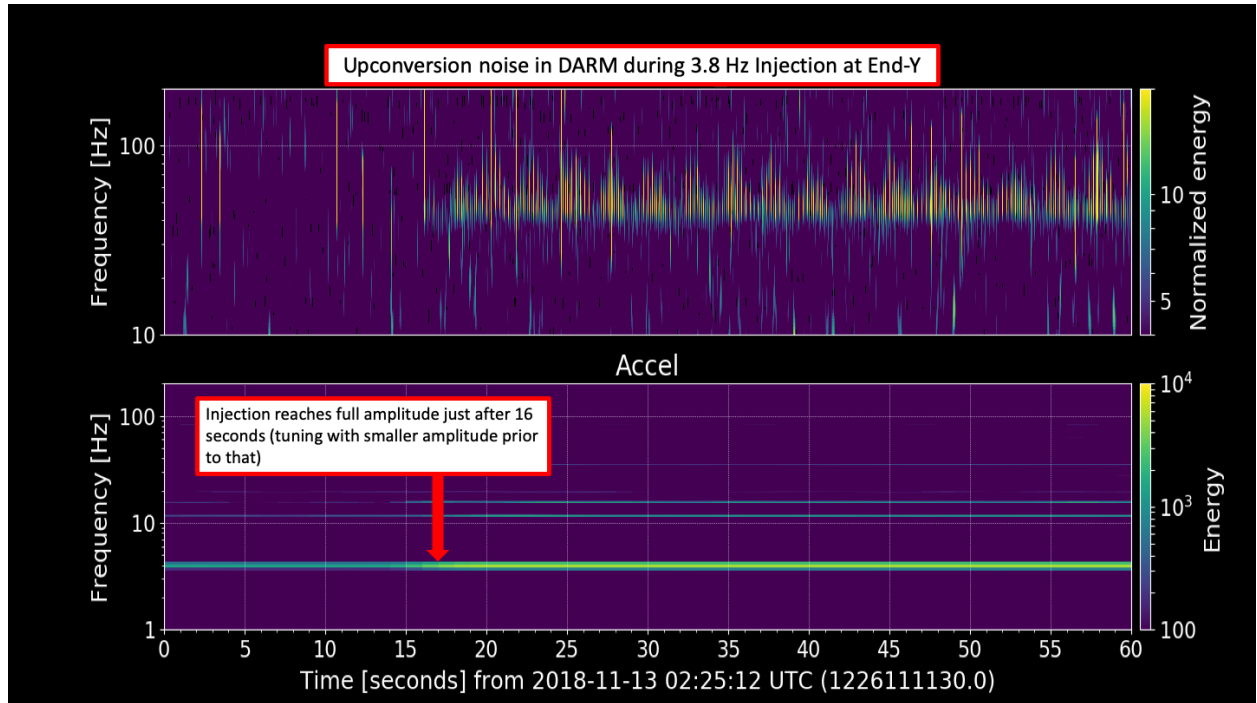


Figure 5.14. Spectrogram showing the DARM (top) and accelerometer (bottom) response to a 3.8 Hz injection performed at the manifold between the BSC that houses ETMY and the cryo pump. As the injection reaches full amplitude, fast scatter noise appears in the DARM spectrogram.

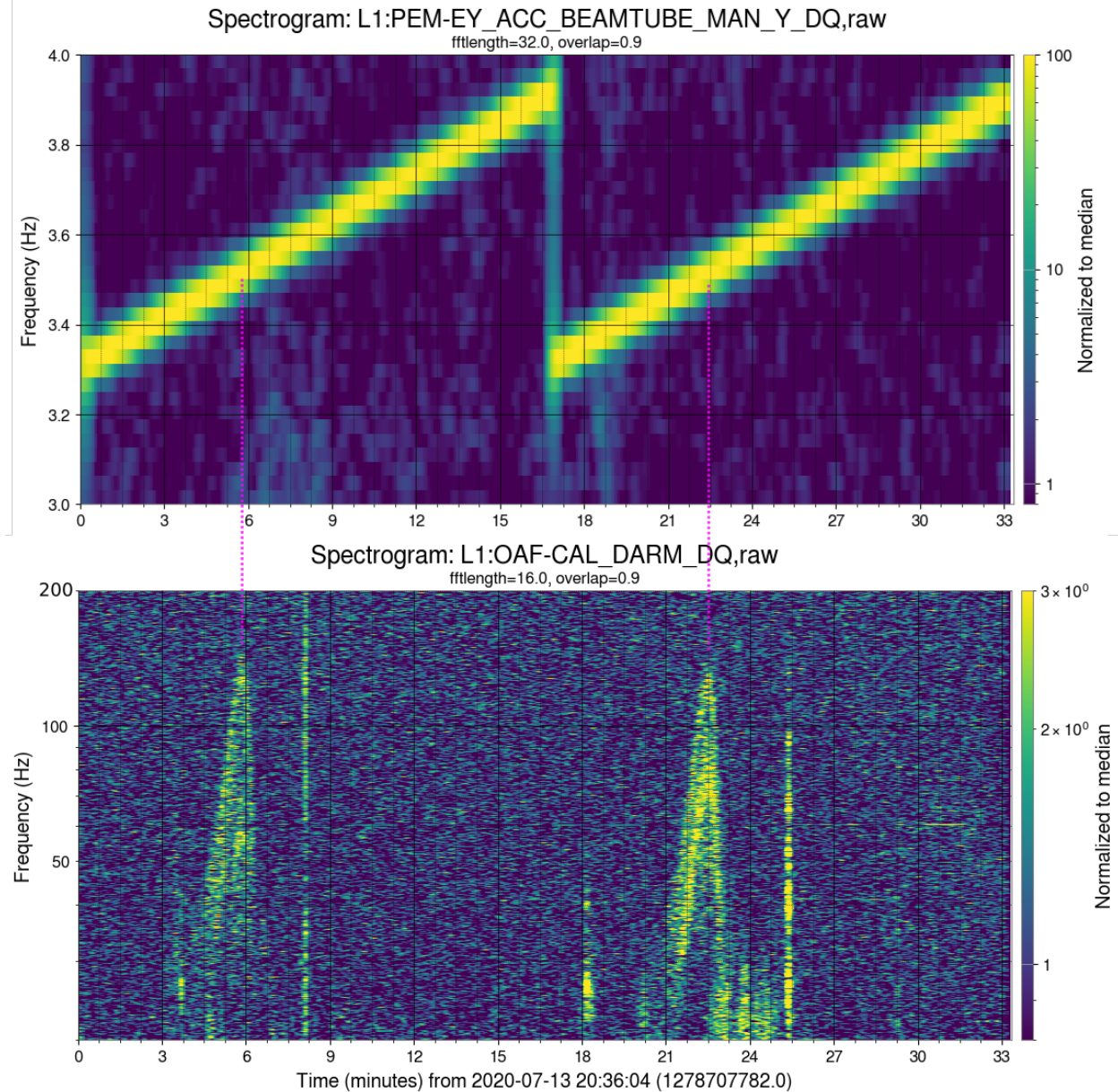


Figure 5.15. Accelerometer (top) and DARM (bottom) response to a sweep injection that ran from 3.3 Hz to 3.9 Hz. As the sweep passes through 3.5 Hz (as seen by the accelerometer) we see upconverted noise in DARM.

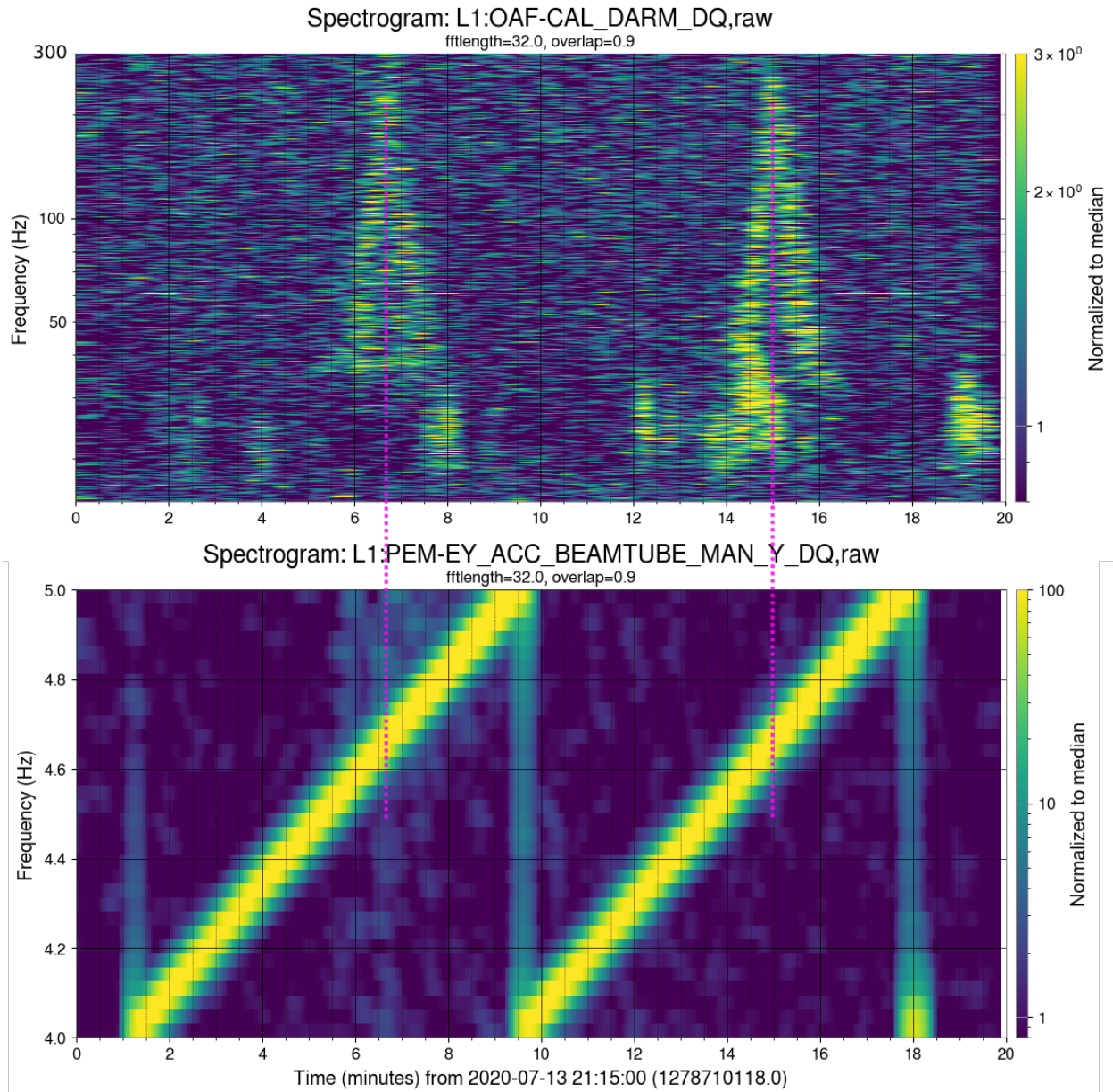


Figure 5.16. DARM (top) and accelerometer (bottom) response to a sweep injection that ran from 4 Hz to 5 Hz. As the sweep passes through 4.6 Hz (as seen by the accelerometer) we see upconverted noise in DARM.

CHAPTER 6. BACKSCATTERED LIGHT IN THE LIGO BEAMTUBES

Light that scatters from one test mass then bounces one or more times off of the beamtube and then recombines with the main beam at the opposite test mass is called *forward scattering* and was considered by Thorne in [45]. This analysis showed that the forward scattering in the beamtube would be a potential limiting noise source for LIGO, so baffles were installed inside the beamtube during its construction to mitigate this forward scattering. The baffles limited the amount of light that would forward scatter, but some amount of light can *back scatter* from the baffles and recombine with the main beam at the same mirror from which it originated. This light picks up phase noise from the acoustic motion of the beamtube and creates amplitude noise when it interferes with the main beam circulating in the arms. Noise associated with back scattered light from the beamtube baffles was first considered by Flanagan and Thorne in [45]. More recently, Martynov [59] and Bai [60] have studied the implications of this noise on future detectors. Both Martynov and Bai added to the original analysis by including the effects of radiation pressure and Bai also included seismic upconversion of the beamtube motion. We here also use updated calculations of the *bidiirectional reflectivity distribution function* (BRDF) which tells us how light scatters from the test masses. In this chapter, we review the calculations as well as a series of measurements made at LIGO Livingston that allowed us to set upper limits on the noise.

6.1 Noise from Backscattered Light

In Chapter 3 we wrote down the following equation for the equivalent strain noise due to scattered light:

$$\tilde{h}(f) = A \left[\frac{h_{\text{eff}}}{\Phi} \right] \tilde{S}(f) + A \left[\frac{h_{\text{eff}}}{RIN} \right] \tilde{C}(f). \quad (6.1)$$

where the amplitude transfer coefficient, A , is defined as the ratio of the scattered field and the measurement field. For convenience, we wrote down the following definition in terms of

the ratio of powers:

$$A^2 \equiv \frac{\delta I}{I} \quad (6.2)$$

In the case of backscattered light in the beamtube, we have three scattering events that must take place for the light to cause noise in the gravitational wave channel: the light scatters from the test mass, the light backscatters from surfaces inside the beamtube, and the light re-combines with the main beam. The ratio of powers is then:

$$\begin{aligned} \frac{\delta I}{I} &= \beta_{\text{mir}} \cdot \beta_{\text{baf}} \cdot \beta_{\text{mir}} \cdot \frac{d\Omega}{r^2} \\ &= \beta_{\text{mir}}^2 \beta_{\text{scat}} \frac{d\Omega}{r^2}, \end{aligned} \quad (6.3)$$

where β_{mir} and β_{baf} are the BRDF of the test mass and beamtube baffles respectively, $d\Omega = 2\pi \sin \theta d\theta$ is the solid angle over the backscattering surfaces, $r = R/\sin \theta$ is the distance to the backscattering surface, R is the beamtube radius, and θ is the angle between the main beam and the scattered light.

6.1.1 BRDF of Test Masses

Given a spectrum of mirror surface roughness (i.e. its phase map), we can simulate the scattered light distribution assuming a Gaussian beam incident on the mirror. In addition, due to the large number of point defects on the surface, we find that there is a larger contribution to the scattered light at large angles than would be estimated from the mirrors' surface PSD alone.

Figure 6.1 is a plot showing the BRDF of the LIGO test masses. This plot combines the BRDF from surface roughness with the BRDF from point defects. In the following sections, we detail how we obtained these curves.

Surface Roughness

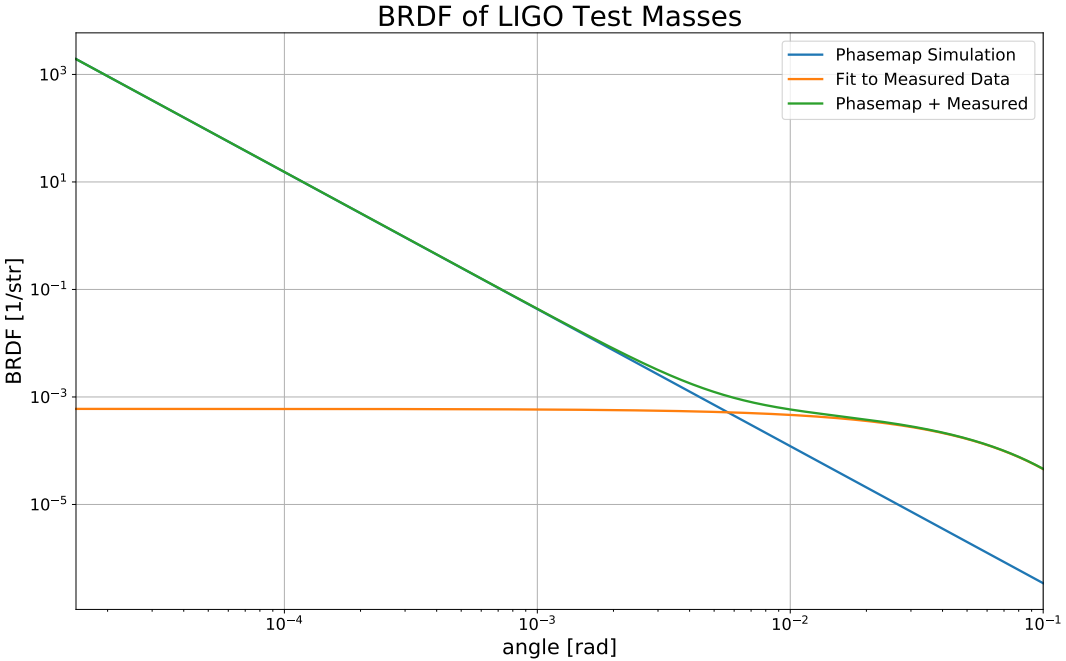


Figure 6.1. BRDF of LIGO test masses created using the sum of phasemap simulations and a fit to measurements made of wide-angle scatter due to point defects.

Light scatters due to surface roughness with spatial frequency ξ at an angle $\theta \sim \lambda\xi$. The rate at which light scatters is proportional to the amplitude of the surface roughness. In order to calculate the BRDF from the phasemap of a mirror, we use the Stationary Interferometer Simulator (SIS) software developed by Hiro Yamamoto and others [61]. The simulation calculates the interaction of the fields with the test mass in the spatial domain and the field is propagated along the arm using the paraxial approximation to Maxwell's equation for a plane wave. We sample the field amplitude at the radius of the beamtube along the distance of the beamtube to obtain the scattered light distribution. We then apply a fit of the following form to obtain an expression for the BRDF due to surface roughness:

$$\beta_{\text{mir,rough}} = \frac{Z}{\theta^n} \quad (6.4)$$

Using the phasemaps of the ETMs at LIGO Livingston, the result of fitting gives the following values for the fitting parameters Z and n :

$$Z = 9.66 \times 10^{-10} \quad n = 2.55 \quad (6.5)$$

We then substitute Eq. 6.4 into Eq. 6.3 and integrate over the length of the beamtube to get the following:

$$A_{\text{rough,ITM}}^2 = 2.37 \times 10^{-15}, \quad (6.6)$$

$$A_{\text{rough,ETM}}^2 = 2.38 \times 10^{-15}. \quad (6.7)$$

The differences arise from the fact that the ITMs are 30 m from the start of the beamtube and the ETMs are 10 m away. This gives the following for the limits of integration:

$$0.00015 < \theta_{ITM} < 0.02, \quad (6.8)$$

and

$$0.00015 < \theta_{ETM} < 0.06, \quad (6.9)$$

We then sum the contribution from all four test masses as incoherent sources to obtain:

$$A_{\text{rough,ave}}^2 = \sqrt{2(A_{\text{rough,ITM}}^2)^2 + 2(A_{\text{rough,ETM}}^2)^2} \quad (6.10)$$

Point Defects

The phasemap calculation underestimates the amount of light scattered at large angles due to point defects on the surface of the mirror. To account for this, we made measurements of the power scattered into viewports in the interferometer while operating the interferometer

[62]. We then applied a fit to this measured data to obtain the following:

$$\beta_{\text{mir,point}} = 6 \times 10^{-4} e^{-25.78\theta}. \quad (6.11)$$

We can substitute Eq. 6.11 into Eq. 6.3 and integrate along the beamtube (using the same limits of integration as above) to obtain:

$$A_{\text{point,ITM}}^2 = 1.12 \times 10^{-15}, \quad (6.12)$$

and

$$A_{\text{point,ETM}}^2 = 1.99 \times 10^{-14}. \quad (6.13)$$

Again, we sum the contribution from the four test masses in quadrature to obtain:

$$A_{\text{point,ave}}^2 = \sqrt{2(A_{\text{point,ITM}}^2)^2 + 2(A_{\text{point,ETM}}^2)^2} \quad (6.14)$$

Finally, to obtain A from Equation 6.1, we add $A_{\text{rough,ave}}^2$ and $A_{\text{point,ave}}^2$ in quadrature:

$$A^2 = \sqrt{(A_{\text{rough,ave}}^2)^2 + (A_{\text{point,ave}}^2)^2}. \quad (6.15)$$

6.1.2 Coherence Length of Beamtube Vibrations

The question of whether backscattered light from different baffles is coherent or incoherent determines if we should sum the amplitude or the power, respectively, to determine the full contribution of noise to the gravitational wave channel. In [45], Flanagan and Thorne worked under the assumption that the noise would be incoherent. In [60], Bai provides the following justification for that assumption.

We begin by writing the backscattered field as follows:

$$\psi = \sum_{a=1}^N \psi_a, \quad (6.16)$$

where ψ_a is the field backscattered from baffle a and ψ is the sum over all N baffles. Rewriting the field from individual baffles in terms of amplitude and phase gives $\psi_a = |\psi_a| e^{i\phi_a}$. This allows us to write the total backscattered power as follows:

$$|\psi|^2 = \sum_{a,b=1}^N |\psi_a| |\psi_b| e^{i\phi_a} e^{-i\phi_b}. \quad (6.17)$$

The phase shift from individual baffles, ϕ_a is proportional to kz_a where z_a is the distance to the baffle from the test mass. We saw previously that phase wrapping occurs with displacements on the order of $\lambda/2$. Since the location of the baffles is not precise on the order of one micron and $\lambda = 1.064$ microns, it is reasonable to assume that the phase of the light coming from subsequent baffles would not be coherent and we sum the contribution from individual baffles as incoherent sources:

$$\langle |\psi|^2 \rangle = \sum_{a=1}^N |\psi_a|^2. \quad (6.18)$$

6.2 Driven Measurements of Acoustic Coupling

The goal of this work was to measure the coupling of acoustic motion of the beamtube to the gravitational wave channel. To measure the motion of the beamtube, we installed accelerometers along both arms of the interferometer as shown in Figure 6.2. Figure 6.2 is representative of the Y-arm of the interferometer, but we installed equivalent sensors along the X-arm. The accelerometers are noise limited at lower frequencies, so we used previously installed ground seismometers to provide the low frequency portion of the motion spectrum necessary for taking into account fringe wrapping. Between 5-10 Hz, both types of sensors

provide useful data, so we high passed the accelerometer data and low passed the seismometer data with a crossover frequency of 8 Hz. We then combined the two filtered spectra to obtain a complete spectra for the motion of the beamtube. The ground seismometers are not located on the beamtube, so we had to work under the assumption that the beamtube follows the ground at low frequencies.

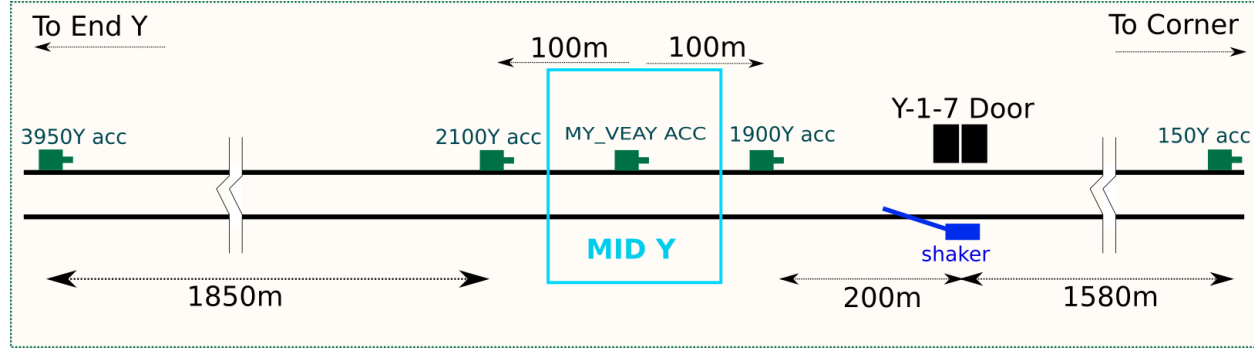


Figure 6.2. Schematic layout of equipment for driven measurements of beamtube backscatter. The accelerometers were permanently installed along the beamtube and the shaker was moved around to different locations.)

6.2.1 Ambient Vibration Levels

We first wanted to look at the noise from backscattered light in the beamtube during normal operation of the interferometer. We collected data from the ITM on the X-arm of the interferometer and data from accelerometers installed along the X-arm of the interferometer during the month of September 2019. We averaged the data from the 5 beamtube accelerometers and combined the data with the seismometer data to obtain a complete motion spectrum as described in the previous section. We used this data in Eq. 6.1 along with the values for $A_{rough,ave}$ and $A_{point,ave}$ from Eqs. 6.10 and 6.14 to make noise projections due to surface roughness and point defects respectively. We also added the two together in quadrature to obtain a total noise estimate. The results of these ambient noise projections are shown in Figure 6.3 (the total noise projection is not shown as it lies nearly on top of the curve for noise from point defects). We find that the total ambient noise level is more than

two orders of magnitude below the noise floor of the interferometer. The noise from point defects dominates the total noise from backscattered light as it is an order of magnitude larger than that from surface roughness.

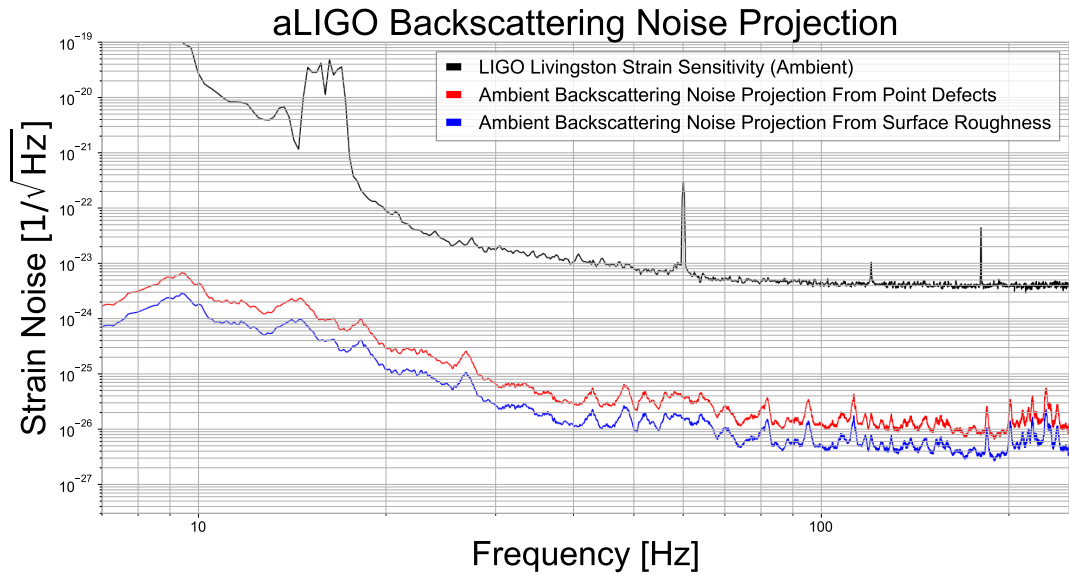


Figure 6.3. Ambient backscattering noise projections due to surface roughness and point defects on the surfaces of the test masses.

6.2.2 Driven Measurements

With the ambient noise levels lying so far below the noise floor of the interferometer, we decided to perform a series of driven measurements to verify our model. The idea behind the driven measurement is that we attach a mechanical shaker to the beamtube to increase the motion of the beamtube. For these tests, we used the low-frequency shaker that was described in Chapter 4. Figure 6.4 is a photograph showing the low-frequency shaker attached to the beamtube. We measure the increased motion with the accelerometers and use the driven motion spectra as an input to our model. We then compare the results of our model with driven motion to the interferometer response.

We began by making broadband injections in two different bands: from 10-30 Hz and



Figure 6.4. APS 113 Electro-Seis shaker with carbon fiber connecting tube used to perform driven measurements of the beamtube.

from 30-100 Hz. We also performed a slow sweep injection that started at 10 Hz and continued up to 100 Hz. We next tried lower frequency injections including a line at 1.55 Hz and a sweep from 1-5 Hz. These low frequency injections were visible in temporary accelerometers placed at the injection location, but these injections did not propagate to the permanent accelerometers installed along the beamtube. None of these injections showed up in the output of the interferometer, but we did notice a few mechanical resonances of the beamtube showing up in our accelerometers.

Equation 6.1 assumes a mostly uniform motion of both arms of the beamtube. With only one shaker, we could only excite one arm of the beamtube, and even with the maximum

output of the shaker, we could only excite one full arm by exploiting the mechanical resonances mentioned above. A 14.1 Hz resonance propagated along one half of the arm where the excitation was applied, but failed to propagate past the gate-valve at the mid-station. A 56.4 Hz resonance was the only injection propagated the full length of one arm, so we used that injection to make noise projections. We again took the average of the beamtube accelerometers along the arm where the injection was made and combined that average with data from the ground seismometer to obtain a complete motion spectra. We then added a factor of 1/2 to Equation 6.1 to account for the fact that we were only exciting one arm.

By using the shaker, we increased the average motion of the beamtube at the 56.4 Hz resonance by a factor of 230. Despite this, we did not see any response in the output of the detector. Figure 6.5 plots the projection of the injection along with the output of the interferometer during the injection. The peak amplitude of the upconverted projection lies a factor of 4.7 below the noise floor of the interferometer. This allows us to set an upper limit on the noise from backscattered light in the beamtube. We show the upper limit of the ambient noise as a dashed line in Figure 6.5. This upper limit for ambient noise is a factor of 10 or more below the current sensitivity of the instrument.

6.3 Implications for Future Detectors

The next generation of ground-based gravitational wave detectors will likely utilize longer arms along with other technological improvements to achieve higher sensitivity than is possible with current generation detectors like LIGO. A look back at Equation 2.22 demonstrates why this increase in arm length will increase sensitivity:

$$h(t) = \frac{\Delta L}{L}. \quad (6.19)$$

The strain sensitivity is the change in distance measured divided by the distance over which the change is measured, so an increase in arm length equates to improved sensitivity.

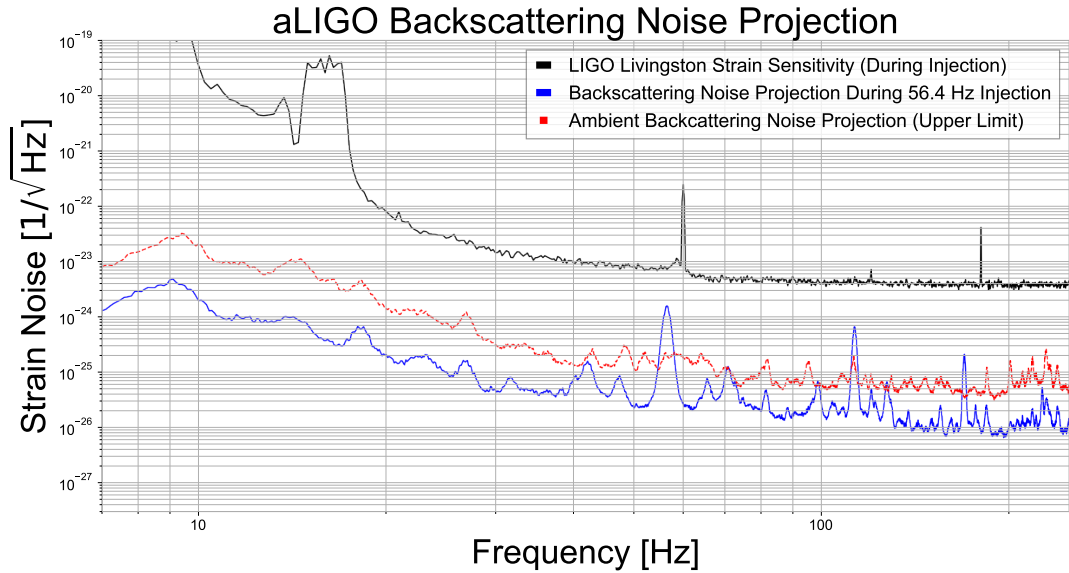


Figure 6.5. Backscattering noise projection made using data from driven measurements. The blue curve is the projection made using the data from driven measurements and the red curve is an upper limit applied to the ambient noise spectra.

Cosmic Explorer is a proposed next generation gravitational wave detector with 40 km long arms with a design that is otherwise very similar to that of LIGO with the A+ upgrades installed. The fabrication and vacuum pumping of the 40 km long beamtubes that will make up the arms of Cosmic Explorer will make up a significant portion of both the monetary and time budgets of the project. Therefore, it is necessary to consider the problem of noise from backscattered light in the beamtubes. The reports by Martynov [59] and Bai [60] were written to specifically address the issue of noise from backscattered light in the beamtubes, but we apply the methods of this paper to the problem in the following paragraphs.

We begin by substituting $L = 40$ km into Equations 3.13 and 3.17. We then update the limits of integration listed in Equations 6.8 and 6.9 with the following:

$$0.000015 < \theta_{ITM,CE} < 0.02, \quad (6.20)$$

and

$$0.000015 < \theta_{ETM,CE} < 0.06, \quad (6.21)$$

With these parameters updated, we are able to make noise projections for Cosmic Explorer. Figure 6.6 compares the noise projection and the upper limits for the noise to the design sensitivity of Cosmic Explorer. Near the beamtube resonance at 14.1 Hz, the noise projection

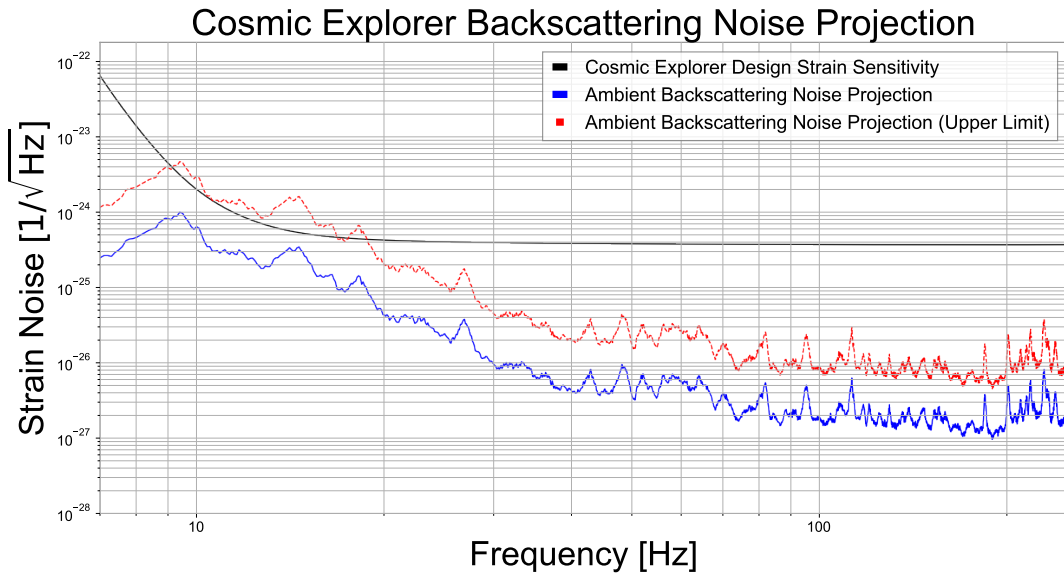


Figure 6.6. Backscattering noise projection and upper limits for Cosmic Explorer. Ambient noise projects below the Cosmic Explorer design curve, but the upper limits extend above the design sensitivity from 9-19 Hz.

is within a factor of 2 of the design sensitivity. The upper limit calculation projects above the noise floor of Cosmic Explorer from 9-19 Hz.

These projections do not take into account any possible improvements to the design of Cosmic Explorer that could reduce the noise. These improvements include better coatings on the test masses with less surface roughness and fewer point defects which would reduce the BRDF and altered geometry of the beamtube, including larger radius, that would decrease the backscatter at small angles which becomes dominant with 40 km arms.

6.4 Summary

We have established reliable estimates for the backscatter noise contribution to the LIGO sensitivity. We also performed a series of driven measurements in an attempt to measure the noise contribution. Though our driven measurements failed to show a response in the interferometer, the measurements allowed us to establish upper limits on the noise contribution from backscattered light. These upper limits lie far enough below the current sensitivity of the instrument to allow us to state that noise due to backscattered light in the beamtube will not be a limiting noise source for LIGO.

We also applied our calculations to a next generation gravitational wave detector, Cosmic Explorer. The proximity of the noise projections to the design sensitivity of Cosmic Explorer suggest that further study is needed to ensure that noise due to backscattered light in the beamtube will not be a limiting noise source for Cosmic Explorer.

CHAPTER 7. CONCLUSION

In this document we have described the mechanisms by which scattered light can cause noise in the gravitational wave channel.

We reviewed the SLiC project and the baffles that were installed as part of the project. Coatings for the baffles were chosen based on their optical properties, cost, handling, and manufacturing constraints. SolidWorks and Zemax were used to determine the location of the baffle apertures and to ensure that ghost beams were properly dumped. Installation of the baffles was followed by a series of shaker injections that were used to measure the effectiveness of the baffles. At the end of the project, coupling to the gravitational wave channel in the output arm and at one of the end stations had been reduced.

We studied the investigations of scattered light noise due to increased ground motion. The shroud installed on the TMS structure at the X-end eliminated the daytime noise. RC tracking implemented at both LIGO sites greatly reduced the relative motion between the test and reaction masses. As a result of this work, the peak frequency and thus the impact on overall sensitivity of the slow scattering shelves has been reduced. Fast scattering has been fully characterized, the likely source has been identified, and a mitigation strategy is currently being implemented.

Finally, we presented the results of measurements made to determine the noise due to beamtube backscatter. We established upper limits for the noise and determined that this noise will not be a limiting source for LIGO. We made noise projections for the next generation Cosmic Explorer project and found that the upper limit projections lie near or slightly above the design sensitivity of Cosmic Explorer.

The astrophysical impacts of this work are difficult to quantify, but we can consider a couple of examples to understand the effects.

During O3, LIGO Livingston had greater sensitivity than LIGO Hanford in the 20-100 Hz frequency range most affected by scattered light as shown in Fig. 7.1. While the differences between the two detectors are not necessarily due to scattered light, the comparison helps to

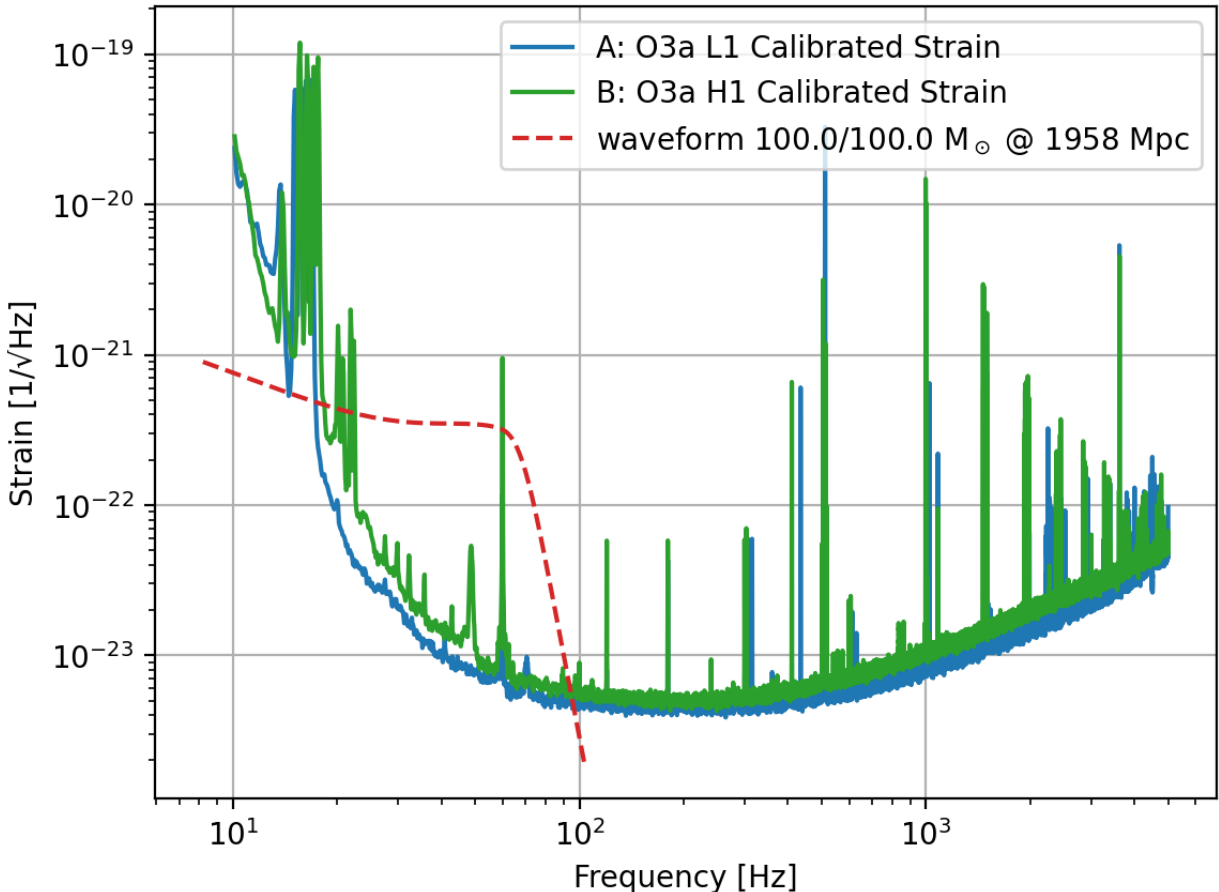


Figure 7.1. Strain sensitivities of LIGO Livingston (blue) and LIGO Hanford (green) during O3a.

understand how improving detector sensitivity in this frequency range impacts astrophysical searches. If we consider a pair of $100M_{\odot}$ black holes, the detection range for LIGO Livingston is 1958 Mpc. For LIGO Hanford, that range is reduced to 1557 Mpc [63].

A metric, VT , that is often used to evaluate potential interferometer upgrades is the product of the volume of spacetime observed and the time spent observing. We can look back at Figure 1.1 and see that the rate of detections has increased over time as the sensitivity of the gravitational wave detector network has increased. Taking the time to make detector improvements has resulted in more detections than would have been made without the improvements even when the time spent not observing is considered. While this work did

not significantly increase the maximum range (and thus the volume observed), it did reduce, and in some cases eliminate, the range drops associated with increased ground motion. The detectors are then able to spend more time observing at their maximum sensitivity thus increasing the VT of the detectors.

We can also look at one of the more significant observations made to date by the LIGO-VIRGO network to understand the impact of this work. GW190521 was the largest system observed by LIGO to date and represented the first observation of an IMBH. The signal from this event swept up in frequency from 30-80 Hz and the SNR of the signal at LIGO Livingston was 11.5. Compare this to fast and slow scattering, and we see that both affect the same 30-80 Hz frequency band. Slow scattering occurred with a median SNR of 37.6 and the median SNR for fast scattering is 11.0. Slow and fast scattering had median durations of 3.2 and 1.3 seconds respectively [48]. The signal from GW190521 had a duration of 0.1 seconds [43]. Had fast or slow scatter been present in the interferometer output at the time the signal from GW190521 passed through the LIGO detector, we likely would not have seen it.

Scattered light remains one of the more difficult noise sources to measure and mitigate in gravitational wave detectors. The methods described here provide a framework for identifying sources of scattered light. Spectra and spectrograms provide information about the velocity and displacement of the scattering surface. Data from seismometers, accelerometers, and OSEMs are systematically searched to identify correlations. Ray tracing and SolidWorks models are used to identify potential scattering paths. Once a source is identified, a mitigation strategy can be employed. Baffles can be used to reduce the amount of power in the scattering path and to direct the scattered light away from the main beam. Changing interferometer controls can be used to reduce the relative motion between optics and scattering surfaces. As further improvements to detector sensitivity are made with future upgrades, such as frequency-dependent squeezing, new sources of scattered light noise will be revealed. Managing scattered light noise will be critical in order to see continued improvements to

detector sensitivity. We have presented here a set of tools that will greatly aid in reducing scattered light noise for years to come.

WORKS CITED

- [1] LIGO. *LIGO suspends third observing run.* URL <https://www.ligo.caltech.edu/news/ligo20200326>. Accessed 11 Sep 2020.
- [2] A. Buikema, C. Cahillane, G. L. Mansell, C. Blair, et al. Sensitivity and performance of the advanced ligo detectors in the third observing run. *Phys. Rev. D*, 102:062003, Sep 2020. doi: 10.1103/PhysRevD.102.062003.
- [3] Hsin-Yu Chen, Daniel E. Holz, John Miller, Matthew Evans, Salvatore Vitale, and Jolien Creighton. Distance measures in gravitational-wave astrophysics and cosmology, 2020.
- [4] D. V. Martynov and E. D. Hall. Sensitivity of the advanced ligo detectors at the beginning of gravitational wave astronomy. *Phys. Rev. D*, 93:112004, Jun 2016. doi: 10.1103/PhysRevD.93.112004. URL <https://link.aps.org/doi/10.1103/PhysRevD.93.112004>.
- [5] Albert Einstein. *The Berlin Years: Correspondence, 1914–1918 (English Translation Supplement, Translated by Ann Hentschel)*. 2016. URL <http://einsteinpapers.press.princeton.edu/VOL8-trans/224>.
- [6] Jorge Cervantes-Cota, Salvador Galindo-Uribarri, and George Smoot. A brief history of gravitational waves. *Universe*, 2(3):22, Sep 2016. ISSN 2218-1997. doi: 10.3390/universe2030022. URL <http://dx.doi.org/10.3390/universe2030022>.
- [7] J. M. Weisberg, J. H. Taylor, and L. A. Fowler. Gravitational waves from an orbiting pulsar. *Scientific American*, 245:74–82, October 1981. doi: 10.1038/scientificamerican1081-74.
- [8] Robert L. Forward. Wideband laser-interferometer gravitational-radiation experiment. *Phys. Rev. D*, 17:379–390, Jan 1978. doi: 10.1103/PhysRevD.17.379. URL <https://link.aps.org/doi/10.1103/PhysRevD.17.379>.
- [9] P. Lindsay, P. Saulson, and R. Weiss. *A Study of a Long Baseline Gravitational Wave Antenna System*. URL https://dcc.ligo.org/public/0028/T830001/000/NSF_bluebook_1983Accessed22Sep2020.
- [10] Peter Saulson. *Fundamentals of Interferometric Gravitational Wave Detectors*. World Scientific Publishing Co., 1994.
- [11] Charles Misner, Kip Thorne, and John Wheeler. *Gravitation*. W. H. Freeman and Company, 1973.
- [12] Abbott et al. Observation of gravitational waves from a binary black hole merger. *Phys. Rev. Lett.*, 116:061102, Feb 2016. doi: 10.1103/PhysRevLett.116.061102.
- [13] Chris L. Fryer and Kimberly C. B. New. Gravitational waves from gravitational collapse. *Living Reviews in Relativity*, 14, Jan 2011.

- [14] B. P. Abbott and others. First targeted search for gravitational-wave bursts from core-collapse supernovae in data of first-generation laser interferometer detectors. *Phys. Rev. D*, 94:102001, Nov 2016. doi: 10.1103/PhysRevD.94.102001. URL <https://link.aps.org/doi/10.1103/PhysRevD.94.102001>.
- [15] B. P. Abbott et al. First search for gravitational waves from known pulsars with advanced LIGO. *The Astrophysical Journal*, 839(1):12, apr 2017. doi: 10.3847/1538-4357/aa677f. URL <https://doi.org/10.3847%2F1538-4357%2Faa677f>.
- [16] Benjamin P. Abbott et al. Upper limits on the stochastic gravitational-wave background from advanced ligo's first observing run. *Phys. Rev. Lett.*, 118(12):121101, 2017. doi: 10.1103/PhysRevLett.118.121101, 10.1103/PhysRevLett.119.029901.
- [17] *Basic michelson labeled*. www.ligo.caltech.edu. Accessed 9 Oct 2018.
- [18] J. Giaime. Studies of laser interferometer design and avibration isolation system for interferometricgravitational wave detectors. PhD Thesis, Massachusetts Institute of Technology, 1995.
- [19] R. Weiss. Quarterly Progress Report No. 105. Technical Report LIGO-P720002, 2010. URL <https://dcc.ligo.org/LIGO-P720002>.
- [20] R.W.P. Drever, J.L. Hall, F.V. Kowalski, et al. Laser phase and frequency stabilization using an optical resonator. *Appl. Phys. B*, 31:97–105, 1983. URL <https://doi.org/10.1007/BF00702605>.
- [21] Denis Martynov. Lock acquisition and sensitivity analysis of advanced ligo interferometers. PhD Thesis, California Institute of Technology, 2015.
- [22] Carlton M. Caves. Quantum-mechanical radiation-pressure fluctuations in an interferometer. *Phys. Rev. Lett.*, 45:75–79, Jul 1980. doi: 10.1103/PhysRevLett.45.75. URL <https://link.aps.org/doi/10.1103/PhysRevLett.45.75>.
- [23] Carlton M. Caves. Quantum-mechanical noise in an interferometer. *Phys. Rev. D*, 23: 1693–1708, Apr 1981. doi: 10.1103/PhysRevD.23.1693. URL <https://link.aps.org/doi/10.1103/PhysRevD.23.1693>.
- [24] M. Tse, Haocun Yu, N. Kijbunchoo, A. Fernandez-Galiana, P. Dupej, L. Barsotti, et al. Quantum-enhanced advanced ligo detectors in the era of gravitational-wave astronomy. *Phys. Rev. Lett.*, 123:231107, Dec 2019. doi: 10.1103/PhysRevLett.123.231107. URL <https://link.aps.org/doi/10.1103/PhysRevLett.123.231107>.
- [25] Gabriela I. González and Peter R. Saulson. Brownian motion of a mass suspended by an anelastic wire. *The Journal of the Acoustical Society of America*, 96(1):207–212, 1994. doi: 10.1121/1.410467. URL <https://doi.org/10.1121/1.410467>.
- [26] Yu. Levin. Internal thermal noise in the ligo test masses: A direct approach. *Phys. Rev. D*, 57:659–663, Jan 1998. doi: 10.1103/PhysRevD.57.659. URL <https://link.aps.org/doi/10.1103/PhysRevD.57.659>.

- [27] J Aasi et al. Advanced ligo. *Classical and Quantum Gravity*, 32(7):074001, 2015.
- [28] S M Aston et al. Update on quadruple suspension design for advanced LIGO. *Classical and Quantum Gravity*, 29(23):235004, oct 2012. doi: 10.1088/0264-9381/29/23/235004. URL <https://doi.org/10.1088%2F0264-9381%2F29%2F23%2F235004>.
- [29] F Maticichard, B Lantz, R Mittelman, K Mason, J Kissel, B Abbott, S Biscans, J McIver, R Abbott, S Abbott, E Allwine, S Barnum, J Birch, C Celerier, D Clark, D Coyne, D DeBra, R DeRosa, M Evans, S Foley, P Fritschel, J A Giaime, C Gray, G Grabeel, J Hanson, C Hardham, M Hillard, W Hua, C Kucharczyk, M Landry, A Le Roux, V Lhuillier, D Macleod, M Macinnis, R Mitchell, B O'Reilly, D Ottaway, H Paris, A Pele, M Puma, H Radkins, C Ramet, M Robinson, L Ruet, P Sarin, D Shoemaker, A Stein, J Thomas, M Vargas, K Venkateswara, J Warner, and S Wen. Seismic isolation of advanced LIGO: Review of strategy, instrumentation and performance. *Classical and Quantum Gravity*, 32(18):185003, aug 2015. doi: 10.1088/0264-9381/32/18/185003. URL <https://doi.org/10.1088%2F0264-9381%2F32%2F18%2F185003>.
- [30] M.E. Zucker and S.E. Whitcomb. Measurement of optical path fluctuations due to residual gas in the ligo 40 meter interferometer. In *Proceedings of the Seventh Marcel Grossman Meeting on Recent Developments in Theoretical and Experimental General Relativity, Gravitation, and Relativistic Field Theories*, pages 1434–1436, 1996. URL <https://dcc-llo.ligo.org/public/0073/P940008/000/P940008-00.pdf>.
- [31] R. Dolesi, M. Hueller, D. Nicolodi, D. Tombolato, S. Vitale, P. J. Wass, W. J. Weber, M. Evans, P. Fritschel, R. Weiss, J. H. Gundlach, C. A. Hagedorn, S. Schlamminger, G. Ciani, and A. Cavalleri. Brownian force noise from molecular collisions and the sensitivity of advanced gravitational wave observatories. *Phys. Rev. D*, 84:063007, Sep 2011. doi: 10.1103/PhysRevD.84.063007. URL <https://link.aps.org/doi/10.1103/PhysRevD.84.063007>.
- [32] M. Smith. Scattered Light Control in Advanced LIGO. Technical Report LIGO-P1000002, 2010. URL <https://dcc.ligo.org/LIGO-P1000002>.
- [33] B. P. Abbott et al. Binary Black Hole Mergers in the first Advanced LIGO Observing Run. *Phys. Rev.*, X6(4):041015, 2016. doi: 10.1103/PhysRevX.6.041015,10.1103/PhysRevX.8.039903. [Erratum: Phys. Rev.X8,no.3,039903(2018)].
- [34] B. P. Abbott et al. Properties of the binary black hole merger gw150914. *Phys. Rev. Lett.*, 116:241102, Jun 2016. doi: 10.1103/PhysRevLett.116.241102. URL <https://link.aps.org/doi/10.1103/PhysRevLett.116.241102>.
- [35] Benjamin P. Abbott et al. GW170104: Observation of a 50-Solar-Mass Binary Black Hole Coalescence at Redshift 0.2. *Phys. Rev. Lett.*, 118(22):221101, 2017. doi: 10.1103/PhysRevLett.118.221101,10.1103/PhysRevLett.121.129901. [Erratum: Phys. Rev. Lett.121,no.12,129901(2018)].
- [36] B.. P.. Abbott et al. GW170608: Observation of a 19-solar-mass Binary Black Hole Coalescence. *Astrophys. J.*, 851(2):L35, 2017. doi: 10.3847/2041-8213/aa9f0c.

- [37] B. P. Abbott et al. GW170814: A Three-Detector Observation of Gravitational Waves from a Binary Black Hole Coalescence. *Phys. Rev. Lett.*, 119(14):141101, 2017. doi: 10.1103/PhysRevLett.119.141101.
- [38] B. P. Abbott et al. Gw170817: Observation of gravitational waves from a binary neutron star inspiral. *Phys. Rev. Lett.*, 119:161101, Oct 2017.
- [39] B. P. Abbott et al. Multi-messenger Observations of a Binary Neutron Star Merger. *Astrophys. J.*, 848(2):L12, 2017. doi: 10.3847/2041-8213/aa91c9.
- [40] B. P. Abbott et al. GW190425: Observation of a compact binary coalescence with total mass $\sim 3.4 M_{\odot}$. *The Astrophysical Journal*, 892(1):L3, mar 2020. doi: 10.3847/2041-8213/ab75f5. URL <https://doi.org/10.3847%2F2041-8213%2Fab75f5>.
- [41] R. Abbott et al. Gw190412: Observation of a binary-black-hole coalescence with asymmetric masses. *Phys. Rev. D*, 102:043015, Aug 2020. doi: 10.1103/PhysRevD.102.043015. URL <https://link.aps.org/doi/10.1103/PhysRevD.102.043015>.
- [42] R. Abbott et al. GW190814: Gravitational waves from the coalescence of a 23 solar mass black hole with a 2.6 solar mass compact object. *The Astrophysical Journal*, 896(2):L44, jun 2020. doi: 10.3847/2041-8213/ab960f. URL <https://doi.org/10.3847%2F2041-8213%2Fab960f>.
- [43] R. Abbott et al. Gw190521: A binary black hole merger with a total mass of $150 M_{\odot}$. *Phys. Rev. Lett.*, 125:101102, Sep 2020. doi: 10.1103/PhysRevLett.125.101102. URL <https://link.aps.org/doi/10.1103/PhysRevLett.125.101102>.
- [44] David Ottaway, Peter Fritschel, and Samuel Waldman. Impact of upconverted scattered light on advanced interferometric gravitational wave detectors. *Optics Express*, 2012.
- [45] Eanna Flanagan and Kip Thorne. Noise due to backscatter off baffles, the nearby wall, and objects at the far end of the beam tube. T940063.
- [46] P. Fritschel and M. Zucker. Wide-angle scatter from ligo arm cavities. T070089.
- [47] P. Fritschel and Yamamoto H. Scattered Light Noise Due to the ETM Coating Ripple. Technical Report LIGO-T1300354-v3, 2013. URL <https://dcc.ligo.org/LIGO-T1300354/public>.
- [48] S Soni, C Austin, A Effler, G González, R Schofield, A Urban, and G Valdes. Reducing scattered light in ligo's third observing run. *Classical and quantum gravity*, jan 2020.
- [49] A. Effler and V. Frolov. LLO aLOG: <https://alog.ligo-la.caltech.edu/aLOG/index.php?callRep=34687>.
- [50] S. Aston. LLO aLOG: <https://alog.ligo-la.caltech.edu/aLOG/index.php?callRep=19047>.
- [51] D. Martynov and N. Mukund. LLO aLOG: <https://alog.ligo-la.caltech.edu/aLOG/index.php?callRep=28541>.

- [52] J. Chavez. aLIGO Systems Layout LLO X-End Station. Technical Report LIGO-D0901465-v6, 2011. URL <https://dcc.ligo.org/LIGO-D0901465>.
- [53] R. Schofield, A. Effler, and C. Austin. LLO aLOG: <https://alog.ligo-la.caltech.edu/aLOG/index.php?callRep=46147>.
- [54] *LIGO Optics*. <https://galaxy.ligo.caltech.edu/optics/>.
- [55] Hiro Yamamoto. Effects of scattered light by AERM. **DCC document T1500455-v2**, 2015.
- [56] Anamaria Effler et al. Reaction chain now tracks main chain for both ETMs. [alog 50851](#), 2019.
- [57] M Zevin, S Coughlin, S Bahaadini, E Besler, N Rohani, S Allen, M Cabero, K Crowston, A K Katsaggelos, S L Larson, and et al. Gravity spy: Integrating Advanced LIGO detector characterization, machine learning, and citizen science. *Classical and Quantum Gravity*, 34(6):064003, Feb 2017. ISSN 1361-6382. doi: 10.1088/1361-6382/aa5cea. URL <http://dx.doi.org/10.1088/1361-6382/aa5cea>.
- [58] J. Smith and A. Lundgren. LLO aLOG: <https://alog.ligo-la.caltech.edu/aLOG/index.php?callRep=44803>.
- [59] Denis Martynov. Analysis of scattering in lungo arm cavities. LIGO Technical Document: T1500590, 2016.
- [60] Yuntao Bai. Cosmic Explorer: Back-Scattering Noise and Design Recommendations. Technical Report LIGO-T1900854, 2019.
- [61] Hiroaki Yamamoto. SIS (Stationary Interferometer Simulation) manual. Technical Report LIGO-T070039-v8, 2013.
- [62] A. Effler and C. Blair. LLO aLOG: <https://alog.ligo-la.caltech.edu/aLOG/index.php?callRep=35580>.
- [63] *Gravitational wave detector inspiral range calculator*. URL: <https://range.ligo.org/>.

VITA

Corey Austin grew up in Mangham, Louisiana and graduated from Mangham High School. He went on to Louisiana State University where he received a B.S. in General Studies in 2005. Following graduation, Corey worked in the oil and gas industry for 7 years before leaving to pursue a graduate degree in physics. In 2015, Corey earned a M.S. in Applied Physics from Louisiana Tech University. He then moved back to Baton Rouge, LA to and worked at the LIGO Livingston observatory in pursuit of a Ph.D. in Physics.